

AD-A040 027

BDM CORP ALBUQUERQUE N MEX  
GENERAL ELECTROMAGNETIC MODEL FOR THE ANALYSIS OF COMPLEX SYSTEMS--ETC(U)  
APR 77 R J BALESTRI, T R FERGUSON

F/G 20/3

F30602-74-C-0182

RADC-TR-77-137-VOL-2

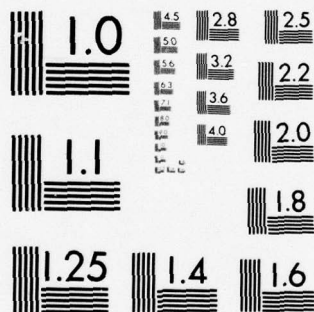
NL

UNCLASSIFIED

1 OF 2

AD  
A040027





MICROCOPY RESOLUTION TEST CHART  
NATIONAL BUREAU OF STANDARDS-1963-A



GENERAL ELECTROMAGNETIC MODEL FOR THE ANALYSIS OF COMPLEX SYSTEMS, VOL II

AD A 040027

AD No.

DDC FILE COPY

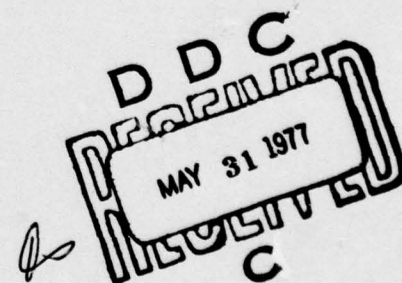
RADC-TR-77-137, Volume II (of two)  
Final Technical Report  
April 1977

GENERAL ELECTROMAGNETIC MODEL FOR THE ANALYSIS OF COMPLEX SYSTEMS  
Engineering Manual

The BDM Corporation



Approved for public release; distribution unlimited.



ROME AIR DEVELOPMENT CENTER  
AIR FORCE SYSTEMS COMMAND  
GRIFFISS AIR FORCE BASE, NEW YORK 13441

This report contains a large percentage of machine-produced copy which is not of the highest printing quality but because of economical consideration, it was determined in the best interest of the government that they be used in this publication.

This report has been reviewed by the RADC Information Office (OI) and is releasable to the National Technical Information Service (NTIS). At NTIS it will be releasable to the general public, including foreign nations.

This report has been reviewed and approved for publication.

APPROVED:

*Kenneth R. Siarkiewicz*  
KENNETH R. SIARKIEWICZ  
Project Engineer

APPROVED:

*Joseph J. Naresky*  
JOSEPH J. NARESKY  
Chief, Reliability & Compatibility Division

FOR THE COMMANDER:

*John P. Huss*  
JOHN P. HUSS  
Acting Chief, Plans Office

Do not return this copy. Retain or destroy.

UNCLASSIFIED

SECURITY CLASSIFICATION OF THIS PAGE (When Data Entered)

REPORT DOCUMENTATION PAGE		READ INSTRUCTIONS BEFORE COMPLETING FORM
1. REPORT NUMBER RADC-TR-77-137, Vol II (of two) ✓	2. GOVT ACCESSION NO. (9)	3. RECIPIENT'S CATALOG NUMBER
4. TITLE (and Subtitle) GENERAL ELECTROMAGNETIC MODEL FOR THE ANALYSIS OF COMPLEX SYSTEMS, Engineering Manual. Volume II.	5. TYPE OF REPORT & PERIOD COVERED Final Technical Report, 2 Apr 74 - 30 Sep 76	6. PERFORMING ORG. REPORT NUMBER N/A
7. AUTHOR(s) R. J. Balestri, T. R. Ferguson E. R. Anderson	8. CONTRACT OR GRANT NUMBER(s) F30602-74-C-0182	9. PERFORMING ORGANIZATION NAME AND ADDRESS The BDM Corporation 2600 Yale Blvd, S.E. Albuquerque NM 87106
10. CONTROLLING OFFICE NAME AND ADDRESS Rome Air Development Center (RBCT) Griffiss AFB NY 13441	11. REPORT DATE April 1977	12. NUMBER OF PAGES 113
13. MONITORING AGENCY NAME & ADDRESS (if different from Controlling Office) Same (12) 23p.	14. SECURITY CLASS. (of this report) UNCLASSIFIED	15a. DECLASSIFICATION/DOWNGRADING SCHEDULE N/A
16. DISTRIBUTION STATEMENT (of this Report) Approved for public release; distribution unlimited. (16) 4540 (17) 41 (18) RADC		
17. DISTRIBUTION STATEMENT (of the abstract entered in Block 20, if different from Report) Same (19) TR-77-137-Vol-2		
18. SUPPLEMENTARY NOTES RADC Project Engineer: Kenneth R. Siarkiewicz (RBCT)		
19. KEY WORDS (Continue on reverse side if necessary and identify by block number) Electromagnetic Compatibility Method of Moments Antenna Analysis Matrix Equation Solution		
20. ABSTRACT (Continue on reverse side if necessary and identify by block number) Volume I of this report is the user's manual for the GEMACS code developed under this contract. GEMACS utilizes a MOM (Method of Moments) formalism with the EFIE (Electric Field Integral Equation) for the solution of electromagnetic radiation and scattering problems. The code employs both full matrix decomposition and Banded Matrix Iteration solution techniques and is expressly designed for large problems. → next page (Continued)		

DD FORM 1 JAN 73 1473

EDITION OF 1 NOV 65 IS OBSOLETE

UNCLASSIFIED

SECURITY CLASSIFICATION OF THIS PAGE (When Data Entered)

391884

y/b



UNCLASSIFIED

SECURITY CLASSIFICATION OF THIS PAGE(When Data Entered)

COM → Volume II of this report describes the engineering approximations, the theory and implementation of the Banded Matrix Iteration scheme, and the results of a wire grid modeling study that established consistent wire grid modeling requirements for large structures. ↑

Accession for	
NTIS	White Section <input checked="" type="checkbox"/>
DDC	Detl Section <input type="checkbox"/>
UNANNOUNCED	<input type="checkbox"/>
JUSTIFICATION	
DISTRIBUTION/AVAILABILITY CODES	
ORG.	AVAIL. ORG./OF SPECIAL
M	

UNCLASSIFIED

SECURITY CLASSIFICATION OF THIS PAGE(When Data Entered)

## TABLE OF CONTENTS

	<u>Page</u>
A. INTRODUCTION	1
B. GEMACS FUNCTIONS	1
1. Geometric Modeling	2
2. Structure Excitation	5
3. Interaction Computation	9
4. Solution Process Implementation	23
5. Observables Computation	29
C. BANDED MATRIX ITERATION THEORY AND DEVELOPMENT SUMMARY	36
1. Introduction	36
2. Theory	37
3. Convergence Measures	40
4. Stability	42
5. Segment Numbering	45
6. Choice of Bandwidth	52
7. Computer Timing Requirements	59
D. SUMMARY OF RESULTS	63
1. Single Straight Wires	63
2. Multiple Straight Wires	66
3. Modified AMP	69
E. RECOMMENDATIONS FOR FUTURE EFFORTS	82
REFERENCES	84
APPENDIX	
A. ANTENNA SYSTEM EFFECTIVENESS AS AFFECTED BY ENVIRONMENT	A-1

## LIST OF ILLUSTRATIONS

<u>Figure</u>		<u>Page</u>
1	Geometry of Current Filament	20
2	Illustration of Matrix Reduction During Decomposition	25
3	Parallel Strips Superimposed on a Wire Loop	46
4	A Set of Parallel Strips Normal to a Direction Vector $d$	48
5	An Object of Irregular Shape with Various Possible Direction Vectors	49
6	Part of the Segment Numbering Obtained with the Principal Axis Slicing System for a Rectangular Parallelepiped	51
7	The Curve of $g_{LIM}$ Versus $f$ and a Fictitious Example of Actual Efficiencies	53
8	Efficiency Versus $f$ for an Example Problem. Curve Labels are the Convergence Criteria on the Relative Error	55
9	The Linear Trend Between the Bandwidth Estimate and the Object Length $L$ ( $R_M$ = Distance Corresponding to Bandwidth)	58
10	Equation Solution Time Versus Number of Complex Multiplicative Operations	61
11	Matrix Fill Time Versus Number of Unknowns ( $\odot$ , Grid Problems; $\square$ , No Multiple Junctions)	62
12	Relative Error Versus Number of Iterations, Example 4 of Reference 1	64
13	Relative Error (Percent) Versus Matrix Bandwidth for First Iteration, Example 4 of Reference 1	65

# LIST OF ILLUSTRATIONS (Concluded)

<u>Figure</u>		<u>Page</u>
14	Amplitude of Current on a Sphere for Plane Wave Scattering, $ka = 4.7$ , Example 13 of Reference 5 (Surface Currents $K$ from Reference 14; Solid Line for E-Plane, Dashed for H-Plane. Wire Grid Currents $I$ ; $\odot$ for E-Plane, $\otimes$ for Near H-Plane)	73
15	Normalized E-Plane Bistatic Cross Section for a Wire Gridded Plate, Example 6A	77
16	Normalized H-Plane Bistatic Cross Section for a Wire Gridded Plate, Example 6A	77
17	Sample Wire Grid Currents for Example 6A or 6B	78
18	Wire Currents Along Edge Normal to the E-Field, Example 6	80
19	Far Field for Plane Wave Scattering from a Strip, H-Polarization, Reference 15	81
20	Far Field for Plane Wave Scattering from a Strip, E-Polarization (Line from Reference 15, Points from Wire Grid)	81



# LIST OF TABLES

<u>Table</u>		<u>Page</u>
1	RELATIVE ERROR (%) FOR EXAMPLE 9, REFERENCE 2 (VERTICAL HALF-RHOMBIC ANTENNA, N=80)	56
2	DESCRIPTION OF EXAMPLE 12 FROM REFERENCE 2	68
3	RELATIVE ERROR (PERCENT) AND CP TIME (SECONDS) FOR EXAMPLE 12 FROM REFERENCE 2	70
4	DESCRIPTION OF EXAMPLE 6 FROM REFERENCE 5	75
5	CONVERGENCE DATA FOR EXAMPLE 6A (N = 544, M = 132)	76
6	CONVERGENCE DATA FOR EXAMPLE 6B (N = 544, M = 132)	76
7	CONVERGENCE DATA FOR EXAMPLE 6C (N = 544, M = 132)	76



### SYMBOLS AND ABBREVIATIONS

A	Impedance matrix
a	Radius of a sphere, cylinder, disk, etc.
B	Banded matrix composed of the principal diagonal of A, M adjacent upper minor diagonals, and M adjacent lower minor diagonals
b	Excitation column vector
$B^{-1}$	The inverse of the matrix B
BMI	Banded matrix iteration
$B_L$	The lower triangular banded matrix obtained by decomposing B
$B_U$	The upper triangular banded matrix obtained by decomposing B
$BCRE_j$	The boundary condition relative error at the j-th iteration
CC	Convergence criterion (a number)
CDC	Control Data Corporation
CM	Convergence measure
CP	Central processor
D	Diameter
d	A vector defining the orientation of strips used in segment numbering
E	Electric field
EFF	Efficiency
f	The ratio of M to N
g	The efficiency of the BMI process relative to full matrix decomposition, based on the approximate number of mo's
$g_{LIM}$	The upper limit of the efficiency for a given bandwidth
GEMACS	General Electromagnetic Model for the Analysis of Complex Systems
H	Magnetic field
I	Wire current
i	An integer
$IRE_j$	The iterative relative error at the j-th iteration

j	An integer or $\sqrt{-1}$
K	The number of iterations required to satisfy the convergence criterion
k	$2\pi/\lambda$
ka	Object circumference in wavelengths
L	Triangular matrix below B in A, also object length
M	Upper or lower bandwidth of B
mA	Milliamps
mo's	Multiplicative operations
N	Number of wire segments; also the number of unknowns in the equations
PP	Peripheral processor
PRE <sub>j</sub>	The predicted relative error at the j-th iteration
R <sub>M</sub>	The distance within which all segment interactions are to be kept in B
R <sub>W</sub>	Wire radius
RE <sub>j</sub>	The relative error of X
S	Surface Area of Integration
sec	Seconds
U	Triangular matrix above B in A
V	Right-hand side of matrix equation, representing input voltage
VCM	Numerical value of the convergence measure at a given iteration
W	Object width
X	Column vector of current coefficients, also a cartesian coordinate
X <sub>e</sub>	The exact solution of $AX = b$
X <sub>j</sub>	The approximate solution column vector at the j-th iteration
X <sub>0</sub>	The column vector used to start the BMI solution process
Y	A cartesian coordinate or input admittance
Z	A cartesian coordinate or input impedance
Z <sub>j</sub>	A column vector intermediate to the solution process of forward elimination and back substitution
$\lambda$	Wavelength
$\phi$	Spherical coordinate (azimuth)

$||Q||$       The norm (euclidian length) of  $Q$   
†      The complex conjugate transpose

## GEMACS ENGINEERING MANUAL

### A. INTRODUCTION

The function of this manual is to discuss the physical and mathematical methods used in the GEMACS (General Electromagnetic Model for the Analysis of Complex Systems) code to obtain the results desired. There are five basic steps involved in obtaining the observables used to evaluate a particular configuration. These are:

- (1) Geometric Modeling
- (2) Structure Excitation
- (3) Interaction Computation
- (4) Numerical Solution
- (5) Observable Computation

Section B discusses each of these areas as they pertain to the GEMACS code. Section C is a discussion of the BMI (Banded Matrix Iteration) solution technique developed as a result of this project. Section D is a summary of results obtained with BMI for various geometries.

Much of the information in section B is presented in the AMP manuals. Much of the AMP discussion is directly applicable since the basis formalism and some of the code itself is identical to the AMP code. The primary differences are in the geometry and excitation processes and in the use of the BMI technique to obtain a solution.

### B. GEMACS FUNCTIONS

When the GEMACS program was first structured, very little was known of the solution techniques to be implemented. Therefore, the basic functions needed to perform a generic electromagnetic analysis were identified. The input requirements for each function were identified and this specified the output requirements of the logically preceding function. In order



to assure flexibility and modularity, the outputs of each function are symbolically identified data sets. These data sets, along with other parameters are used as inputs to subsequent functions.

Thus, each function will operate on previously defined data or user supplied inputs to generate another data set for subsequent use.

#### 1. Geometric Modeling

Geometric modeling is used to convey structure geometry to the GEMACS code. Since GEMACS uses the EFIE (Electric Field Integral Equation), the actual structure is represented by a series of wire segments connected in a way that approximates the actual surface. In the usual solution technique, the segments are given a number and the number assigned to one segment is totally independent of other segment numbers. This is also true in GEMACS when using the full interaction matrix in the solution; however, when using the BMI technique, it becomes important to number the segments in such a way that segments which are electrically close have numbers which are also close. This is because, for any given row or column of the interaction matrix, a segment's position is determined by its number. Thus, all interactions with segment 1 will be in row 1 and column 1. Much study on numbering has been completed and is summarized in section C. In order to accommodate the need for specific numbering sequence, the RN (Renumber) command has been included in the geometry processor. With this command, the user may enter the model in the most convenient manner and then specify the desired numbering sequence. When reducing the EFIE to a set of simultaneous linear equations, two assumptions are made:

- (1) The wire segments are of sufficiently small radii that circumferential currents may be ignored.
- (2) The current on any segment may be approximated by some function called the basis or expansion function.

These two assumptions have several implications depending on the structure being modeled and the expansion function used. Assumption (1) restricts the wire radius,  $R$ , to something less than a wavelength ( $\lambda$ ). Typically,

$R < \lambda/10$  is quoted as acceptable. If the expansion function is to represent the actual current over the segment, then the segment length,  $L$ , must, in general, also be less than  $\lambda$ . The basis function used in GEMACS is the sine + cosine + pulse expansion with collocation and it has been observed that  $L = \lambda/4$  is sufficient where the current does not vary rapidly and  $L \approx \lambda/10$  is adequate where rapid variations occur. A general rule of thumb for modeling structures is that the total area of the wire segments should approximate the surface area of the structure. In addition, for the expansion function used, a ratio  $L/R \approx 5$  has been found to give consistent agreement with currents obtained from analytic solutions. Using these rules, the number of segments ( $N$ ) for a given frequency may be approximately determined from:

$$\sum_{i=1}^N 2\pi R_i L_i = A$$

$$\sum_{i=1}^N \frac{2\pi L_i^2}{5} = A$$

$$\sum_{i=1}^N \frac{2\pi \lambda^2}{500} = A$$

$$\frac{2\pi N}{500} \lambda^2 = A$$

$$N \approx \frac{80 A}{\lambda^2} \quad (\text{Eq. 1})$$

where A is the surface area to be modeled. With  $N = 800$ , an area of approximately  $10 \lambda^2$  can be represented quite accurately. If less confidence in the observables is acceptable, A may be much larger than indicated. The reader is cautioned that the applicability of these rules to codes employing other methods is largely unknown at this time. A consistent method of modeling has not been established except for the present code.

Once the structure has been defined to the GEMACS code, several operations take place before the next command is executed. The geometry data are scanned to find all segments connected to each other. During this operation, segments which have identical end points are found and all but one of these segments are given a segment and tag number of zero. In this way, segments in planes of symmetry and on axes of rotation are allowed. The criterion for segments being connected is that the end point separation is less than the roundoff error of the host computer. This number is internally computed based on the number of bits used for the mantissa of a floating point number. During this time, any segment which terminates on the XY plane is identified as being connected to a ground plane if one is subsequently specified. If no connections are found, this is also noted for user convenience. Once all of the junctions are found, a list is constructed which identifies the next segment connected to either end of each segment. For example, if end 1 of segments 1, 3, 5, 20, and 75 are connected, then data identifying the next segments would be 3, 5, 20, 75, and 1. This forms a circular linked list identifying all segments connected to either end of a given segment. This information is listed in the geometry output for both end 1 and end 2 of each segment. A negative number implies end 1 of the identified segment while a positive number identifies end 2. Once all junctions are identified and the junction linked list constructed, the geometry data internal format is changed from end point data to centerpoint coordinates, segment length, and direction cosine format. When used, dimensioned geometry data are scaled to wavelength for computational ease.

## 2. Structure Excitation

There are two methods of structure excitation available in the GEMACS code. These are voltage excitation for antennas and a wave excitation for scatterers. These types may be superimposed for composite excitations.

### a. Antenna Source Model

The normal derivation of the currents on a body involves writing the electric field as

$$\bar{E}(X) = \bar{E}^{inc}(X) + \bar{E}^S(X) \quad (\text{Eq. 2})$$

where  $\bar{E}(X)$  is the total electric field at  $X$ ,  $\bar{E}^{inc}(X)$  is the incident electric field, and  $\bar{E}^S(X)$  is the electric field due to some volume distribution of currents. By imposing the boundary condition at a finite number of points on the surface of a perfect conductor and specifying the incident field, we solve for the currents induced on the body.

$$\hat{n} \times \bar{E} = \hat{n} \times \left( \bar{E}^{inc} + \bar{E}^S \right) = 0 \quad (\text{Eq. 3})$$

therefore,

$$\hat{n} \times \bar{E}^{inc} = -\hat{n} \times \bar{E}^S \quad (\text{Eq. 4})$$

In the thin-wire approximation, this condition is enforced on the component of the field in the direction of the wire since the assumption that azimuthal currents are negligible forces the  $\theta$  components to zero, i.e.,

$$\hat{l} \cdot \bar{E}^{inc} = -\hat{l} \cdot \bar{E}^S \quad (\text{Eq. 5})$$



where  $\hat{\ell}$  is a unit vector in the direction of the wire. This condition is enforced at the centerpoint of each segment and no information about  $\bar{E}$  is known between these points. This is equivalent to throwing all of the wires away since wire parameters have no effect on the boundary conditions, but only on the current distribution used to satisfy the boundary condition.

Now, the only way to specify a boundary point to the code is via a wire segment and thus an antenna source must be specified as a wire segment. However, this segment is totally artificial in that  $\hat{n} \times \bar{E}$  along this segment is not zero since  $V = \int \bar{E} \cdot d\bar{\ell}$  is the voltage driving the antenna. Since the boundary condition is only satisfied at the midpoint and the structure of the excitation field is of second order, a uniform excitation gives reasonably good results as long as the excited segment length is much less than  $\lambda$ . Since the total field at the midpoint has been specified, equation 2 can be used by again invoking the thin-wire approximation and taking only the tangential field.

$$\begin{aligned} \hat{\ell} \cdot \bar{E}_{\text{ant}} &= \hat{\ell} \cdot (\bar{E}^{\text{inc}} + \bar{E}^{\text{S}}) \\ \text{or} \quad \hat{\ell} \cdot (\bar{E}^{\text{inc}} - \bar{E}_{\text{ant}}) &= -\hat{\ell} \cdot \bar{E}^{\text{S}} \end{aligned} \quad (\text{Eq. 6})$$

with  $\bar{E}_{\text{ant}} = 0$  at those points not driven as antenna sources.

The solution of equation 6 is a set of currents at the midpoints of each segment and the antenna input admittance can be approximated by:

$$Y \approx \frac{1}{V} \quad (\text{Eq. 7})$$

The shortcomings of this type of model are presented in the AMP Engineering Manual and its references (reference 16).

b. Field Excitation

The incident electric field ( $\bar{E}$ ) on a structure may be either a polarized or nonpolarized field from a plane or spherical wave. Multiple wave excitations may be combined in any order desired.

In general, the field at the observation point  $r$  is given by

$$\bar{E}(r) = \bar{E}_I e^{-jk_i \cdot \bar{r}} + \bar{E}_R e^{-jk_r \cdot \bar{r}} \quad (\text{Eq. 8})$$

where  $\bar{E}_I$  is the source or direct illumination field and  $\bar{E}_R$  is the reflected field. If there is no ground plane,  $\bar{E}_R = 0$ . There are two differences between a spherical and plane wave. The spherical wave has a  $1/R$  amplitude dependence and the wave vector  $\hat{k}$  is always oriented in the direction of the field point from the source point. For a plane wave, the amplitude and  $\hat{k}$  are constant.

In general, the incident or source field is:

$$\bar{E}_I = \bar{E} + j\bar{E}P \quad (\text{Eq. 9})$$

where  $\bar{E}P$  is the polarization component if present.  $\bar{E}P$  is determined from the vector relationship  $\bar{E} \times \bar{E}P = \hat{k}$  and  $ECC = \frac{|\bar{E}P|}{|\bar{E}|}$  where ECC is the user supplied eccentricity.

The reflected field is given by

$$\bar{E}_R = -R_{11} \bar{E}_{11}^P + R_{11} \bar{E}_{11}^n - R_{\perp} \bar{E}_{\perp} \quad (\text{Eq. 10})$$

where

$R_{11}$  is the in-plane reflection coefficient

$R_{\perp}$  is the out-of-plane reflection coefficient

$\bar{E}_{11}^P$  is the in-plane tangential component

$\bar{E}_{11}^n$  is the in-plane normal component

$\bar{E}_{\perp}$  is the out-of-plane component

Let  $\hat{\rho}$  be a unit vector normal to the plane of incidence. Then, with  $\hat{k}_i$  from source to specular point and  $\hat{k}_r$  from specular point to the field point, we have

$$\begin{aligned}\hat{\rho} &= \hat{k}_i \times \hat{k}_r \text{ (unit vector } \perp \text{ to plane of incidence)} \\ \bar{E} &= \bar{E}_{11} + \bar{E}_{\perp}\end{aligned}\quad (\text{Eq. 11})$$

$$\begin{aligned}\bar{E}_{\perp} &= (\bar{E} \cdot \hat{\rho}) \hat{\rho} \\ &= \frac{[-k_y(E_x + jEP_x) + k_x(E_y + jEP_y)]}{(k_x^2 + k_y^2)} \begin{bmatrix} -k_y \hat{i} + k_x \hat{j} \end{bmatrix}\end{aligned}\quad (\text{Eq. 12})$$

$$\bar{E}_{11} = \bar{E} - \bar{E}_{\perp} \quad (\text{Eq. 13})$$

$$\bar{E}_{11}^n = (\bar{E}_{11} \cdot \hat{z}) \hat{z} \quad (\text{Eq. 14})$$

$$\bar{E}_{11}^p = \bar{E}_{11} - \bar{E}_{11}^n \quad (\text{Eq. 15})$$

The reflection coefficients  $R_{11}$  and  $R_{\perp}$  are the modified Fresnel coefficients. This method is discussed at some length in the AMP Engineering Manual (reference 16). Portions of the manual are reproduced as appendix A. The reflection coefficients are:

$$R_{11} = - \frac{\epsilon_E \cos \theta - \sqrt{\epsilon_E - \sin^2 \theta}}{\epsilon_E \cos \theta + \sqrt{\epsilon_E - \sin^2 \theta}} \quad (\text{Eq. 16})$$

$$R_{\perp} = \frac{\cos \theta - \sqrt{\epsilon_E - \sin^2 \theta}}{\cos \theta + \sqrt{\epsilon_E - \sin^2 \theta}} \quad (\text{Eq. 17})$$

$$\epsilon_E = \frac{\epsilon_1}{\epsilon_0} \left( 1 - \frac{j\sigma_1}{\omega\epsilon_1} \right), \quad (\text{Eq. 18})$$

where  $\theta$  is the angle of incidence measured from  $\hat{z}$  and  $\epsilon_1$  and  $\sigma_1$  are the dielectric constant and conductivity of the ground plane. The free space permittivity is  $\epsilon_0$ .

### 3. Interaction Computation

The interaction or structure matrix used in the GEMACS code is formally identical to that found in the AMP code. Minor changes in the data structure have been made; however, given identical geometries, one obtains identical elements in the structure matrix. The derivation involved in obtaining the elements of the structure matrix is presented in chapter 11 of the AMP Engineering Manual portions of which are reproduced here with equation numbers changed to be consistent with numbering in this manual.

#### a. Integral Equation Formulation

The electric field  $\vec{E}$  due to a volume current distribution  $\vec{J}$  is written by means of the Green's dyadic as

$$\vec{E}(\vec{r}_0) = \iiint_V j\omega\mu_0 \vec{J}(\vec{r}) \cdot \vec{\bar{G}}(\vec{r}, \vec{r}_0) dV \quad (\text{Eq. 19})$$

where  $\vec{r}_0$  and  $\vec{r}$  are the observation and source points, respectively, and the Green's dyadic is expressed in the usual notation as

$$\vec{\bar{G}}(\vec{r}, \vec{r}_0) = -(1/4\pi) \cdot [\vec{I} + (1/k^2) \nabla \nabla] g$$

where

$$g = \exp(-jk|\vec{r} - \vec{r}_0|) / |\vec{r} - \vec{r}_0|$$



and  $\bar{\bar{I}}$  is the unit second-rank tensor. The suppressed time variation is  $\exp(j\omega t)$  with  $\omega$  the radian frequency. The plane wave propagation constant is  $k$ , and is related to  $\epsilon_0$  and  $\mu_0$ , the permittivity and permeability of free space, respectively, and  $\omega$  by

$$k = \omega \sqrt{\mu_0 \epsilon_0}$$

Where the current distribution is limited to the surfaces of a perfectly conducting body, equation 19 becomes

$$\bar{E}(\bar{r}_0) = \iint_S j\omega\mu_0 \bar{J}_s(\bar{r}) \cdot \bar{\bar{G}}(\bar{r}, \bar{r}_0) dA \quad (\text{Eq. 20})$$

with  $\bar{J}_s$  the surface current density. If this surface current is induced by an incident electric field  $\bar{E}^I$ , then an integral equation for the unknown surface current  $\bar{J}_s$  can be obtained from equation 20 and the boundary condition that

$$\hat{n}(\bar{r}_0) \times [\bar{E}^S(\bar{r}_0) + \bar{E}^I(\bar{r}_0)] = 0 \quad (\text{Eq. 21})$$

where  $\hat{n}(\bar{r}_0)$  is the unit normal vector at  $\bar{r}_0$  and  $\bar{E}^S$  is the scattered field due to the secondary current distribution. Equating  $\bar{E}^S$  of equation 21 with  $\bar{E}$  of equation 20 yields

$$-\hat{n}(\bar{r}_0) \times \bar{E}^I(\bar{r}_0) = \hat{n}(\bar{r}_0) \times \iint_S j\omega\mu_0 \bar{J}_s(\bar{r}) \cdot \bar{\bar{G}}(\bar{r}, \bar{r}_0) dA \quad (\text{Eq. 22})$$

For the thin-wire approximation, limiting attention to circular cross-section bodies of diameters small compared with the wavelength, the azimuthal current may be neglected, and equation 22 becomes

$$-\hat{n}(\bar{r}_o) \times \bar{E}^I(\bar{r}_o) = \hat{n}(\bar{r}_o) \times \frac{-1}{4\pi} \iint_S \left\{ j\omega\mu_o J_s(\bar{r}) \left[ \hat{s} + \frac{\hat{s} \cdot \nabla \nabla}{k^2} \right] g(\bar{r}, \bar{r}_o) \right\} dA$$

(Eq. 23)

where  $\hat{s}$  is the unit tangent vector at  $\bar{r}$  pointing in the direction of the current. A scalar integral equation for the current is obtained by taking the dot product of equation 23 with the unit tangent vector  $\hat{s}_o$  at the observation point  $\bar{r}_o$  as

$$-\hat{s}_o \cdot \bar{E}^I(\bar{r}_o) = \frac{-1}{4\pi} \iint_S j\omega\mu_o J_s(\bar{r}_o) \left[ \hat{s} \cdot \hat{s}_o + (\hat{s} \cdot \nabla)(\hat{s}_o \cdot \nabla) \frac{1}{k^2} \right] g(\bar{r}, \bar{r}_o) dA$$

(Eq. 24)

If the assumption is now made that  $J_s$  is independent of the azimuthal variable, equation 24 can be written

$$-\hat{s}_o \cdot \bar{E}^I(\bar{r}_o) = \frac{-1}{4\pi} \int_L ja\omega\mu_o J_s(s) \int_0^{2\pi} \left[ \hat{s} \cdot \hat{s}_o - \frac{1}{k^2} \frac{\partial^2}{\partial s \partial s_o} \right] g(\bar{r}, \bar{r}_o) d\phi ds$$

(Eq. 25)

where  $a$  is the wire radius and the  $s$  integration is over the entire length of wire  $L$ . A final approximation is that the current may be realistically represented as a filament of strength  $I_s(s) = 2\pi a J_s(s)$  flowing on the wire axis while the field is evaluated on the wire surface, allowing equation 25 to be written

$$-\hat{s}_o \cdot \bar{E}^I(\bar{r}_o) = (-j\omega\mu_o/4\pi) \int_L I_s(s) \left[ \hat{s} \cdot \hat{s}_o - \frac{1}{k^2} \frac{\partial^2}{\partial s \partial s_o} \right] g(\bar{r}, \bar{r}_o) ds$$

(Eq. 26)

where  $|\bar{r} - \bar{r}_0|$  is now measured from the wire axis, or source point, to the observation point on the surface, which can thus never be closer than the wire radius  $a$ . By considering the current as a tubular sheet centered on the wire axis while evaluating the electric field at the wire axis, one can resolve the ambiguity in the azimuth involved. The form of equation 26 is not changed using this convention, but the interpretation of the tangential field evaluation is simplified when nonparallel, nonplanar wires are considered.

The thin-wire approximation which leads from the electric field integral for a surface current distribution to equation 26 involves the assumption that the wire radius  $a \ll \lambda$  so that: (1) azimuthal current flow around the wire may be neglected; (2) the longitudinal current is independent of azimuth and may be represented as a filament along the wire axis; and (3) that the surface integration can be replaced by a line integration along the wire at a radial distance  $a_n$  so that the minimum source-to-observation point distance is  $a_n$  thus avoiding the singularity in the kernel of the integral which would occur at  $\bar{r} = \bar{r}_0$ .

This thin-wire approximation has been applied to radiation and scattering problems with a great deal of success. Until fairly recently, for example, linear antenna theory was almost exclusively restricted to the thin-wire approach; the same observation applied to scattering from finite length cylinders. At the same time, the antenna and scattering solutions were largely confined to dipoles on the order of a few wavelengths long. This results, for the most part, from the approximate analytic approaches required due to the difficulty involved in obtaining a numerical solution of the integral equation. While Wu (1960) and Chen (1968) extended the analytic methods developed by Hallen (1938) and King (1956) to antenna and scatterers without this length restriction, their results are quite complicated in form and in addition have not been subjected to extensive experimental comparison.

The reason for concentration on analytic solutions to the integral equation, until the past few years, was the lack of sufficiently powerful computers to provide the capability to obtain a completely numerical solution. With the present development of both high-speed computers and advanced methods of numerical analysis this is no longer the case: significant progress has been made in extending accurate numerical solutions to more complex geometries. In the following section, the method of solution will be outlined for the electromagnetic properties of structures to which the thin-wire integral equation is applicable.

b. Reduction to a Linear System (Collocation)

A numerical solution to an integral equation may perhaps be best undertaken using the method of moments. This is a well-founded mathematical technique for finding the unknown by forcing the integral equation to be satisfied in some prescribed fashion over the range of the integral operator. GEMACS is based on the thin-wire electric field integral equation.

Equation 26 may be written symbolically as:

$$\mathcal{L}(f) = g \quad (\text{Eq. 27})$$

following Harrington's (1968) notation. The solution of equation 26 (or of equation 27) is obtained by the method of moments. An intuitive approach to solving equation 27 for the unknown function  $f$  is to set  $f$  equal to a constant  $f_i$  within  $N$  subintervals of the domain of  $\mathcal{L}$ , and to require equation 27 to be satisfied at  $N$  points over the range of  $\mathcal{L}$ , obtaining  $N$  equations in the  $f_i$  unknowns. This is a specialized application of the method of moments which is more generally written as follows. Let

$$f = \sum a_n f_n$$

with the basis function  $f_n$  defined in the domain of  $\mathcal{L}$  so that equation 27 may be written



$$\sum a_n \mathcal{L}(f_n) = g \quad (\text{Eq. 28})$$

Then, with the set of weighting functions  $w_m$ , defined in the range of  $\mathcal{L}$ , the inner product denoted by  $\langle \rangle$  is formed as

$$\sum a_n \langle w_m, \mathcal{L}(f_n) \rangle = \langle w_m, g \rangle \quad (\text{Eq. 29})$$

where  $m = 1, 2, 3, \dots$ . Equation 29 can be written in matrix form as

$$[G_{mn}] [a_n] = [S_m]$$

where

$$G_{mn} = \langle w_m, \mathcal{L}(f_n) \rangle$$

and

$$S_m = \langle w_m, g \rangle$$

and the matrix  $G_{mn}$  is referred to as the structure matrix. If the inverse of  $G_{mn}$  exists, then the  $a_n$  can be found, and thus, the function  $f$ , which is the desired solution, for any specified source function  $S_m$ .

The proper choice of weight functions and basis functions, as well as the subsectioning of the domain of  $\mathcal{L}$ , is not an obvious one. Although there is some leeway in the matter, careful consideration of the physics of the problem and the nature of the expected solution will show that some representations for the  $f_n$  will be more efficient than others in terms of computer time and accuracy. Constant, linear, quadratic, trigonometric, and Fourier series have all been used for this role. The weighting functions have generally been more restricted in choice than  $f_n$ . The special case  $w_n = f_n$  is referred to as Galerkin's method.

More often, the weights are  $\delta$ -functions, a method referred to as collocation, so that the inner product equation 29 merely becomes the sequence of values  $\oint (f_n)_m$  and  $g_m$ . These are, respectively, the tangential electric fields due to current segment  $n$  at observation point  $m$  and the tangential incident electric field at observation point  $m$ .

c. Current Expansion

The GEMACS program employs the collocation method with constant, sine and cosine terms for the  $f_n$  segment or current function, i.e.,

$$I(s) = \sum_{j=1}^N U_j(s) [A_j + B_j \sin k(s-s_j) + C_j \cos k(s-s_j)] = \sum_{j=1}^N U_j(s) I_j(s) \quad (\text{Eq. 31})$$

where  $U_j(s)$  is 1 when  $s$  is on segment  $j$  and zero otherwise. Equation 31 appears disadvantageous because three constants are required to specify the current on each segment, so that apparently  $3N$  linear equations need be solved; however, it is not necessary to employ the integral equation itself to find the extra unknowns introduced by the sinusoidal expansion. Two of the three constants for each segment may be obtained by requiring the current in adjacent segments to satisfy some specified mutual conditions. In the GEMACS thin-wire program, the extrapolated current from a given segment is forced to match the center current values in two adjacent segments to satisfy the required condition for two-wire junctions as follows.

Let the current on segment  $j$  be expressed as

$$I_j(s) = A_j + B_j \sin k(s-s_j) + C_j \cos k(s-s_j) \quad (\text{Eq. 32})$$

with  $s_j$  the midpoint coordinate (Yeh and Mei, 1967). Also, let segment  $j$  be connected to segments  $j-1$  and  $j+1$  at its minus and plus reference ends respectively with the reference directions on all three segments the same. Evaluation of  $I_j$  at  $s_j$ ,  $s_{j-1}$ , and  $s_{j+1}$  results in

$$A_j + C_j = I_j$$

$$A_j + B_j s_{j-1,j} + C_j c_{j-1,j} = I_{j-1} \quad (\text{Eq. 33})$$

$$A_j + B_j s_{j+1,j} + C_j c_{j+1,j} = I_{j+1}$$

where  $d_j$  is the length of the  $j^{\text{th}}$  segment and

$$\left. \begin{array}{l} s \\ c \end{array} \right|_{j \pm 1, j} = \frac{\sin}{\cos} \left[ k(d_{j \pm 1} + d_j)/2 \right]$$

Solution for  $A_j$ ,  $B_j$ , and  $C_j$  in terms of  $I_{j-1}$ ,  $I_j$ , and  $I_{j+1}$  provides an equation of the form

$$I_j(s') = X_j(s') I_{j-1} + Y_j(s') I_j + Z_j(s') I_{j+1} \quad (\text{Eq. 34})$$

where  $X_j$ ,  $Y_j$ ,  $Z_j$  contain the coefficients  $A_j$ ,  $B_j$ ,  $C_j$ . The system of equations which results from the collocation solution to the integral equation is thus seen to involve as unknowns the  $N$  current samples at the centers of the  $N$  segments into which the structure is divided.

The extension of the interpolation procedure to multiple junctions is straightforward. Consider the case where segment  $j$  is connected to  $m$  segments numbered  $j+1, \dots, j+m$  at its plus end and

the single segment  $j-1$  at its minus end. Then only the equation representing equation 32 evaluated at  $s_{j+1}$  is modified and becomes

$$A_j + \frac{1}{m} \sum_{i=j+1}^{j+m} (B_j s_{i,j} + C_j c_{i,j}) = \frac{1}{m} \sum_{i=j+1}^{j+m} I_i \quad (\text{Eq. 35})$$

which comes from interpolating  $I_j$  to the midpoints of the  $m$  connected wires where it is equated to the average midpoint value. A solution for the  $A_j$ ,  $B_j$  and  $C_j$  in terms of the midpoint currents  $I_{j-1}$ ,  $I_{j+1}$ , ....  $I_{j+m}$  follows as before. A multiple junction at the minus end of the segment is similarly treated.

The sinusoidal current expansion appears to make the system of equations resulting from collocation somewhat more involved. But the required computer time is not significantly increased when compared with the same number of current unknowns without using the sinusoidal expansion. Other current expansion functions-linear, quadratic, Fourier series-could be used in place of the constant-sine-cosine expression, but this particular expansion has a number of additional advantages over the other possibilities mentioned. For instance, a solution for the current to a specified accuracy for a half-wave dipole scatterer and antenna requires the fewest current segments using the sinusoidal expansion (Neutreuther, et al., 1968). This advantage would be expected to carry over to more complex geometries. Second, the solution will more accurately exhibit the required dependence on wire radius (Andreason, 1968) because the constant current term produces infinite tangential electric field on the current axis, as opposed to the sine and cosine terms which do not.

Third, the parallel and perpendicular electric field components (due to the sine and cosine current terms) and the tangential field components (due to constant current terms) may be analytically evaluated. This eliminates the necessity for extensive numerical integration to evaluate all the elements in the coefficient matrix



$G_{mn}$ . Only the perpendicular electric field excited by the constant current terms requires numerical integration and this is handled by applying the Romberg variable-interval width technique to the difference integrand. This is discussed in the appendix of the AMP Engineering Manual.

d. Calculation of the Structure Matrix

The form of the matrix elements which result from applying the method of collocation to equation 26 is considered in the following discussion. Each entry  $G_{ij}$  in the structure matrix represents the tangential electric field at observation point  $i$  on the structure produced by unit current flowing on segment  $j$ . The boundary condition on the tangential electric field is enforced at each observation point. The collocation method of solving the integral equation is thus basically one of calculating electric field components at specific points due to the current induced on the structure.

The thin-wire approximation involves the explicit assumption that the effects of azimuthal currents can be neglected in comparison with those of axially directed currents and that, in addition, the cylindrical tube of axial current has no azimuthal dependence. The former assumption allows one to consider only one current component rather than two, while the latter provides partial justification for reducing the surface integral to a line integral. It may be deduced from an examination of equations 25 and 26, however, that even where  $J_s$  is independent of  $\phi$ , the kernel of the integration equation depends in general upon both  $\phi$  and  $s$ . However, the integrand is independent of  $\phi$  in the special case where the observation point is located on the axis of a linear tube of current, and the  $\phi$  integration of equation 25 may be replaced without approximation by the factor  $2\pi$ .

Consequently, the observation points are located where the tangential electric field is to be calculated, on the axis rather than on the surface of each wire segment. The  $\phi$  integration in equation 25 is thus exact for the self-field as well as the mutual fields for

all current segments having a common axis. In addition, the possible ambiguity involved in evaluating the incident field over a  $2\pi$  variation in  $\phi$  on the wire surface is resolved. As a final point, the observation point is always at least as far as the wire radius from the source point.

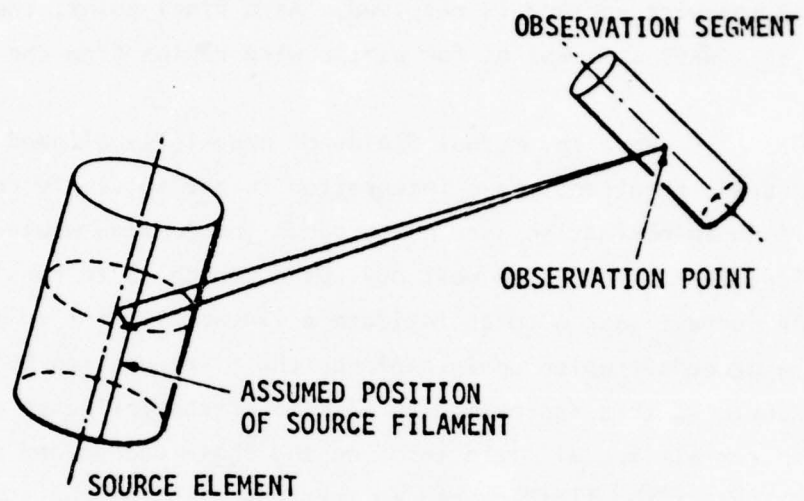
When the mutual fields of nonaxially aligned current segments are required, the  $\phi$  integration is not so simply performed. And, if no approximation were used, the  $\phi$  integration would require numerical evaluation. The most obvious approach is to consider the tubular current source to approximate a linear filament on the wire axis, a procedure which again replaces the  $\phi$  integration by a  $2\pi$  factor. Unfortunately, this approximation eliminates the influence of the wire radius from all mutual field terms on the phase change and geometrical attenuation of the field caused by the separation of the source and observation points.

An alternative to the above method is replacement of the current tube by a current filament which is not located on the wire axis but is displaced in distance from it by the wire radius. The direction of displacement is perpendicular to the plane of the wire axis and the line joining the observation point and wire axis midpoint (the observation point for the self term field). The geometry of this method is shown in figure 1. The improved agreement obtained between theory and experiment for a 16-sided regular polygon backscatter cross section demonstrates that this approach is more realistic.

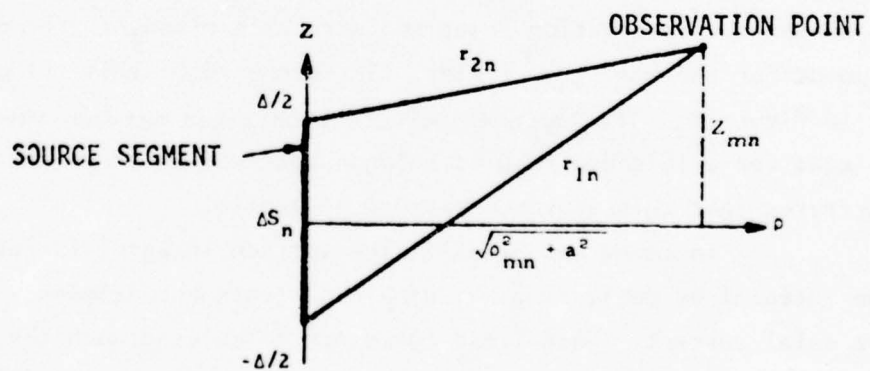
To summarize briefly, the surface integral is reduced to a line integral by neglecting azimuthal<sup>1</sup> currents and azimuthal variation of the axial current. Self-field terms are calculated with the observation point on the axis of a cylindrical current tube, while mutual field terms are calculated at the same observation point with the current represented as a filament displaced from the wire axis by the wire radius.

---

<sup>1</sup>Taken here to mean the direction measured along the intersection of the current tube surface with a plane perpendicular to the axis of the current tube.



(a) Thin wire current approximation



(b) Geometric parameters for field evaluation

Figure 1. Geometry of Current Filament

The integral equation 26 can now be written in the form

$$E_m^I = (j\omega\mu_0/4\pi) \sum_{n=1}^N \int_{\Delta S_n} \left[ \hat{s}_m \cdot \hat{s}_n - \frac{1}{k^2} \frac{\partial^2}{\partial s \partial s_m} \right] g(r_m, r) I_n(s) ds \quad (\text{Eq. 36})$$

$m = 1, \dots, N$

where  $\Delta S_n$  denotes the length of segment  $n$ ,  $E_m^I$  is the tangential component of the incident electric field at the  $m^{\text{th}}$  segment, and

$$g(r_m, r) = \frac{\exp \left[ -jk \sqrt{\rho^2 + (s_m - s)^2} \right]}{\sqrt{\rho^2 + (s_m - s)^2}} \quad (\text{Eq. 37})$$

It should be noted that the integration over  $L$  has been reduced to a summation of  $N$  separate straight-wire segment integrals. It is convenient to rewrite equation 36 in terms of cylindrical coordinates referred to the wire segment being integrated. Then one obtains

$$E_m^I = (j\omega\mu_0/4\pi) \sum_{n=1}^N \int_{\Delta z_n} \left[ \hat{z}_n \cdot \hat{s}_m - \frac{1}{k^2} \frac{\partial^2}{\partial z_n \partial s_m} \right] g(r_{mn}, z_n) I_n(z_n) dz_n \quad (\text{Eq. 38})$$

where

$$g(r_{mn}, z_n) = \exp(-ikr_{mn})/r_{mn} \quad (\text{Eq. 39})$$

$$r_{mn} = \sqrt{(z_{mn} - z_n)^2 + \rho_{mn}^2 + a_n^2} \quad (\text{Eq. 40})$$



$a_n$  is the radius of wire segment  $n$ , and  $\rho_{mn}$  and  $z_{mn}$  are the radial and  $z$ -coordinates of the observation point at the center of segment  $m$  referred to the midpoint of segment  $n$ , as shown in figure 1.

e. Impedance Loading

The discussion has thus far been limited to the case of a perfectly conducting scatterer. The approach may be generalized to allow for loading of the structure by introducing a voltage drop term in the integral equation. If the impedance loading per unit length on segment  $m$  is  $Z_m$ , then equation 38 becomes

$$E_m^I - I_m Z_m = \text{same right-hand side} \quad (\text{Eq. 41})$$

f. Current Solution

Having evaluated the mutual impedance elements (the structure matrix), equation 26 can be written in matrix notation as

$$\sum_{j=1}^N G_{ij} I_j = -E_i^I \quad i = 1, 2, \dots, N \quad (\text{Eq. 42})$$

where  $G$  is the structure matrix,  $I_j$  is the unknown current at wire segment  $j$ , and  $E_i^I$  is the incident tangential field at segment  $i$ . Equation 42 is solved in the form

$$I_j = - \sum_{j=1}^N G_{ij}^{-1} E_i^I \quad (\text{Eq. 43})$$

The operation implied by this equation may be accomplished via inversion, factorization of the  $G$  matrix, or by iteration. In the collocation solution of the wire-antenna problem used in the GEMACS program for arbitrary thin-wire structures, the solution of equation 43 for the current will represent the major portion of computer program execution time for complex structures containing a large number of segments. It is, therefore, of the utmost importance to have efficient solution procedures available for this type of structure.

#### 4. Solution Process Implementation

The basic solution process involves decomposing the structure matrix [G] (or that portion of it extracted for a BMI solution), performing forward elimination and back substitution, and performing matrix multiplication. The performance of these functions is straightforward when all of the data reside in core. However, GEMACS was designed to handle large problems and thus core resident routines are not very efficient. The primary function is that of decomposing a matrix into an upper and lower triangular matrix when none of the matrices will fit in core storage. The algorithm employed in GEMACS is specifically tailored to the data storage method for matrices. All matrices are stored by column, that is, each column requires a separate read and write. For this discussion, a column will be referred to as a record. While this is obviously not the best I/O scheme, it is likely to be fairly good since larger problems typically require several hundred elements and each record will contain twice that number of entries since the matrix is complex. Therefore, the system buffer for I/O will be quite adequately used with a single record. Enlarging the buffers usually increases the core size and will not significantly reduce run time. In addition, all I/O is in ANSI FORTRAN IV for compatibility with a large number of machines.

The function of the solution processor is to find the solution  $I$  to the set of simultaneous linear equations:

$$GI = V \quad (\text{Eq. 44})$$

The method employed is known as lower/upper triangular decomposition which is a variant of Gaussian elimination. The matrix  $G$  is decomposed into lower ( $L$ ) and upper ( $U$ ) triangular matrices such that

$$G = L U$$

then

$$G I = V$$

$$L U I = V$$

$$U I = L^{-1} V = Y$$

and

$$I = U^{-1} Y$$

Note that the inverses of L and U are never found and the notation is used to show the solution logic only. Also, the inverse of G is not found unless explicitly requested.

When decomposing a matrix, one proceeds down the diagonal modifying all elements below and to the right of the diagonal by operations performed upon elements of the diagonal row and column. Thus, once the  $i^{\text{th}}$  diagonal element has been used, all column elements below and row elements to the right of the diagonal will not be referenced again. These are the elements of the lower and upper triangular matrices and may be written out immediately to their respective files. Likewise, the elements of the square submatrix remaining may be written to a peripheral file and when all of the elements have been processed, all future elements reside in this square submatrix which is smaller by one row and column than the source. This procedure is repeated  $N-1$  times where  $N$  is the dimension of the original matrix. In this way, the point is reached where the entire remaining submatrix will fit in core and may be decomposed using normal codes. This procedure is illustrated in figure 2 for the first three diagonal elements of a  $10 \times 10$  matrix.

Note that even though the elements of the upper triangular matrix are row elements, they will be stored as column elements. This will be compensated for during the elimination process.

The types of decomposition encountered are referred to as row or column decomposition depending on the sequence of operations performed. GEMACS employs column decomposition and diagonal pivoting; that is, no row or column interchanges take place. The lack of interchanging rows or

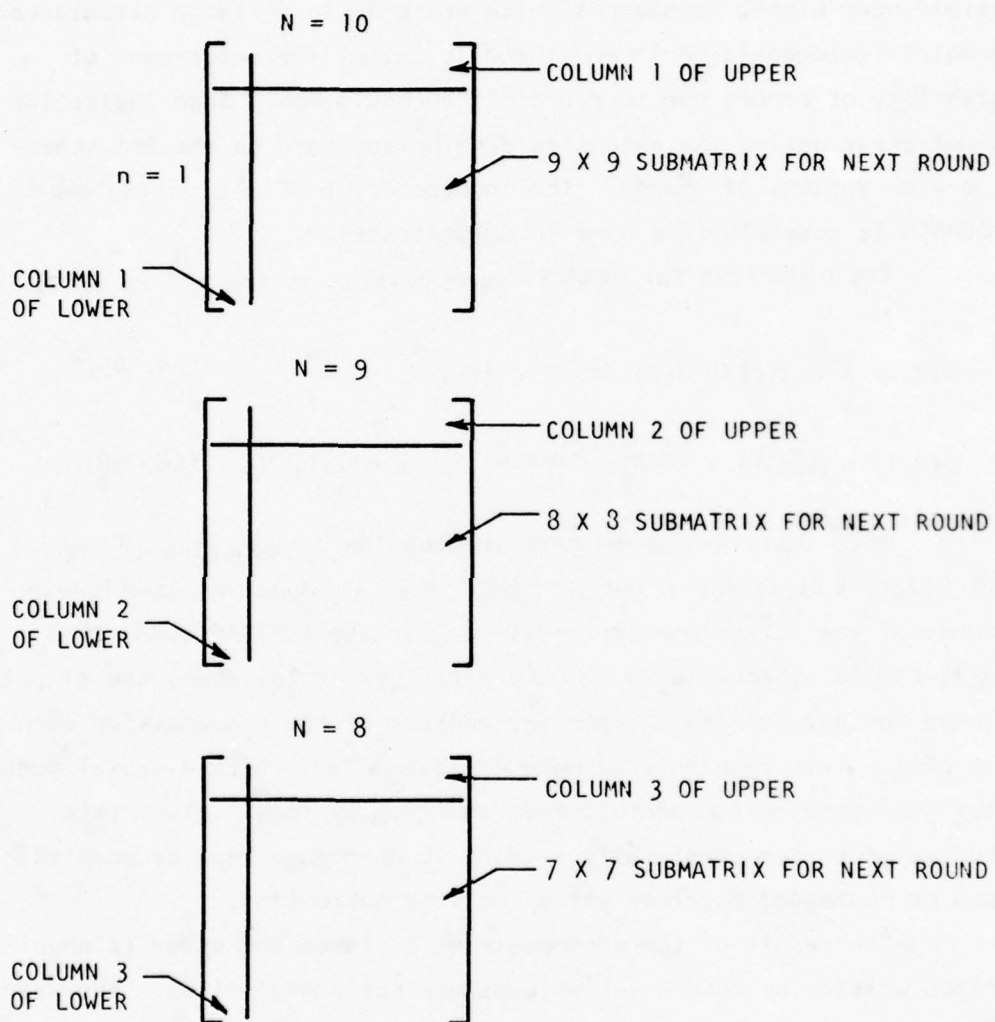


Figure 2. Illustration of Matrix Reduction During Decomposition



columns may lead to problems for ill-conditioned matrices; however, the matrices generated by GEMACS do not display this characteristic except possibly near high-Q resonances which are unlikely on large structures. The matrix decomposition is monitored to detect the occurrence of instability or errors due to round-off accumulation. Such indication did not occur during the extensive development work on the BMI scheme for a wide variety of shapes. The incorporation of a pivoting capability in GEMACS is possible if a need is demonstrated.

The algorithm for GEMACS decomposition at the  $J^{\text{th}}$  round is:

$$G(J,I) = G(J,I)/G(J,J) \text{ for } I = J+1, N \quad (\text{Eq. 45})$$

$$G(K,I) = G(K,I) - \frac{G(J,I)*G(K,J)}{G(J,J)} \text{ for } K = J+1, N \quad (\text{Eq. 46})$$

Note that the second term in equation 46 contains the constant  $G(J,I)/G(J,J)$  for  $I$  and  $J$  fixed. Then as  $K$  varies, contiguous elements of the  $I^{\text{th}}$  column are modified. In the FORTRAN code, this permits simple subscripts to be used with incremental steps and alleviates the need for determining the storage address of the elements for each value of  $I$ . This results in a more efficient code which executes much faster than codes which perform decomposition by rows. Also, this method makes it computationally simpler to decompose real or complex, banded or nonbanded matrices using the same subroutine.

The result of the decomposition is lower and upper triangular matrices written by record to two separate peripheral files. The matrices could have been combined, however, they are never both needed simultaneously. Therefore, more of each will fit into the available core using this method. Normally one of the matrices will have ones (1) on the diagonal while the other will have the diagonal elements as modified by decomposition. The GEMACS code places the diagonal elements on both matrices since, if the original matrix was transposed (as in the case

for the GEMACS structure matrix) the role of the lower and upper matrices is interchanged. If L and U are the lower and upper matrices resulting from decomposition of G, then

$$G = LU \quad (\text{Eq. 47})$$

$$G^T = (LU)^T$$

$$= U^T L^T$$

$$G^T = L^T U^T \quad (\text{Eq. 48})$$

where  $L^T$  and  $U^T$  are the lower and upper triangular matrices obtained from transposing U and L. Therefore, the role has reversed and the logic has been incorporated in the GEMACS code to always assume the lower triangular matrix has unit diagonal elements.

Using the algorithm described above, GEMACS needs room for only three columns of the matrix in core in order to perform the decomposition (2 columns for decomposition and 1 column to accumulate the elements of the upper triangular matrix). The lower matrix is stored on a scratch file.

Once the matrix has been decomposed, the data to be used in the lower matrix are recovered by column until the available core storage is used. Forward elimination is the process of solving the system

$$LY = V \quad (\text{Eq. 49})$$

where V is the original right-hand side and Y is originally the null vector. Storage for Y is not actually required since V may be overwritten. The elements of V are modified according to

$$v_i = v_i - \sum_{j=1}^{i-1} l_{ij} v_j \quad (\text{Eq. 50})$$

where  $l_{ij}$  is an element of the lower triangular matrix. It is seen that the element  $v_i$  depends only on the elements  $v_j$  which precede it, thus the name, forward elimination. Therefore,  $v_i$  may be accumulated for those rows of  $V$  for which the columns of  $L$  are in core. Note that the elements of  $L$  were written out as a column even if  $G$  is a transposed matrix since the rows of  $U$  become the columns of  $L$ .

Once  $Y$  is found, the system that remains is

$$UI = Y \quad (\text{Eq. 51})$$

where  $U$  is the upper triangular matrix with 1 row per record,  $I$  is the solution vector, and  $Y$  is  $L^{-1}V$  or a modified right-hand side. Since  $U$  is a lower triangular matrix, one starts at the bottom and works back up the right hand side. The elements of  $I$  again overwrite  $Y$  or  $V$  and are given by

$$v_i = \left( v_i - \sum_{j=i+1}^N u_{ij} v_j \right) / u_{ii} \quad (\text{Eq. 52})$$

where  $u_{ij}$  is an element of the upper triangular matrix. Since the last elements of  $U$  are needed first, the GEMACS code will determine how many rows will fit and fetch the data in the proper sequence. Since ANSI FORTRAN does not support random access I/O, this can be a time consuming and expensive process for very large matrices. This expense, as well as the expense of decomposition, is considerably reduced for banded matrices, however, when using BMI, the solution process is repeated for each iteration. A detailed discussion of BMI is presented in section D.

Implicit in using BMI is the matrix multiplication involved in finding the RHS (right-hand side) at each iteration,  $i$ , prior to the solution of equation 49.

$$\text{RHS}_i = V - (GL + GU) I_{i-1} \quad (\text{Eq. 53})$$

The elements of equation 53 are matrices where GL and GU are those parts of the structure matrix not included in the band. V is the excitation and  $I_{i-1}$  is the last solution obtained. Remembering that we have core storage for at least three columns of the structure matrix,  $V_i$ ,  $I_{i-1}$ , and one column of G will fit in core. The elements of GL and GU remain imbedded in G. The elements of RHS for a bandwidth of M are (where i and j are subscripts of the matrices):

$$RHS_i = V_i - \sum_{\substack{j < i-m \\ j > i+m}}^N (GL_{ij} + GU_{ij}) I_j \quad (Eq. 53(a))$$

and are accumulated as the blocks G are read into core. The same technique of partial sum accumulation may be used to multiply matrices together which will not fit into core, and it is even more efficient than conventional methods when they do fit, since again, the innermost FORTRAN DO loops reference continuous data, and thus, an optimizing compiler will not generate the indexing locations code.

In discussing how to handle large matrices, the idea of very large core machines usually comes up. While such machines exist, few can directly access very large arrays. For instance, while the CDC 7600 may have 1 million words of LCM (Large Core Memory), only 131,000 words may be addressed in any single array. This is due to the size of the address word used by the compiler in indexing computations. It is highly unlikely that anyone is going to be willing to dedicate more than 18 bit words to address storage, and thus, 131,000 is the limit. Without assembly language routines, this necessitates the use of out-of-core techniques and GEMACS has been specifically designed for this within the constraints imposed by ANSI FORTRAN IV.

##### 5. Observables Computation

The GEMACS code will compute the near and far electric field upon request. These quantities are computed exactly as in the AMP code. Portions of the AMP Systems Manual describing the AMP subroutines EFLD and FFLD are reproduced here. The GEMACS code does not include the ground wave capability present in the AMP code.



The far electric field due to line currents can be written

$$\bar{E}(\bar{r}) = j\omega\mu_0 \frac{e^{-jk r}}{4\pi r} \left[ \left( \hat{k} (\hat{k} \cdot \int e^{j\bar{k} \cdot \bar{r}'} \bar{T}(\bar{r}') d\ell) \right) - \int e^{j\bar{k} \cdot \bar{r}'} \bar{T}(\bar{r}') d\ell \right] \quad (\text{Eq. 54})$$

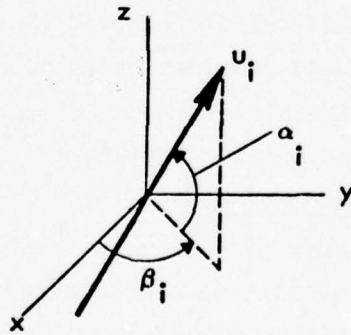
where  $\bar{r}$  is the position vector of the observation point,  $\bar{r}'$  is the position vector of the source point,  $\bar{k}$  is in the direction of propagation with a magnitude of  $2\pi/\lambda$ . Specialized to straight wire segments as used in the GEMACS formulation

$$\bar{E}(\bar{r}) = j \frac{\eta_0}{4\pi} \frac{e^{-jk r}}{r/\lambda} \sum_{i=1}^N e^{j\bar{k} \cdot \bar{R}_i} \left[ \hat{k} (\hat{k} \cdot \bar{Q}_i) - \bar{Q}_i \right] 2\pi \quad (\text{Eq. 55})$$

where  $\eta_0$  is free space impedance,  $\bar{R}_i$  is the position vector of the center of the  $i^{\text{th}}$  segment and

$$\bar{Q}_i = \hat{u}_i \int_{-(S/2)}^{S/2} e^{j2\pi(\hat{k} \cdot \hat{u}_i)t} \frac{I_i(t)}{\lambda} dt$$

where  $\hat{u}_i = \cos \alpha_i \cos \beta_i \hat{x} + \cos \alpha_i \sin \beta_i \hat{y} + \sin \alpha_i \hat{z}$  which is the reference direction of the  $i^{\text{th}}$  segment with the angles defined as shown below,  $t\hat{u}_i = \bar{r}'/\lambda - \bar{R}_i/\lambda$ , and  $s$  is the segment length in wavelengths.



With

$$I_i(t)/\lambda = A_i + B_i \sin 2\pi t + C_i \cos 2\pi t$$

integration of  $Q_i$  yields

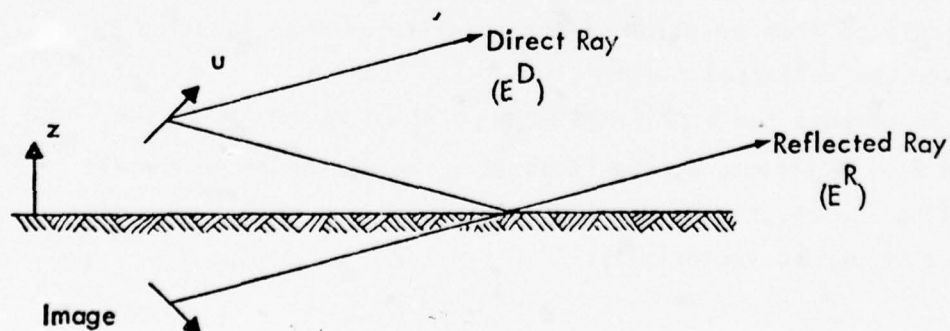
$$\begin{aligned} \bar{Q}_i = \hat{u}_i \left[ A_i \frac{\sin \pi w_i s}{\pi w_i} + j B_i \left( \frac{\sin \pi(1 + w_i)s}{2\pi(1 + w_i)} - \frac{\sin \pi(1 - w_i)s}{2\pi(1 - w_i)} \right) \right. \\ \left. + C_i \left( \frac{\sin \pi(1 + w_i)s}{2\pi(1 + w_i)} + \frac{\sin \pi(1 - w_i)s}{2\pi(1 - w_i)} \right) \right] \end{aligned} \quad (\text{Eq. 56})$$

$$\text{where } w_i = -\hat{k} \cdot \hat{u}_i \quad (\text{Eq. 57})$$

Note, the term  $\hat{k} (\hat{k} \cdot \bar{Q}_i)$  in equation 55 is completely radial and cancels the radial component of  $\bar{Q}_i$ . This term is ignored in GEMACS since the desired transverse components will be computed by a dot product. Thus for program use only and with the understanding that only transverse components will be used, we write

$$\bar{E}(\bar{r}) = -j \frac{\eta_0}{4\pi} \frac{e^{-jkr}}{r/\lambda} \sum_{i=1}^N e^{j\bar{k} \cdot \bar{R}_i} 2\pi \bar{Q}_i \quad (\text{Eq. 58})$$

Ground effects are included by means of an image and the appropriate reflection coefficients. The  $z$  component of the segment; reference direction vector  $\hat{u}$  changes sign for the image as shown



Using this convention, the reflected field can be written in terms of the image field ( $\vec{E}^I$ ) as

$$\begin{aligned}\vec{E}^R &= R_{\perp} (\vec{E}^I \cdot \hat{p}) \hat{p} + R_{11} [\vec{E}^I - (\vec{E}^I \cdot \hat{p}) \hat{p}] \\ &= R_{11} \vec{E}^I + (R_{\perp} - R_{11}) (\vec{E}^I \cdot \hat{p}) \hat{p}\end{aligned}\quad (\text{Eq. 59})$$

where  $\hat{p}$  is a unit vector perpendicular to the plane of incidence,

$$\begin{aligned}R_{\perp} &= \frac{\cos \theta - \sqrt{\epsilon_E - \sin^2 \theta}}{\cos \theta + \sqrt{\epsilon_E - \sin^2 \theta}} \\ R_{11} &= -\frac{\epsilon_E \cos \theta - \sqrt{\epsilon_E - \sin^2 \theta}}{\epsilon_E \cos \theta + \sqrt{\epsilon_E - \sin^2 \theta}}\end{aligned}$$

are the reflection coefficients for the image field perpendicular and parallel, respectively, to the plane of incidence,

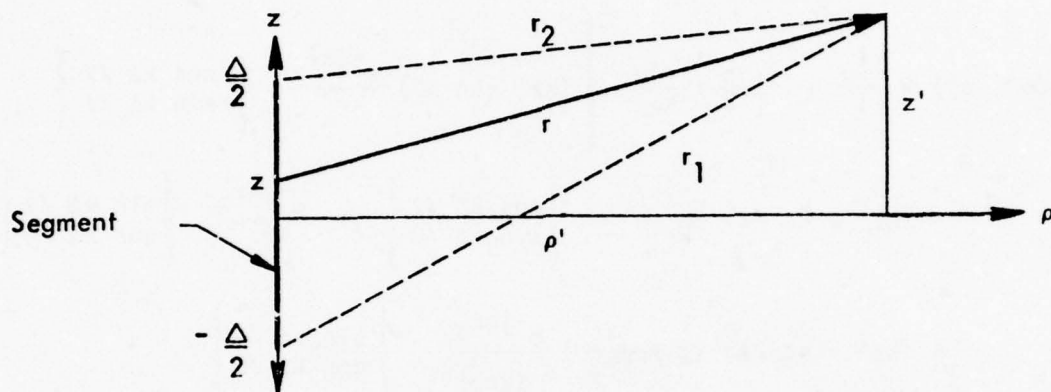
$$\epsilon_E = \frac{\epsilon_1}{\epsilon_0} \left( 1 - \frac{j\sigma_1}{\omega\epsilon_1} \right),$$

and  $\theta$  is measured from  $\hat{z}$ .

For a semi-infinite ground, the electric field of the image can be calculated from equation 55 and substituted into equation 59 to calculate the reflected field.

To compute the near field at a point in space due to the current on a wire structure, the field is computed for three current distributions: sine, cosine, and constant functions on all wire segments and then summed vectorially.

The wire segment is considered to be located at the origin of a local cylindrical coordinate system with the point at which the field is computed being  $(\rho', \phi', z')$ . The geometry for a filament of current of length  $\Delta$  is shown below.



For a sine or cosine current distribution, the field can be written in closed form.<sup>1</sup> The  $\rho$  and  $z$  field components for a current

$$I_0 \begin{Bmatrix} \sin kz \\ \cos kz \end{Bmatrix} \text{ are:}$$

$$E_z(\rho', z') = \frac{I_0}{\lambda} j \frac{\eta}{2} \left[ \frac{e^{-jkr_2}}{kr_2} \begin{Bmatrix} \cos k\Delta/2 \\ -\sin k\Delta/2 \end{Bmatrix} - \frac{e^{-jkr_1}}{kr_1} \begin{Bmatrix} \cos k\Delta/2 \\ \sin k\Delta/2 \end{Bmatrix} \right. \\ \left. - \left( j + \frac{1}{kr_2} \right) \frac{e^{-jkr_2}}{(kr_2)^2} (kz' - k\Delta/2) \begin{Bmatrix} \sin k\Delta/2 \\ \cos k\Delta/2 \end{Bmatrix} \right]$$

<sup>1</sup>Stratton, J. A., Electromagnetic Theory, McGraw Hill Book Co., New York, 1941, p.454.



$$+ \left( j + \frac{1}{kr_1} \right) \frac{e^{-jkr_1}}{(kr_1)^2} (kz' + k\Delta/2) \left\{ \begin{array}{c} -\sin k\Delta/2 \\ \cos k\Delta/2 \end{array} \right\} \quad (\text{Eq. 60})$$

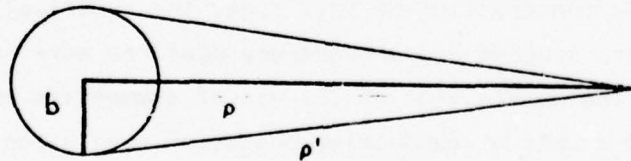
$$\begin{aligned} E_\rho(\rho', z') = & \frac{I_0}{\lambda} \left( -j \frac{n}{2} \right) \frac{1}{k\rho'} \left[ (kz' - k\Delta/2) \frac{e^{-jkr_2}}{kr_2} \left\{ \begin{array}{c} \cos k\Delta/2 \\ -\sin k\Delta/2 \end{array} \right\} \right. \\ & - (kz' + k\Delta/2) \frac{e^{-jkr_1}}{kr_1} \left\{ \begin{array}{c} \cos k\Delta/2 \\ \sin k\Delta/2 \end{array} \right\} + \frac{e^{-jkr_2}}{kr_2} \left\{ \begin{array}{c} \sin k\Delta/2 \\ \cos k\Delta/2 \end{array} \right\} \\ & - (kz' - k\Delta/2)^2 \left( j + \frac{1}{kr_2} \right) \frac{e^{-jkr_2}}{(kr_2)^2} \left\{ \begin{array}{c} \sin k\Delta/2 \\ \cos k\Delta/2 \end{array} \right\} \\ & \left. - \frac{e^{-jkr_1}}{kr_1} \left\{ \begin{array}{c} -\sin k\Delta/2 \\ \cos k\Delta/2 \end{array} \right\} + (kz' + k\Delta/2)^2 \left( j + \frac{1}{kr_1} \right) \frac{e^{-jkr_1}}{(kr_1)^2} \right. \\ & \left. \cdot \left\{ \begin{array}{c} -\sin k\Delta/2 \\ \cos k\Delta/2 \end{array} \right\} \right] \quad (\text{Eq. 61}) \end{aligned}$$

The expression for the field of a constant current distribution involves an integral of  $\exp(-jkr)/r$  which must be evaluated numerically. The field components for a current  $I_0$  are

$$\begin{aligned} E_\rho(\rho', z') = & \frac{I_0}{\lambda} \left( -j \frac{n}{2} \right) (k\rho') \left[ \left( j + \frac{1}{kr_2} \right) \frac{e^{-jkr_2}}{(kr_2)^2} \right. \\ & \left. - \left( j + \frac{1}{kr_1} \right) \frac{e^{-jkr_1}}{(kr_1)^2} \right] \quad (\text{Eq. 62}) \end{aligned}$$

$$E_z(\rho', z') = \frac{I_0}{\lambda} \left( -j \frac{\eta}{2} \right) \left[ \int_{-\Delta/2}^{\Delta/2} \frac{e^{-jkr}}{r} dz + \left( j + \frac{1}{kr_2} \right) (kz' - k\Delta/2) \cdot \frac{e^{-jkr_2}}{(kr_2)^2} - \left( j + \frac{1}{kr_1} \right) (kz' + k\Delta/2) \frac{e^{-jkr_1}}{(kr_1)^2} \right] \quad (\text{Eq. 63})$$

These expressions are separated into real and imaginary parts for evaluation in the program. The coordinate  $\rho'$  for a wire segment is taken as the distance from the observation point to a point on the side of the segment as shown below.



Also, the components  $E_\rho$  are multiplied by  $\rho/\rho'$  to account for the change in vector direction.

Ground image contributions are taken into account in the same manner as for the far field computation.

## C. BANDED MATRIX ITERATION THEORY AND DEVELOPMENT SUMMARY

### 1. Introduction

This section is a summary of the theory and development of the BMI (Banded Matrix Iteration) solution technique for the linear simultaneous equations arising from the thin-wire method of moments formalism. Standard methods of computer solution are too expensive for application to large problems. The BMI technique was developed to reduce this cost. It was chosen from a variety of possible new alternative methods after a review of the literature (reference 1). The first application was for single straight wires, either antennas or scatterers, up to 10 wavelengths long (reference 1). Success in this application motivated a study of multiple wire configurations and a test of application motivated to wire grid problems (reference 2). Initially, studies were restricted to problems involving 100 unknowns or less for economic reasons; exact solutions computed by standard methods were compared to the iterative solutions. The relative efficiency of the BMI technique was sufficiently high to justify construction of a computer code for performing the out-of-core storage manipulations required in the solution of large problems. During construction of this code, the numerical properties of the technique were studied and convergence measures were investigated (reference 3). The combination of the use of symmetries and the BMI study, wire grid models of conducting bodies of revolution were investigated. Model parameters were varied, and computed results were compared to exact theoretical results. Consistently good agreement was obtained, and the resulting model criteria were used in calculations for models of objects of varied shape and size. Problems with up to 1000 unknowns were studied (reference 5). One summary paper was published following the study of single wires (reference 6), another was published following the study of multiple wires (reference 7) and a third was published after large problems were studied (reference 8).

In parallel with these studies, a GEMACS computer code was undergoing initial development. The long term goal is to incorporate a

wide range of methods for solving electromagnetics problems in a single user-oriented package.

## 2. Theory

The method of moments is a formalism for reducing an integral equation to a set of linear simultaneous equations

$$AX = b, \quad (\text{Eq. 64})$$

where  $A$  is the complex  $N \times N$  impedance matrix,  $X$  is the column vector of complex coefficients in the current expansion, and  $b$  is the complex excitation column vector. A variety of choices for the integral equation, expansion functions, and weighting functions are in use. It is assumed that the combination chosen leads to an unsymmetric matrix  $A$ .

If  $N$  is sufficiently small, equation 64 can be solved without using peripheral device storage. Comparative efficiencies of different solution algorithms can then be predicted from the required number of complex mo's (multiplicative operations). If  $N$  is large, other factors must be considered in determining relative efficiencies. These are discussed in subsection 7.

The most efficient general method for solving linear simultaneous equations is to decompose the matrix into a product of lower and upper triangular matrices using Gaussian elimination (reference 9). This requires approximately  $N^3/3$  mo's. Solution in fewer operations requires some special feature of the equations

For thin-wire moments problems of sufficient size, such a special feature is available. The matrix elements correspond to interactions between wire segments. The interactions decrease with increasing distance between the segments. As detailed in subsection C.5, the segments



can be numbered such that the difference between segment numbers for all close-neighboring segment pairs is small compared to  $N$ . The largest matrix elements can then be kept close to the principal diagonal of  $A$ . The matrix is separated into

$$A = L + B + U, \quad (\text{Eq. 65})$$

where  $B$  is a banded matrix with upper and lower bandwidths  $M$  (numbers of minor diagonals),  $L$  is the triangular portion of  $A$  below  $B$ , and  $U$  is the triangular portion of  $A$  above  $B$ . Equation 64 can be written as

$$BX = b - (L+U)X \quad (\text{Eq. 66})$$

An iterative scheme is then

$$BX_{j+1} = b - (L+U)X_j \quad (\text{Eq. 67})$$

where  $X_j$  denotes an approximation to the solution at the  $j^{\text{th}}$  iteration, and  $X_{j+1}$  denotes an approximation to the solution at the next iteration. Some starting value  $X_0$  is chosen, and  $X_1$  is computed from equation 67. Then  $X_1$  is entered on the right-hand side, and  $X_2$  is computed. If the sequence converges, an approximate solution of equation 64 is obtained.

Equation 67 must be solved at each iteration. The cost is minimized by decomposing  $B$  into a product of lower and upper triangular banded matrices,  $B_L$  and  $B_U$ . Equation 67 is then solved by forward elimination in

$$B_L Z_j = b - (L+U)X_j \quad (\text{Eq. 68})$$

followed by back substitution in

$$B_U X_{j+1} = Z_j \quad (\text{Eq. 69})$$

Decomposition of  $B$  is similar to full matrix decomposition, except that the cost can be much less. The cost depends on the pivoting strategy used. Full pivoting destroys bandedness, and  $B_L$  and  $B_U$  would not be banded. Partial pivoting doubles the bandwidth of either  $B_L$  or  $B_U$ . Pivoting on the principal diagonal elements of  $B$  retains the bandwidth of  $M$  for both  $B_L$  and  $B_U$ . The latter is the least expensive in terms of mo's, requiring about  $NM^2 - 2M^3/3$ . Pivoting on the diagonal elements increases the risk of large errors due to accumulating rounding errors during decomposition. This subject is discussed in subsection C.4.

Assuming that  $B$  is decomposed by pivoting on the principal diagonal elements, equation 67 can be solved at a cost of about  $N^2$  mo's for each iteration. Assuming that  $K$  iterations are required for convergence, the total cost for the iterative solution process is  $NM^2 - 2M^3/3 + KN^2$  mo's. Based on the number of mo's required, the efficiency  $g$  of the banded matrix iterative method relative to the best general method is

$$g = N^3 [3(NM^2 - 2M^3/3 + KN^2)]^{-1} \quad (\text{Eq. 70})$$

This quantity is discussed in subsection C.6.

Theoretically, convergence of the sequence is assured if the spectral radius (magnitude of the largest eigenvalue) of  $B^{-1}(L+U)$  is less than one. If the spectral radius is greater than one, the sequence must eventually diverge. If it is only slightly greater than one, the sequence may initially converge and then diverge. This behavior is called pseudoconvergence. It has been observed in this research (reference 5). The best approximate solution obtained during pseudoconvergence may be sufficiently accurate for some purposes, depending on the quantity of interest and the percent error.

For the iterative method to be efficient, a reasonable convergence rate is necessary. If the choice of M and the segment numbering scheme results in such a rate, it might be expected that the solution of

$$BX_1 = b \quad (\text{Eq. 71})$$

would yield a reasonable approximation to the exact solution  $X_e$ . This is verified in practice. As a consequence, the zero vector can be used for  $X_0$ , and the multiplication  $(L+U)X_0$  need not be performed. The cost of obtaining  $X_1$  is then less than  $N^2$  (assuming B has been decomposed). If  $M \ll N$ , most of the cost of one iteration is saved. This is significant only for small problems. The important point is that if the convergence rate is high enough for efficient solution,  $X_1$  is a reasonable approximation to  $X_e$  if the zero vector is used for  $X_0$ . Hence, no physical arguments or expensive calculations for obtaining a starting value are required.

### 3. Convergence Measures

The iterative solution process is terminated by a numerical CC (convergence criterion) on some convergence measure. In the early studies of small problems (references 1 and 2) the measure used was the RE (relative error),

$$RE_j = [(X_j - X_e)^\dagger (X_j - X_e) / X_e^\dagger X_e]^{1/2}, \quad (\text{Eq. 72})$$

where  $(\dagger)$  denotes the complex conjugate transpose. The exact solution  $X_e$  was obtained by full matrix decomposition using Gaussian elimination. The computer CP (central processor) times for example problems were recorded both for the exact solution process and for the BMI process. Efficiencies computed from CP times and from numbers of mo's (equation 70) were similar, verifying that the number of mo's is an adequate measure of efficiency for solution processes if no out-of-core manipulations are required.

Due to the cost of computing  $X_e$  for large problems, the RE was available as a convergence measure only during the research phase on small problems. An alternative measure called the BCRE (boundary condition relative error)

$$\text{BCRE}_j = [(AX_j - b)^{\dagger}(AX_j - b)/b^{\dagger}b]^{1/2} \quad (\text{Eq. 73})$$

was proposed (reference 1). A study of the relationship between the BCRE and the RE for a variety of small problems showed that the BCRE is not always a reliable measure of convergence (reference 2). This lack of reliability can be traced to the stability of the equations for a given problem (reference 3). This subject is discussed in subsection C.4.

An alternative measure of convergence is available (reference 3). The IRE (iterative relative error) is defined by

$$\text{IRE}_j = [(X_j - X_{j-1})^{\dagger}(X_j - X_{j-1})/X_j^{\dagger}X_j]^{1/2}. \quad (\text{Eq. 74})$$

The IRE is a measure of the relative change in the sequence of approximate solutions from one iteration to the next. It is an adequate measure of convergence.

The sequence of values of the RE or the IRE has been found to be approximated by a simple exponential function (reference 3). As a result, the IRE can be approximately predicted at any iteration from the values at the previous two iterations;

$$\begin{array}{ll} \textcircled{1} \text{ IRE}_j = P e^{-Q \cdot j} & \textcircled{4} P = \text{IRE}_j (\text{IRE}_{j-1} / \text{IRE}_j)^j \\ \textcircled{2} \text{ IRE}_{j-1} = P e^{-Q \cdot (j-1)} & \textcircled{5} \text{ IRE}_{j+1} = P e^{-Q \cdot (j+1)} \\ \textcircled{3} Q = \ln(\text{IRE}_{j-1} / \text{IRE}_j) & \textcircled{6} \text{ IRE}_{j+1} \approx (\text{IRE}_j)^2 / \text{IRE}_{j-1} \end{array}$$

(Eq. 75)



The smallness criterion for convergence can then be placed either on the IRE or on the predicted IRE at the next iteration.

Statistics gathered for small problems showed that the predicted value of the IRE is also a good prediction of the RE, at least for cases of rapid convergence (reference 3). This leads to a definition of the PRE (predicted relative error)

$$PRE_j = (IRE_j)^2 / IRE_{j-1}. \quad (Eq. 76)$$

The PRE (Equation 75, number 6) is an adequate measure of convergence.

The flexibility of the GEMACS code allows the user to specify his own convergence measure. Any quantity that is readily (inexpensively) computed can be used. Since some quantities such as the BCRE may not be adequate due to instability of the equations, new measures should be used with caution.

#### 4. Stability

The subjects in this section have been investigated in great detail in the last two decades. The purpose of this section is to introduce, in a nonrigorous manner, those definitions and concepts which were useful in this research. The material and notation closely follow reference 9. Most quantities in this report are complex, whereas those in reference 9 are real.

The euclidean length or norm of a vector  $X$  in complex  $N$ -dimensional space is defined as

$$||X|| = (X^\dagger X)^{1/2} \quad (Eq. 77)$$

Other vector norms exist, but will not be used here. The norm of a complex matrix  $A$  with  $N$  rows and  $N$  columns is defined as

$$||A|| = \max_{X \neq \theta} \frac{||AX||}{||X||} \quad (\text{Eq. 78})$$

where  $\theta$  denotes the zero vector. An alternative definition is

$$||A|| = \max ||AX||, ||X||=1 \quad (\text{Eq. 79})$$

This can be interpreted to mean that if the unit sphere in the space of  $X$  is mapped by  $AX$  into the space of  $b$ ,  $||A||$  is the longest vector that will be obtained.

Similarly, the norm of the inverse of  $A$  can be defined by

$$||A^{-1}|| = \max_{b \neq \theta} \frac{||A^{-1}b||}{||b||} \quad (\text{Eq. 80})$$

or by

$$||A^{-1}|| = \max ||A^{-1}b||, ||b||=1 \quad (\text{Eq. 81})$$

Thus, if the unit sphere in the space of  $b$  is mapped into the space of  $X$  by  $A^{-1}b$ ,  $||A^{-1}||$  is the longest vector that will be obtained.

The condition number of  $A$ , denoted by  $\text{cond}(A)$ , is defined as

$$\text{cond}(A) = ||A|| \cdot ||A^{-1}|| \quad (\text{Eq. 82})$$

This number is not easily computed. It is conceptually valuable in a variety of ways. If the vector  $b$  is subject to the uncertainty  $\delta b$ , the uncertainty  $\delta X$  in  $X$  is bounded by

$$\frac{||\delta X||}{||X||} \leq \text{cond}(A) \cdot \frac{||\delta b||}{||b||} \quad (\text{Eq. 83})$$

The relative error in the solution is then bounded by the product of the relative error in  $b$  and  $\text{cond}(A)$ . If the matrix elements in  $A$  are subject to uncertainty  $\delta A$ , a similar bound is obtained. In each case, a large value of  $\text{cond}(A)$  is a warning that the solution may be highly sensitive to small changes in  $A$  or  $b$ .

Another useful bound involves the ratio of the RE to the relative residual, which is the BCRE used in this work:

$$\frac{1}{\text{cond}(A)} \leq \frac{\text{RE}}{\text{BCRE}} \leq \text{cond}(A). \quad (\text{Eq. 84})$$

Since  $\text{cond}(A) \geq 1$ , this ratio can be very small or very large. For a variety of thin-wire moments problems, this ratio was found (reference 2) to be between 1 and 10, with an average of about 3. It is obvious that a much wider range of values is possible. If  $\text{cond}(A)$  is large, A is said to be ill-conditioned. One consequence of ill-conditioned matrices is that the BCRE may be quite small when the RE is large. The BCRE may then be an adequate measure of convergence in the banded matrix iteration method only if  $\text{cond}(A)$  is near unity.

A measure of stability that has been used in the method of moments (reference 10) and that has properties similar to those of the condition number, is the pivot ratio. This quantity is easily calculated during decomposition by Gaussian elimination. It can be defined as the ratio of the magnitudes of the first and last pivot elements (reference 10), or as the ratio of the largest to the smallest of the magnitudes of the pivot elements. Only the order of magnitude of the pivot ratio is significant. The choice of definitions is not important when compared to the effect of the choice of pivoting strategies. While pivoting on the largest element of a row or column will reduce the cumulative effect of rounding errors, it also reduces the pivot ratio. Hence, pivoting on the diagonal elements should produce a larger pivot ratio for ill-conditioned matrices.

In the banded matrix iterative scheme, the banded matrix is decomposed using Gaussian elimination. The decomposition is accomplished by pivoting on the diagonal elements. (Pivoting on other elements would increase the bandwidth and result in loss of efficiency.) The pivot ratio for the banded matrix is then available as a measure of ill-conditioning of B. Unfortunately, no method has been found to relate either the pivot ratio to  $\text{cond}(B)$  or  $\text{cond}(A)$  to  $\text{cond}(B)$ . It is possible

that either A or B could be ill-conditioned while the other is not. This would probably depend on the physical problem, the choice of segment numbering schemes, and the choice of bandwidths. Certainly  $\text{cond}(B)$  should approach  $\text{cond}(A)$  as M approaches N.

#### 5. Segment Numbering

Two types of segment numbering problems occur. For the iterative scheme to be efficient, the segments must be numbered so as to keep the large matrix elements in the band. The best choice of numbering for this purpose is obvious in some cases and not in others. More than one choice may be apparent. The same logical process can be used to number segments for a variety of problems, as will be shown. The other problem in numbering is related to the requirements for input data for the geometry processor in any moments code. Generally speaking, the code automatically numbers segments in sequence along each wire, in the order in which wire data are entered. For the iterative method, this numbering is adequate in some cases and not in others. If some other numbering is necessary, the obvious method is to enter the wire data in the order desired. For most codes, this could require a tedious process of entering each segment as a single wire and supplying connection data. An easier way will be shown that involves segment renumbering.

##### a. Numbering for the Iterative Method

The logic for the numbering scheme that is adequate for many problems is most easily explained for flat objects (all wires in a plane). The basic idea is to superimpose a set of narrow parallel strips on the object of interest. Figure 3 shows the strips as separated by dashed lines, with a lumpy appearing object in outline. Assuming that the object is a wire loop, numbering is as shown in the figure. Starting at one extremity, numbering proceeds from left to right until all segments in the first strip are numbered. Moving to the next strip, numbering again proceeds from left to right. This continues until all segments are numbered. In the figure, it is assumed that the segment end occurs at intersections with the dashed lines. This need not be the case. Strip widths can also vary. This depends on the geometry of the object.



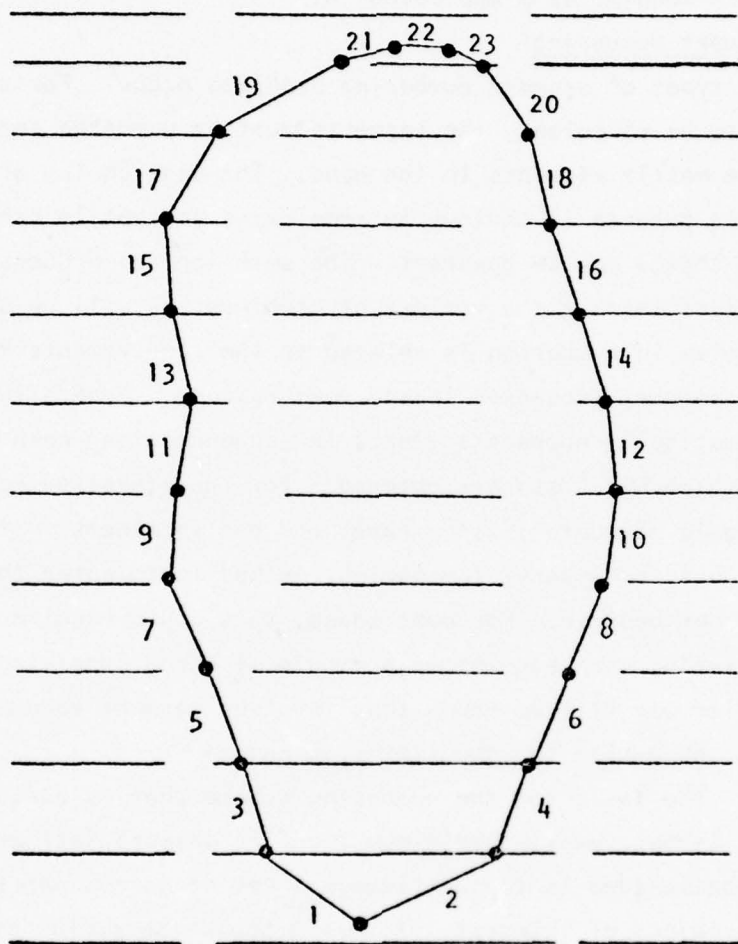


Figure 3. Parallel Strips Superimposed on a Wire Loop

Section E of reference 2 includes a discussion of this numbering scheme as it applies to example problems. Generally, any flat object should be oriented so that the strips run across the narrow dimension of the object. This keeps the number difference between segments in adjacent strips as small as possible.

The strip numbering scheme has a direct application for some three-dimensional objects. The simplest is a cylindrical grid. Numbering a rectangular grid by the strip method and rolling the grid into a cylinder (about the correct axis) results in a helix-like numbering scheme. This is appropriate when the cylinder length is greater than or roughly equal to its circumference. If the cylinder has end caps, numbering should proceed from one end cap center to the other. The pattern is then spiral, helical, and spiral. However, if the cylinder is short compared to its circumference, the spiral scheme may not give an efficiency as high as that obtained by orienting the cylinder axis normal to the plane of the strips.

A sphere or cube can be handled much the same as the cylinder with end caps. For elongated shapes, numbering should start at one extremity.

A similar method for segment numbering that can be automated is discussed in reference 4. It is called geometric cell division. Figure 4 shows a set of parallel strips normal to a direction vector  $d$ . For planar objects, it was noted that the set of strips could be superimposed on the wire object; segment numbering would proceed along each strip starting at one extremity of the object. For an irregular object, the choice of direction for  $d$  is not obvious.

Figure 5 shows an irregular planar object with four possible directions for  $d$ . If the small appendages were absent,  $d_1$  would be the obvious choice. Numbering would then be in strips across the narrow dimension of the large rectangle. With the appendages present, directions  $d_1$  and  $d_3$  are not advisable. In some strips, numbering would proceed across the large rectangle and along the length of one projection before advancing to the next strip. This can be alleviated somewhat

by using direction  $d_2$ , so that no strip runs through the length of the longer projection. The other choice is  $d_4$ , and it is clearly the best. No strip runs both across the large rectangle and along a projection, and the strips that cut through both projections include few wire segments.

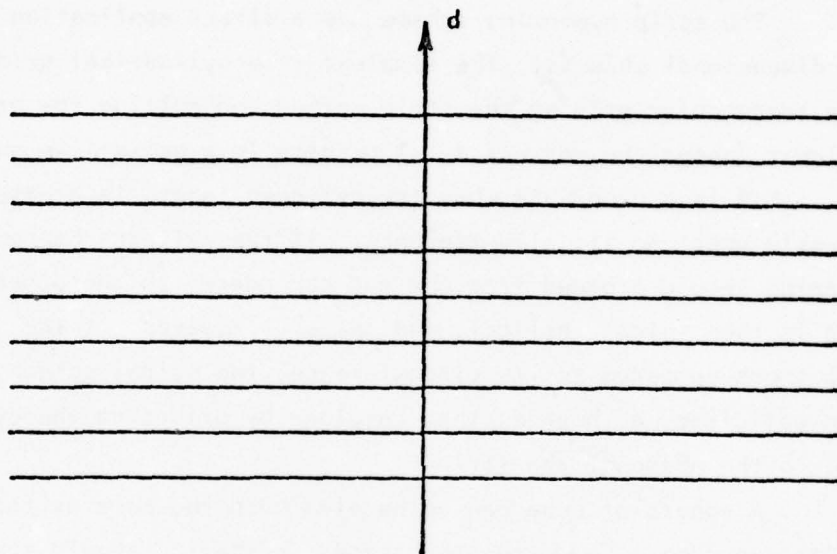


Figure 4. A Set of Parallel Strips Normal to a Direction Vector  $d$

After studying several examples of this sort, a consistent result emerges. The best choice of orientation apparently lies along (or at some small angle to) a principal inertial axis of equal point masses located at the wire segment centers. The best principal axis is always the one about which the moment of inertia is least. This scheme will be called the PASS (Principal Axis Slicing System). No proof has been found that this orientation for slicing is the best choice, and its practicality would have to be exhibited in practice. The method can be extended to three dimensions as follows. Let the principal axis coordinates be denoted  $X, Y, Z$ , with the least inertia about the  $X$ -axis

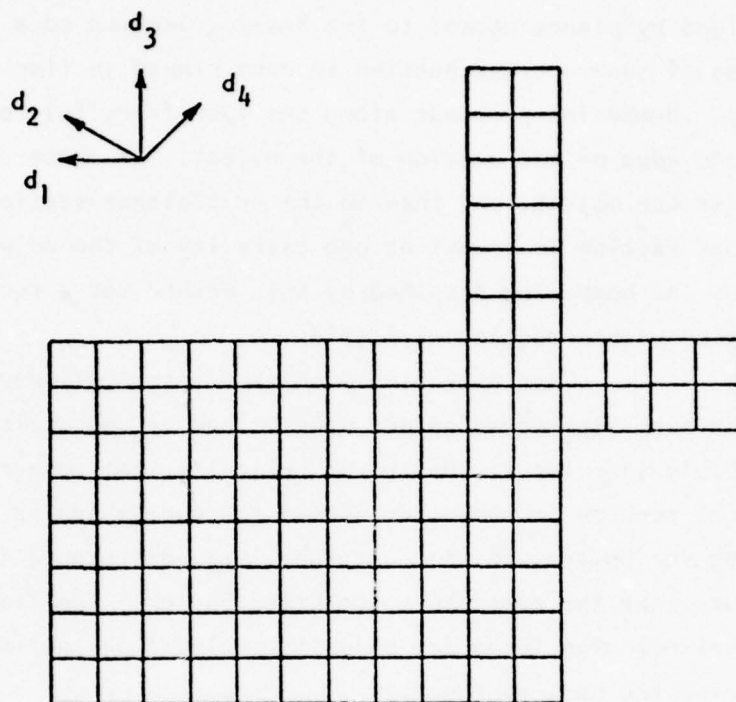


Figure 5. An Object of Irregular Shape with Various Possible Direction Vectors



and the greatest about the Z-axis. Divide the object by a set of planes normal to the X-axis, with the separation of the planes somewhat less than the wire segment lengths. The space between adjacent planes is divided by planes normal to the Y-axis, leading to a set of parallel tubes of square cross section in each planar section normal to the X-axis. Numbering proceeds along one tube (parallel to the Z-axis) starting at one edge of the section of the object. It proceeds from tube to tube across the object, and then to the next planar section. The first planar section is always at one extremity of the object. Figure 6 shows the numbering obtained by this method for a rectangular object modeled with a regular wire grid.

For a problem such as a large cylinder with end caps or other such flat-ended object, the method of geometric cell division is probably inferior to the spiral-helical-spiral numbering method. The former results in numbering across the end in strips before proceeding along the object, so that a rather large difference in segment numbers occurs near the edge where numbering begins. The limited practical experience with large fat objects precludes any definite statement concerning the best approach.

b. Segment Renumbering

As mentioned earlier, the geometry processing portions of most programs provide segment numbering that is sequential along each wire in the order in which wire data are entered. This segment numbering is adequate for the banded matrix method for some problems. If it is not, it can still be used initially to simplify the model input data. The segments can then be renumbered in any sequence desired. Details and examples of the renumbering process as it was used in the research phase are contained in Section E of reference 2. The GEMACS code permits the user to number the segments in any order desired.

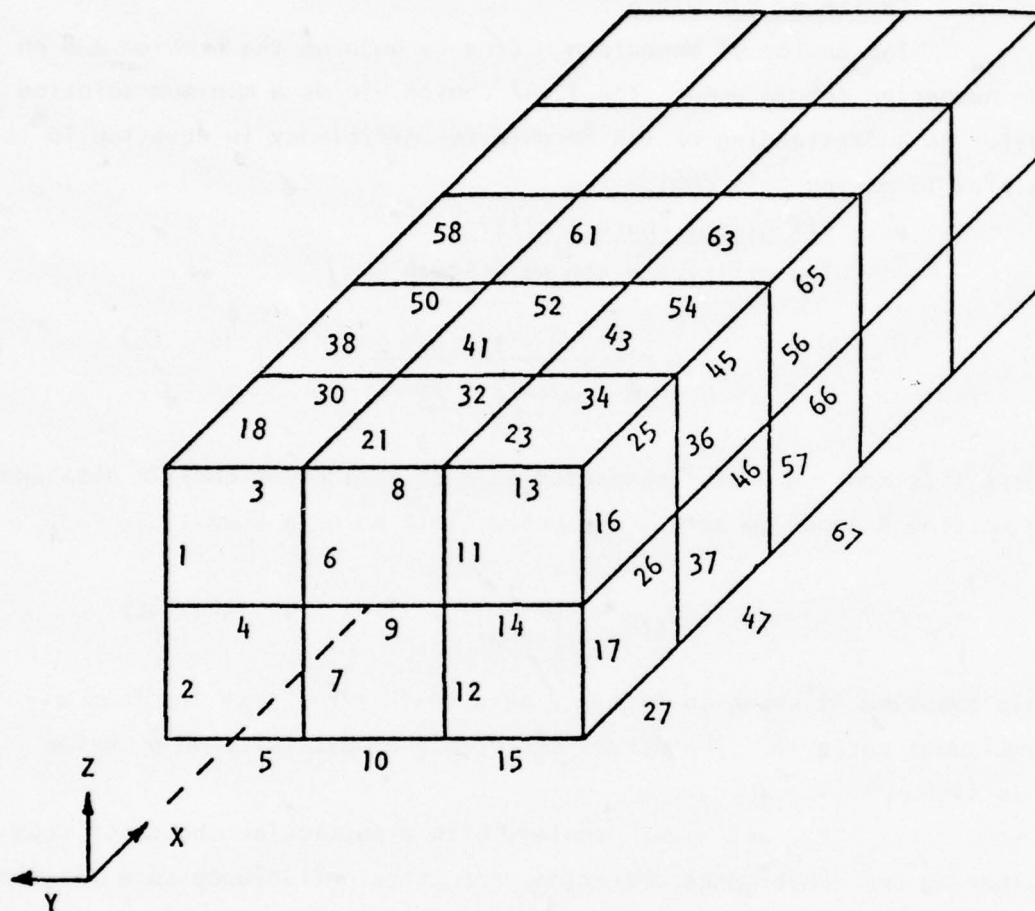


Figure 6. Part of the Segment Numbering Obtained with the Principal Axis Slicing System for a Rectangular Parallelepiped

## 6. Choice of Bandwidth

The choice of bandwidth  $M$  depends both on the problem and on the numbering scheme used. The ideal choice yields a minimum solution cost. An understanding of the formula for efficiency in equation 70 is helpful in making this choice.

### a. Efficiency Characteristics

The efficiency can be written

$$g = \frac{1}{f^2(3-2f) + 3K/N}, \quad (\text{Eq. 85})$$

where  $f$  is  $M/N$ . A useful characteristic of this efficiency is obtained by setting  $K$  equal to zero. The upper limit on  $g$  is then

$$g_{\text{LIM}} = \frac{1}{f^2(3-2f)}, \quad (\text{Eq. 86})$$

This function is shown in figure 7 as a solid line, treating  $f$  as a continuous variable. The actual efficiency always falls on or below this line.

For any given problem, with a particular choice of segment numbering and convergence criterion, the actual efficiency as a function of the bandwidth is as follows. At  $M$  equal to  $N$ , the solution  $X_1$  will always satisfy the CC (convergence criterion). (When the relative error is not available as a convergence measure, at least one iteration is necessary to test for convergence. If  $N$  is large, one iteration is of little cost, and will be ignored in this discussion.) As  $M$  is decreased, the error in  $X_1$  gradually increases. Experience shows that this error may not increase monotonically, but may have minor oscillations superimposed (reference 1). Eventually, a bandwidth in the breaking region is reached. This region is a narrow range in bandwidth where the error in  $X_1$  is just above or just below the CC. A breaking point can be defined as the largest bandwidth at which the error in  $X_1$  is greater than the CC. At this bandwidth, at least one iteration is required to reduce the error to the CC. In most cases, the actual efficiency will then depart from

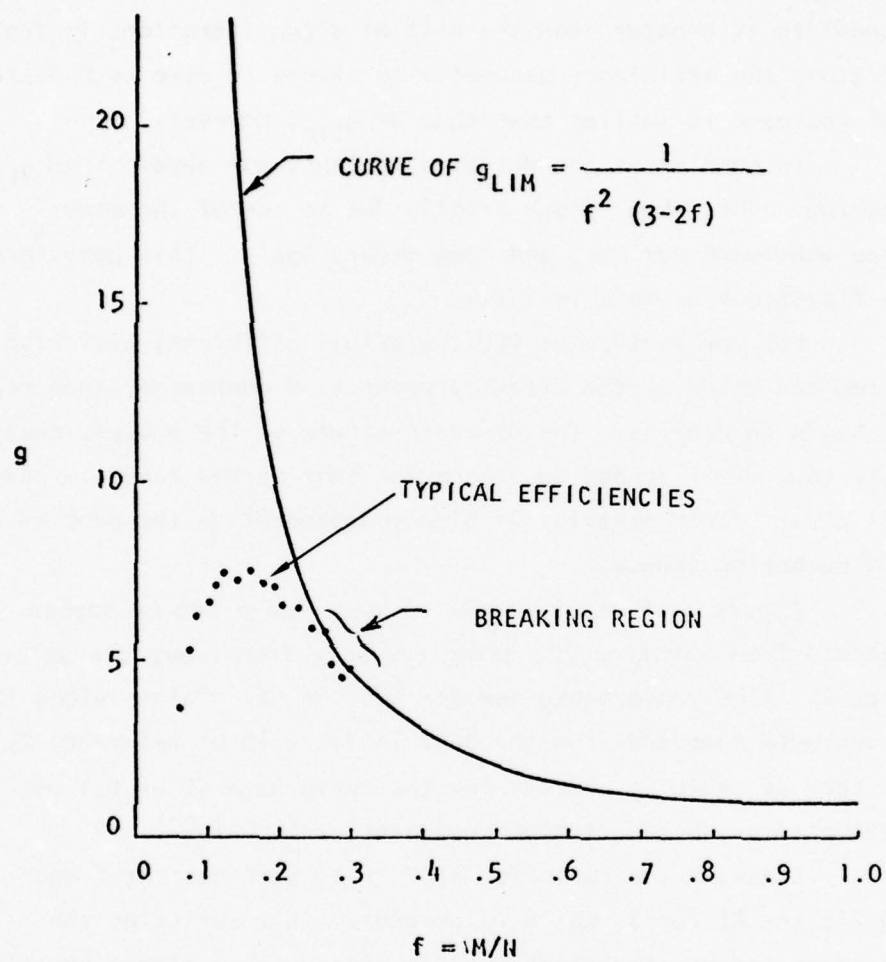


Figure 7. The Curve of  $g_{LIM}$  Versus  $f$  and a Fictitious Example of Actual Efficiencies



the  $g_{LIM}$  curve. Because the savings in cost of decomposing B at a smaller bandwidth is greater than the cost of a few iterations in the breaking region, the efficiency generally continues to rise as M decreases. The rate of increase is smaller than that of  $g_{LIM}$ , however.

In some cases the actual efficiency can depart from  $g_{LIM}$  at the breaking point, then return briefly due to one of the minor oscillations mentioned earlier, and then depart again. This behavior was shown by a fictitious example in figure 7.

For any particular CC, the actual efficiency will rise somewhat from the value at the breaking point as M decreases, then reach a peak and begin to decline. The discrete nature of the process necessarily means that minor up and down behavior over narrow ranges of bandwidths will occur. This behavior is highly dependent on the problem and the segment numbering scheme.

Figure 8 shows the curve of  $g_{LIM}$  and a set of dashed curves obtained from equation 70, using the data from example problem 9 in reference 2. (The convergence measure was the RE. Points along the dashed curves were computed from the data in Table 45 of reference 2, reproduced here as table 1. Points for the curve at a CC of 0.1 percent were approximated using the extended exponential function.)

Consider the curve for a CC of 10 percent. At f equal to 17/80 or 0.21, the RE for  $X_1$  was 6.13 percent. This satisfies the CC of 10 percent, so no iterations were required. Then either equation 70 or equation 86 yields an efficiency of 8.7. This is the highest efficiency that can be obtained for this problem at a bandwidth of 17; relaxing the CC will not affect the efficiency. Tightening it to something less than 6.13 percent will result in at least one iteration being performed, with a loss in efficiency.

The location of the peak of the efficiency curve clearly shifts toward smaller bandwidths as the CC is relaxed. The width of the curve near the peak narrows as the CC is relaxed. The rate of decrease in efficiency is less to the right of the peaks.

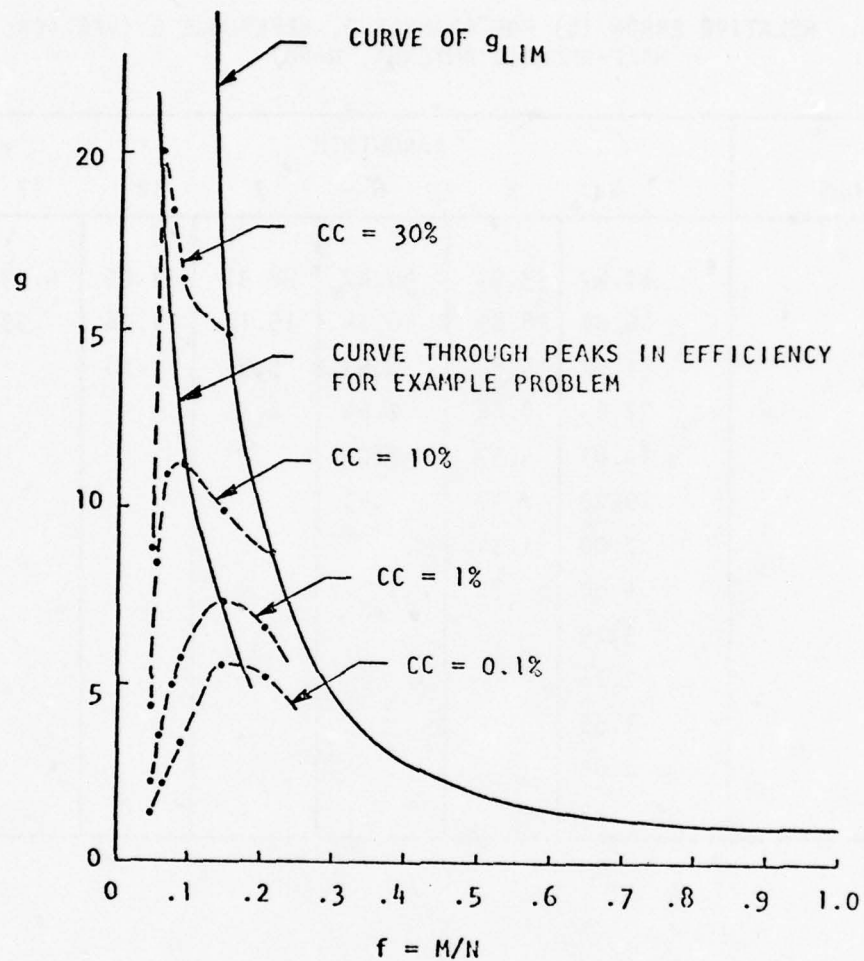


Figure 8. Efficiency Versus  $f$  for an Example Problem. Curve Labels are the Convergence Criteria on the Relative Error

TABLE 1. RELATIVE ERROR (%) FOR EXAMPLE 9, REFERENCE 2 (VERTICAL  
HALF-RHOMBIC ANTENNA, N=80)

ITERATIONS	BANDWIDTH					
	4	5	6	7	12	17
1	67.67	53.91	40.47	38.91	11.05	6.13
2	46.09	28.89	16.14	15.12	1.36	.59
3	31.62	15.64	6.53	5.94	.18	
4	21.69	8.46	2.64	2.33		
5	14.87	4.57	1.06	.91		
6	10.20	2.47	.43			
7	7.00	1.34				
8	4.80	.72				
9	3.29					
10	2.26					
11	1.55					
12	1.06					
13	.73					

If the program user imposes a tight CC (about 1 percent or smaller for small problems), he can afford to pick  $M$  such that he misses the peak efficiency by quite a bit to either side because the peak is wide. At larger values of the CC, he will tend to decrease  $M$  to try to stay near the peak, but he may be increasingly conservative to avoid a point too much to the left of the peak. This is good in a sense, because use of larger bandwidths provides lower initial errors and higher convergence rates, resulting in better performance of the PRE convergence measure (see subsection C.3). If the user picks a bandwidth too much to the left of the peak, slow convergence and low efficiency will occur. Restarting with a larger bandwidth might provide a higher overall efficiency even with the cost of an aborted run included.

b. Bandwidth Estimates for Long, Thin Objects

The shapes and locations of peaks of the efficiency curves vary considerably from problem to problem. No method for accurate prediction of the bandwidth for peak efficiency has been found. A survey of example small problems did yield a trend when the CC is 1 percent. It was found that the bandwidth for efficient solution could be estimated from structure dimensions with fair reliability. A bandwidth  $M$  corresponds to a distance  $R_M$  within which all interactions are to be kept in the band. (For segments of length  $0.1 \lambda$  numbered sequentially along a straight wire, a bandwidth of  $M$  corresponds to a distance of  $M \times 0.1 \lambda$ .) The distance in wavelengths for bandwidth estimation is shown in figure 9 as a function of the object length in wavelengths for objects having a dominant dimension  $L$ . The vertical bars show the uncertainty in value for several problems. The linear trend is obvious.

This trend was obtained from studies of problems with 100 unknowns or less. They were primarily problems involving long wires or wire arrays. Studies of larger problems did not include bandwidth as a parameter. The initial bandwidth was generally selected from figure 9. For planar or near-planar objects and for thin cylinders, rapid convergence was fairly consistently obtained. Fat cylinders, spheres, and objects where  $L$  is less than  $\lambda$  require larger bandwidths (reference 5).



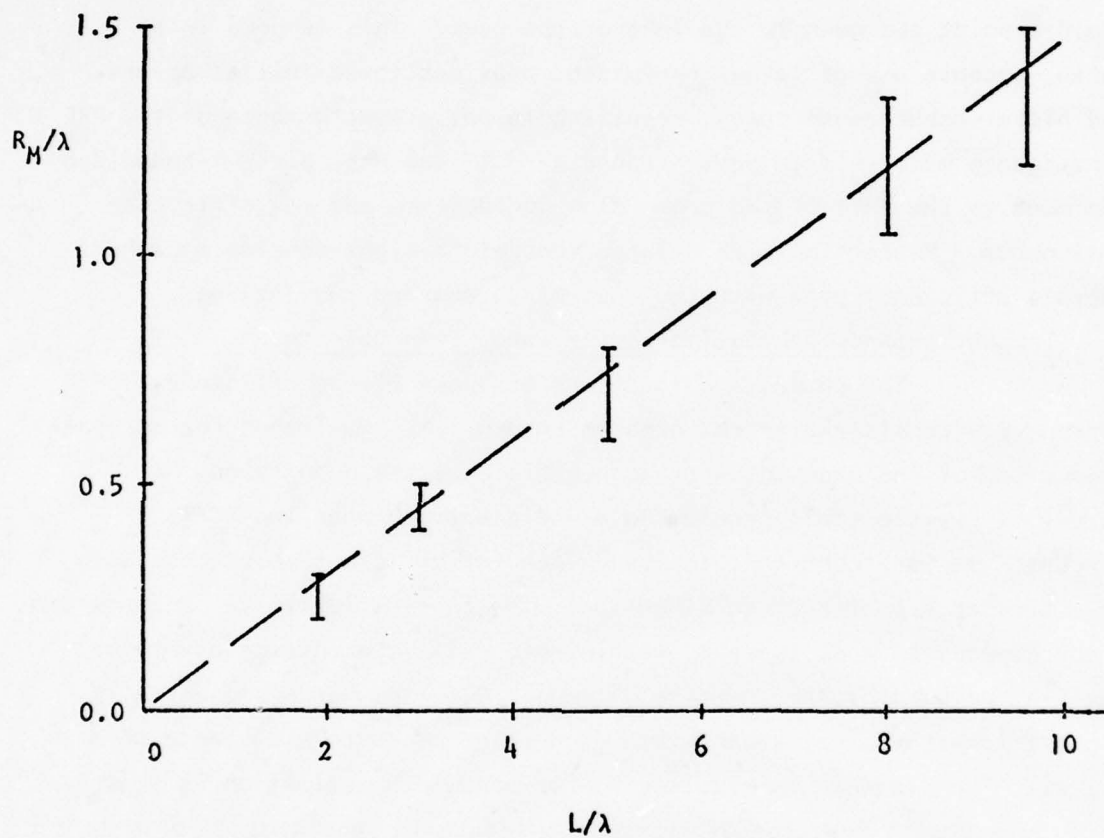


Figure 9. The Linear Trend Between the Bandwidth Estimate and the Object Length  $L$   
 ( $R_M$  = Distance Corresponding to Bandwidth)

The parameter  $L$  is usually the largest geometric dimension; however, for complex objects, the choice or value of  $L$  may depend on the excitation type and orientation (this is shown by an example in subsection D.3). Use of figure 9 for these objects may lead to pseudo-convergence for cases in which there are large (or small coherent) interactions not included in the band.

#### 7. Computer Timing Requirements

For small problems, the primary computer cost is the CP (central processor) time required to compute matrix elements. Use of the BMI solution process in the place of full matrix decomposition by Gaussian elimination is primarily of academic interest for such problems. The CP time for computing matrix elements increases as the square of  $N$  for most programs. The solution time increases as the cube of  $N$  for full matrix decomposition. For sufficiently large  $N$ , the solution time by this method will eventually dominate. The iterative process is a method for reducing the solution cost. The total cost for generating and solving large problems is sufficient to justify optimization of the code for a given computing facility.

For problems with  $N$  in the range below 1000, three primary factors contribute to the computer costs; the CP time required to compute or fill the impedance matrix, the CP time required to perform the multiplicative operations in solving the equations, and the PP (peripheral processor) time required for out-of-core manipulations. The PP time includes input/output time and considerable bookkeeping time. For large problems, the PP time is almost entirely associated with the solution process. A cost comparison of solution methods should include both CP and PP times. (The best comparison is actually based on dollar costs, but no two installations use the same cost algorithm to charge for total computer resources used.) The PP time and solution CP time are extremely dependent on the machine, the computing system, and the particular computer code being used. The solution CP time also depends on the compiler used. Consequently, the efficiency based on the number of multiplicative operations is used as a simple assessment of overall efficiency.

The CP times required for solution on the CDC 6600 computer (FTN 4.2 compiler) are shown in figure 10 versus the number of multiplicative operations required to solve example problems using the iterative method. The linear dependence over such a wide range indicates that the efficiency based on number of multiplicative operations is a valid comparison of CP costs between methods.

The PP time shows a similar linear dependence on the number of multiplicative operations, except that the PP times were higher by a factor of about 15. This proportionality factor is extremely dependent on the amount of fast access core available for matrix elements during the decomposition of B. (For a given amount of storage, the PP time for decomposition of B should be much less than that for decomposition of the full matrix using Gaussian elimination.) The amount of available core can be increased by a variety of methods including program segmentation or overlaying. These methods were not used during this investigation and only 14 columns of the matrix could be kept in core for a problem with 1000 unknowns. As a consequence, the PP costs were the highest dollar cost of the study.

The CP times required by the modified AMP code incorporating the BMI solution technique for computing matrix elements is shown in figure 11 versus the number of unknowns. The upper curve is for wire grid problems and the lower is for wire problems with no multiple wire junctions. The difference is due to a repeated search of junction connection data, and is not apparent for small problems. Most of this cost difference is eliminated in the GEMACS code by replacing the search with a circular linked list. The CP times for large problems can be further reduced by using less expensive algorithms (such as the Hertzian dipole) to compute matrix elements corresponding to interactions between segments separated by about a wavelength or more. This option was not used for the example problems. Further cost reductions may be obtained by relaxing the accuracy restrictions in computing large matrix elements. These elements should be accurate only enough to match the overall accuracy required of the modeling and solution process.

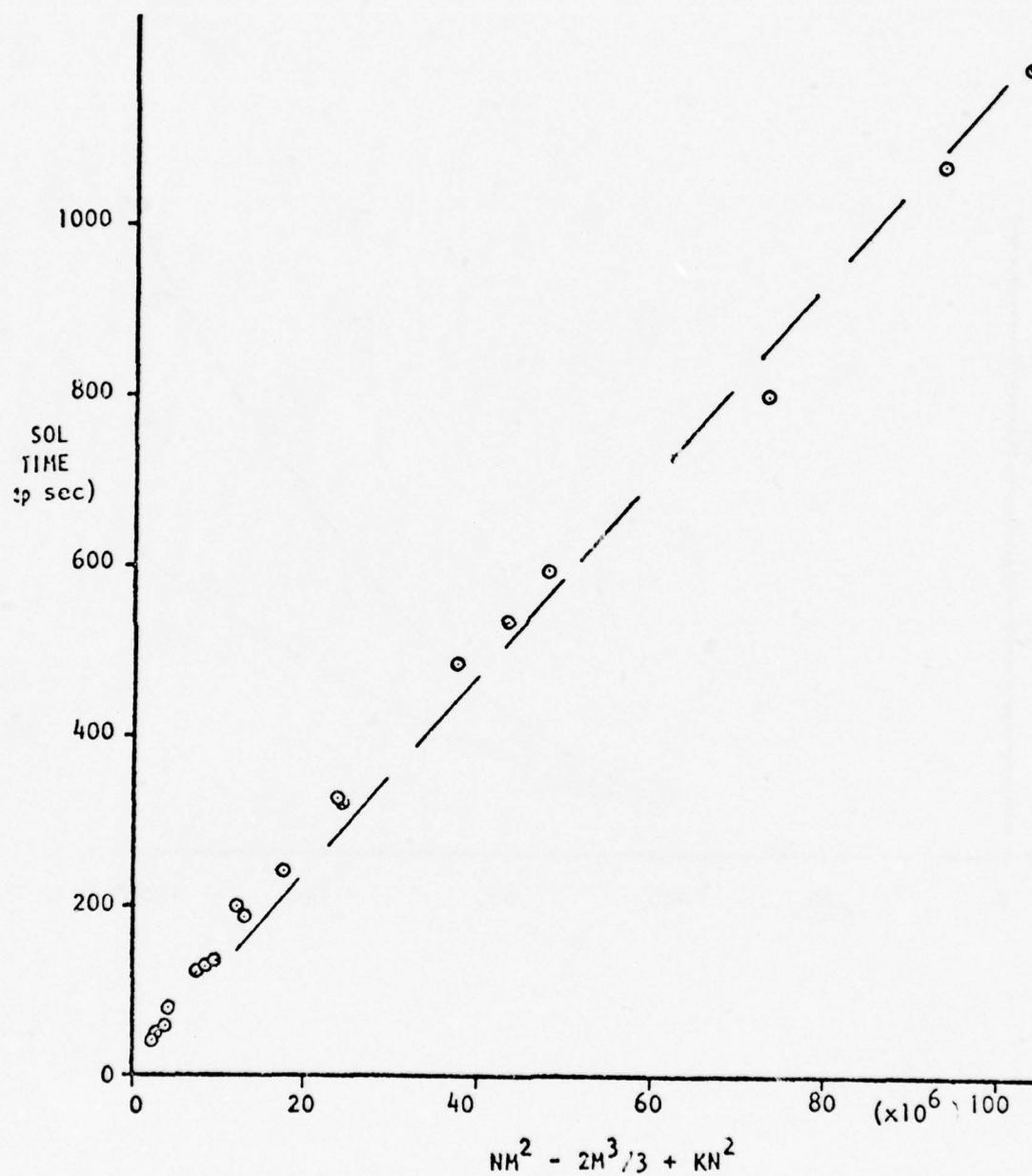


Figure 10. Equation Solution Time Versus Number of Complex Multiplicative Operations



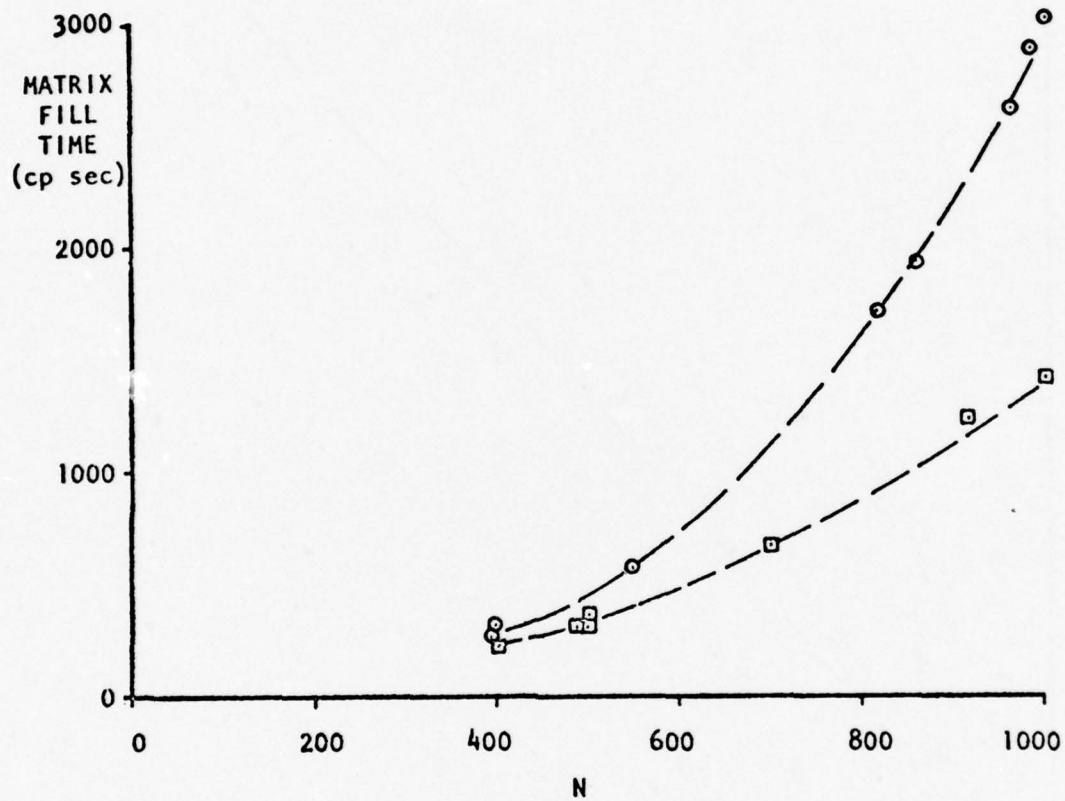


Figure 11. Matrix Fill Time Versus Number of Unknowns  
(⊙, Grid Problems; ◻, No Multiple Junctions)

#### D. SUMMARY OF RESULTS

Numerical results were obtained for a variety of thin-wire problems (references 1 through 5). Three different computer programs were used. The general results and a few examples are listed here. All calculations were performed on a CDC 6600 computer. Dimensions are in meters.

##### 1. Single Straight Wires

The first results (reference 1) were obtained using the moments formalism of Harrington (reference 11). That is, the potential integral equation was solved using pulse expansion functions and point matching (collocation) at wire segment midpoints. All examples were single straight wires, either antennas or broadside scatterers, with  $L$  (length) to  $\lambda$  (wavelength) ratios ranging from 2.5 to 10. Length to  $D$  (diameter) ratios were either 74.2 or 1000. The convergence measure was the RE, and the convergence criterion was 1 percent. There were 10 segments per wavelength used, with segment numbering sequential along the wire. It was found that:

- (1) The iterative solution converges monotonically at bandwidths from 3 to  $N$ . (With 10 segments per wavelength, a bandwidth of 3 means that interactions at distances over  $0.3\lambda$  are excluded from the band.) An example of the convergence behavior is shown in figure 12. The wire is a centerfed antenna with  $L/\lambda = 2.5$ ,  $L/D = 1000$ , and  $N = 25$ . The figure shows the RE at each iteration for a given bandwidth. Points are connected by a line for clarity; the results are necessarily discrete.
- (2) Convergence rates depend on the wire radius, as do errors in the initial solution,  $X_1$ . Thinner wires result in better efficiency.
- (3) Relative errors for  $X_1$  are larger for resonant antennas than for nonresonant antennas for the same bandwidth. The difference is greater for smaller wire radii.
- (4) The relative error for  $X_1$  does not decrease smoothly and monotonically with increasing bandwidth. Periodic variations occur at changes in bandwidth that correspond to half-wavelength changes in distance along the wires, as exemplified in figure 13.

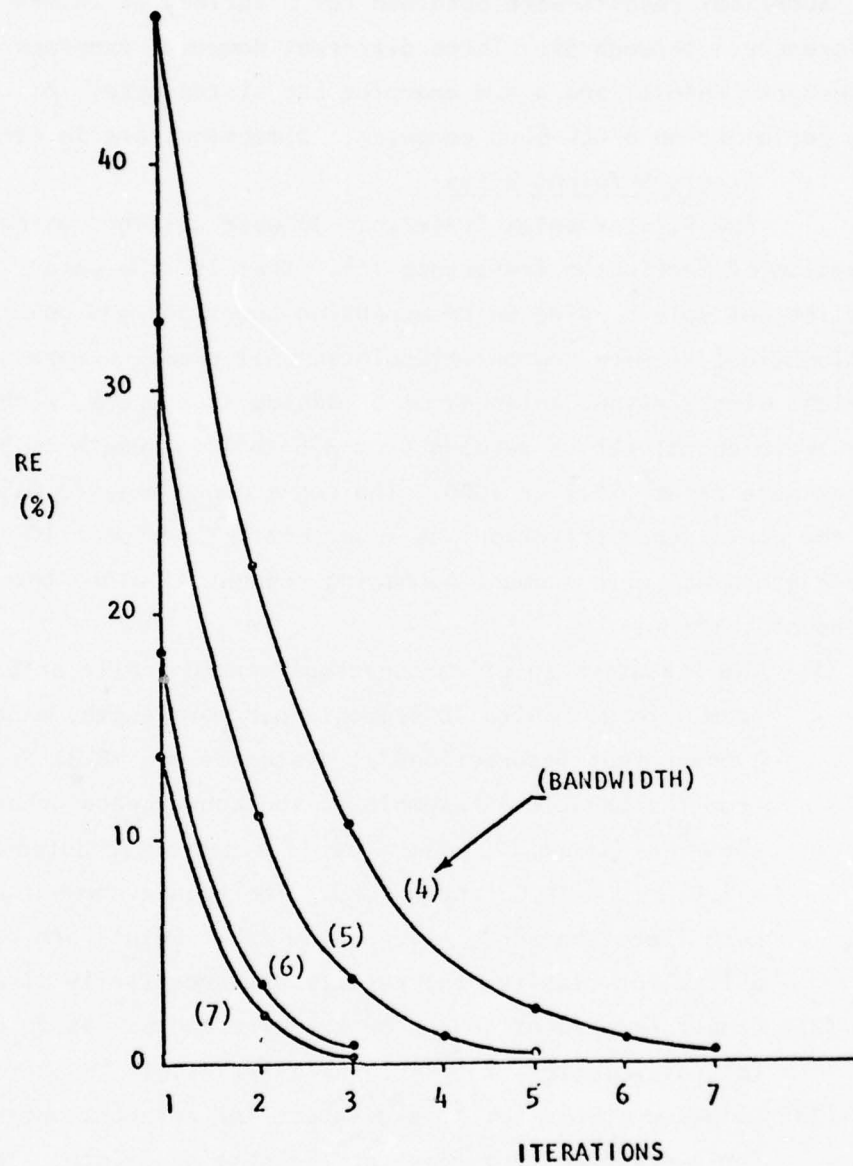


Figure 12. Relative Error Versus Number of Iterations, Example 4 of Reference 1



Figure 13. Relative Error (Percent) versus Matrix Bandwidth for First Iteration, Example 4 of Reference 1



- (5) As indicated in subsection C.3, convergence behavior for a given bandwidth can be approximated with varying accuracy by the formula  $RE(\%) \approx 100 e^{-Q \cdot i}$ , where  $i$  is the number of iterations and  $Q$  is a function that is dependent on the bandwidth. The dependence is linear in a first approximation, with an oscillation superimposed. However, the slope of the linear part is dependent on the excitation, length, and wire radius.
- (6) For a length to wavelength ratio of 10, iterative solutions with a relative error of 1 percent were obtained with an efficiency of about 7. For a relative error of 10 percent, an additional reduction in CP time up to a factor of 2 was obtained.
- (7) The bandwidth resulting in peak efficiency varies with wire length in a roughly linear fashion. At 10 segments per wavelength, the optimum bandwidth is about 4 of 5 for  $3\lambda$  wires and in the range 10-15 for  $10\lambda$  wires.

The reader is referred to reference 1 for details and to 6 and 7 for summary comments.

## 2. Multiple Straight Wires

The second set of results (reference 2) was obtained by modifying program WAMP (reference 12). That program is based on the Pocklington integral equation, with pulse plus sine plus cosine expansion functions and collocation. With  $N$  wire segments, this choice of expansion function requires  $3N$  current coefficients. Imposition of "extended continuity conditions" at adjacent segment midpoints reduces the number of unknowns to the  $N$  values of current at the segment midpoints. Point continuity in the current is not obtained at junctions. An extended continuity method is also used at multiple junctions, but the method is considered poor for wire grid problems.

Using this program for generating the equations, various combinations of thin-wire geometries were used to investigate the capabilities and limitations of the banded matrix method. These included:

- (1) One straight wire.
- (2) Two parallel centered antennas at varying separations and radii.
- (3) Two collinear centered antennas at large and small separations.
- (4) A linear array of parallel dipoles.
- (5) Square and circular arrays of parallel dipoles.
- (6) A two-dimensional array of short dipoles.
- (7) A helix antenna.
- (8) A vertical half-rhombic antenna over sea water.
- (9) A wire-gridded rectangular strip.
- (10) A square loop.
- (11) A pair of crossed wires.

In each case, N was restricted to 100 or less for economic reasons.

For many of the examples, the sequence of solutions converged uniformly to the exact solution. Divergence was forced for some examples by using a combination of element numbering, geometry, and bandwidth so that some large matrix elements were not contained in the B band. The general approach to segment numbering for the BMI solution technique was developed during this phase.

Because of the wide variety of geometries involved in these examples, the results are not in a form to be easily summarized. The convergence measure was the RE. At a convergence criterion of 1 percent, efficiencies were generally around 5 to 10 and up to 23. The iterative process was interrupted for some problems when the RE was first reduced to less than 30 percent. The far field pattern was computed from the approximate solution. The iteration was then continued to the 1 percent level, and the far field pattern was again computed. Comparison of the far fields obtained from the two current distributions indicates that a 30 percent CC may be adequate for far-field pattern determination.

Example 12 of reference 2 is reproduced here to exhibit one of the problems with automating the segment numbering scheme called PASS (see section C.5). Table 2 shows the description of the problem; a

TABLE 2. DESCRIPTION OF EXAMPLE 12 FROM REFERENCE 2

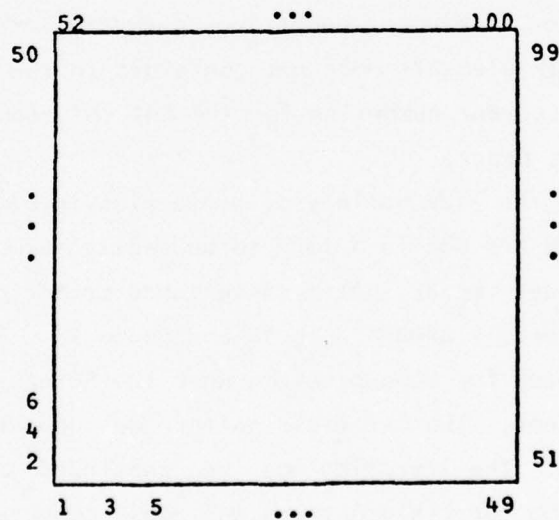
TYPE: Square loop

DIMENSIONS: 2.5 meters on each side

$R_W = 0.0015$ ,  $\lambda = 1$

SEGMENTATION: 10 segments per meter, total of 100

SEGMENT NUMBERING:



Excitation: Segment 25 (center of bottom edge)

EXACT SOLUTION CP TIME (sec): 4.178

square loop antenna. Dimensions are in meters. The strip numbering scheme produces the segment numbering shown if the strips are oriented properly. (The vector  $d$  in figure 4 would be tilted 45 degrees to the right.) Table 3 shows the convergence data obtained. Efficiencies are shown based both on comparative computer central processor times and on comparative numbers of multiplicative operations.

The problem with using an automated PASS system for this problem is that the geometry is redundant. The principal axes can lie either parallel to the sides of the square or pass through its corners. The former would yield a poor numbering scheme, because numbering would be sequential along one edge, then alternate between opposite sides. An efficiency greater than three is unlikely with such numbering.

It would be possible, however, to automate a slicing system for numbering that would allow the user to specify the orientation for the vector  $d$ .

For the numbering actually used, the bandwidth for efficient solution could have been estimated from figure 9 using an object length (corner to corner circumferential distance) of  $5\lambda$ . A distance  $R_M$  of about  $0.7\lambda$  is suggested by figure 9. The difference in segment numbers for segments separated by  $0.7\lambda$  is 14. A bandwidth of 14 provided peak efficiency.

### 3. Modified AMP

The results documented in references 1 and 2 were sufficiently encouraging to motivate development of a computer program for solving large problems. The AMP (Antenna Modeling Program) was selected for modification (reference 13). The AMP code uses the same moments formalism as the WAMP code except for continuity schemes at junctions. Reference 4 discusses the modifications and the resulting code.

A number of problems of intermediate size ( $N \leq 300$ ) was investigated (reference 4). The most important of these were the wire grid models of conducting objects of various shapes. A parameter study (wire radius, segment length and associated mesh size) was conducted for two sphere problems.



TABLE 3. RELATIVE ERROR (PERCENT) AND CP TIME (SECONDS)  
FOR EXAMPLE 12 FROM REFERENCE 2

ITERATIONS	BANDWIDTH				
	6	10	14	18	22
1	47.09	22.36	10.70	12.47	10.50
2	23.98	4.95	1.25	1.67	.97
3	12.49	1.17	.22	.23	
4	6.53	.28			
5	3.42				
6	1.79				
7	.94				
TIME	0.738	0.477	0.453	0.577	0.591
EFF (CP TIME)	5.7	8.8	9.2	7.2	7.1
EFF (MO'S)	5.3	8.5	8.8	6.8	6.5

The reader is referred to reference 4 for the details and to reference 8 for a summary. The resulting guidelines call for segment lengths somewhat less than  $0.2\lambda$  as a maximum and a wire radius of about  $0.025\lambda$ . Predicted far field patterns and bistatic scattering cross sections for models constructed with these guidelines were consistently in good agreement with the independent results from the literature.

The modeled objects in this study all had rotational symmetry. The models were constructed with many-fold rotational symmetry. Both this symmetry and the iterative method were used in the solution process. Due to symmetry operations performed on the matrix, the iterative method was not highly efficient in this study because large submatrices and bandwidths were required. This is not especially important, because the only significant cost for such problems is in generating part of the impedance matrix.

Reference 5 includes a number of example problems with  $N$  ranging up to 1000. The solutions were mostly obtained without using symmetries. Banded matrix iteration is shown to be a useful solution method for large problems.

Most of these example problems were chosen because the predicted current distribution or far fields could be compared to independent results from the literature. Few problems of the desired electrical size range have been solved for current distributions, so most of the comparisons are to theoretical far fields. As noted previously, reasonably good far fields can be obtained from inaccurate currents. Comparison to theoretical far fields is not the best validation for choice of model parameters.

Comparisons of shapes of grid current distributions and surface current distributions are possible in some cases. The wires usually must be oriented on the surface along the natural coordinates, because surface currents are computed by component along those coordinates. A rectangular plate modeled by a square mesh grid is an obvious example. For a sphere, the natural wire orientations are along lines of latitude and longitude. For plane wave scattering, surface currents are known for the E- and H-planes. If the plane wave is incident along the polar axis, H-plane currents are  $\phi$ -directed and can be compared to currents on wires crossing the H-plane and oriented along lines of latitude. E-plane surface currents cannot be compared to currents on a set of wires along a line of longitude, because these currents break up and run through the pole on a variety of wire paths. If the plane wave is incident along a line normal to the polar axis and the electric field is in the equatorial plane, both comparisons are possible. In the E-plane, the grid is essentially rectangular. Currents are  $\phi$ -directed in the H-plane, and can be compared to currents on wires along lines of latitude except at the poles. Such a comparison is shown in figure 14 for a sphere with  $ka$  equal to 4.7 (example 13 from reference 5). The model used 996 wire segments for a surface area of 7 square wavelengths. The predicted bistatic scattering cross section was in excellent agreement with the exact theoretical results of King and Wu (reference 14).

In general, the iterative process yields good efficiencies for planar and near-planar wire grids when the strip numbering scheme is used and the bandwidth is chosen from figure 9. It also works well for cylinders with diameters less than about a half-wavelength. For fat cylinders and spheres, larger bandwidths are required for convergence. Bandwidths chosen from figure 9 for these problems yield pseudoconvergence or divergence. No rule for bandwidth selection in such cases was found since the study of such problems was brief. It is possible that internal modes contribute to this problem; example 15 of reference 5 was a single attempt to investigate this possibility.

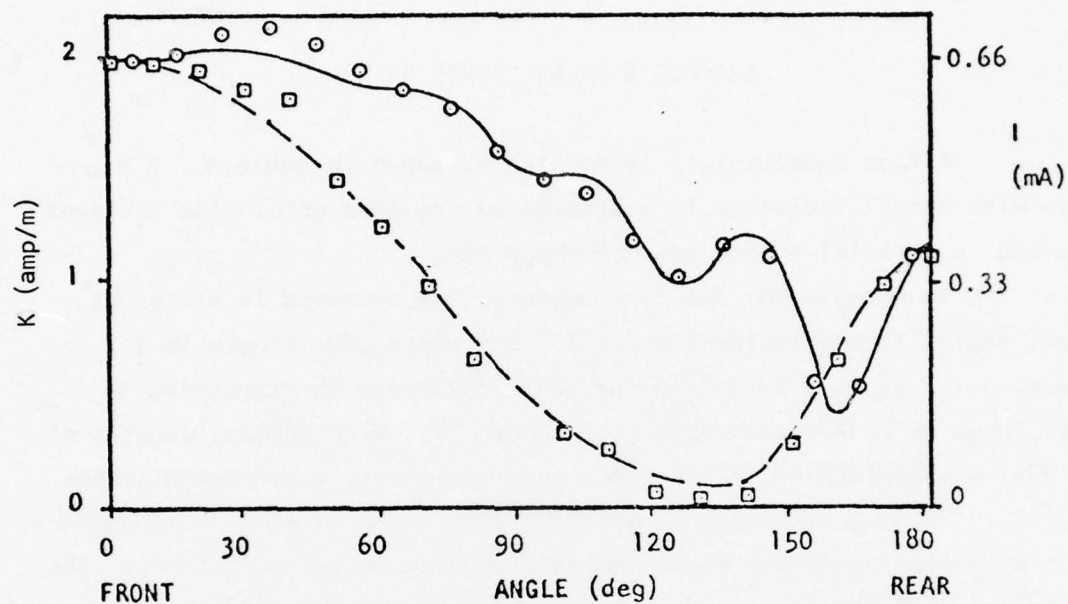


Figure 14. Amplitude of Current on a Sphere for Plane Wave Scattering,  $ka = 4.7$ , Example 13 of Reference 5 (Surface Currents  $K$  from Reference 14; Solid Line for E-Plane, Dashed for H-Plane. Wire Grid Currents  $I$ ;  $\circ$  for E-Plane,  $\square$  for Near H-Plane.)



As an example of the application of the iterative process in larger problems, example 6 of reference 5 is reproduced here.

#### EXAMPLE 6 OF REFERENCE 5

A flat square plate is modeled as shown in table 4. A plane wave with normal incidence is scattered by the wire grid. The incident E-field is parallel to one edge of the plate.

In example 6A, the wire segments are numbered in strips at right angles to the incident E-field. The plate edge length is  $2\lambda$ . Figure 9 indicates a bandwidth for peak efficiency corresponding to a distance of  $0.3\lambda$  for an object of length  $2\lambda$ . With segment lengths of  $0.125\lambda$ , a bandwidth of 132 includes interactions to a minimum distance of  $0.5\lambda$ . Table 5 shows the convergence data. Convergence is so rapid that a smaller bandwidth would probably provide better efficiency. The normalized bistatic cross sections in the E- and H-planes are shown in figures 15 and 16. The backscatter cross section  $\sigma/\lambda^2$  is 220. The pivot ratio was 20.0. The matrix fill time was 608 seconds and the solution time was 138 seconds.

Example 6B is identical to example 6A except for orientation of the incident field, which is parallel to the X-axis. This is equivalent to retaining the orientation parallel to the Y-axis and numbering in strips normal to the X-axis. The two are physically equivalent problems. The convergence data are shown in table 6. The solutions for the two examples were the same within about 1 percent in the regions of large current.

Currents parallel to the field are shown in figures 17(a), 17(b), and 17(c) for wires along the edge, next to the edge, and in the interior of the grid. The edge wires carry a larger current as expected. The wires next to the edge carry slightly less current than interior wires.

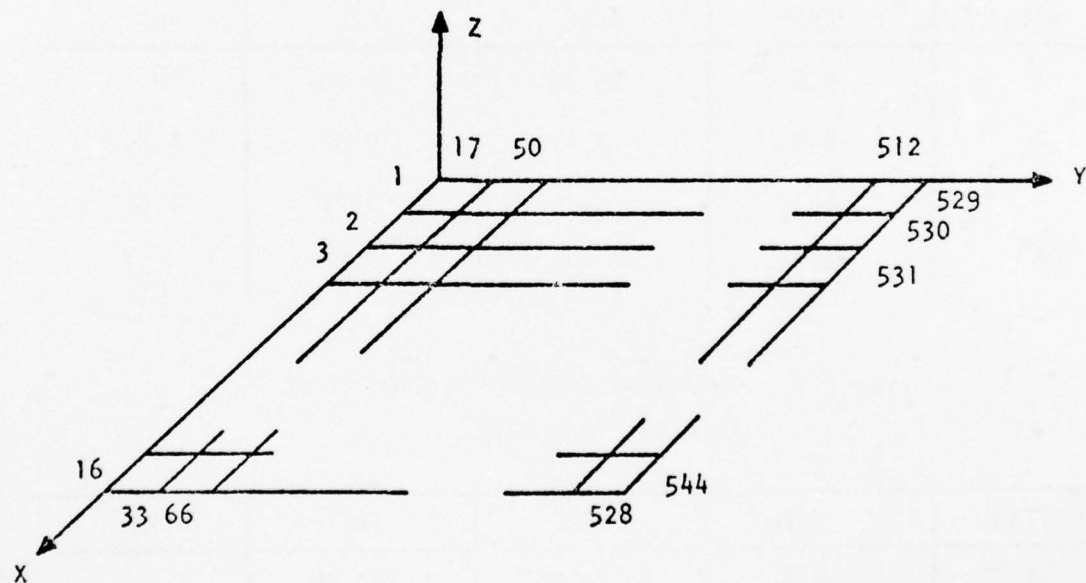
TABLE 4. DESCRIPTION OF EXAMPLE 6 FROM REFERENCE 5

TYPE: SQUARE PLATE

DIMENSIONS:  $L = 2$ ,  $W = 2$ ,  $R_w = 0.025$ ;  $\lambda = 1$  (6A, 'B');  
 $\lambda = 1.176$  (6C)

SEGMENTATION: SQUARE GRID, 16 SEGMENTS PER EDGE, TOTAL OF 544

SEGMENT NUMBERING:



EXCITATION: PLANE WAVE, NORMAL INCIDENCE, E PARALLEL TO ONE EDGE

TABLE 5. CONVERGENCE DATA FOR EXAMPLE 6A  
(N = 544, M = 132)

ITER	EFF	BCRE	IRE	PRE
1	6.8	13.68	100.00	-
2	6.5	3.60	15.47	2.39
3	6.3		3.29	.70

TABLE 6. CONVERGENCE DATA FOR EXAMPLE 6B  
(N = 544, M = 132)

ITER	EFF	BCRE	IRE	PRE
1	6.8	25.76	100.00	-
2	6.5	7.47	20.50	4.20
3	6.3	2.19	5.77	1.62
4	6.1		1.81	.57

TABLE 7. CONVERGENCE DATA FOR EXAMPLE 6C  
(N = 544, M = 132)

ITER	EFF	BCRE	IRE	PRE
1	6.8	17.07	100.00	-
2	6.5	4.00	17.98	3.23
3	6.3		3.89	.84

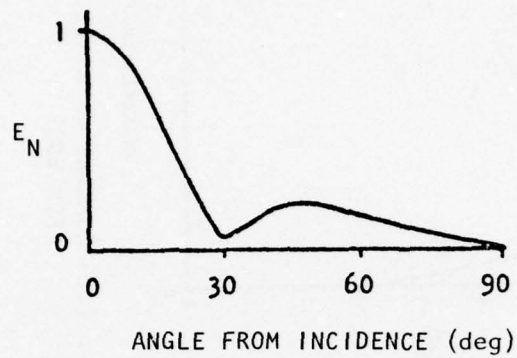


Figure 15. Normalized E-Plane Bistatic Cross Section for a Wire Gridded Plate, Example 6A

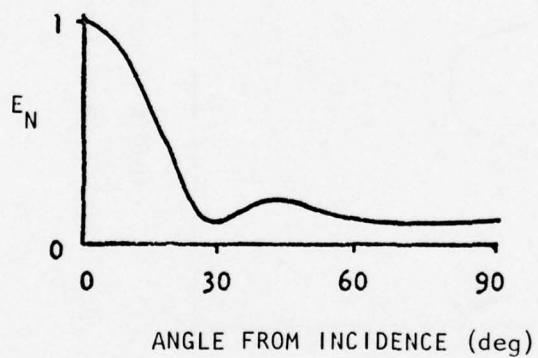


Figure 16. Normalized H-Plane Bistatic Cross Section for a Wire Gridded Plate, Example 6A



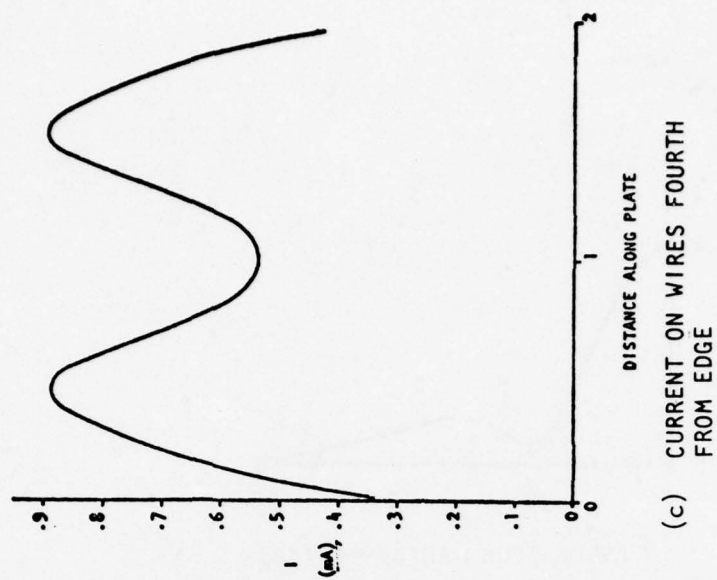
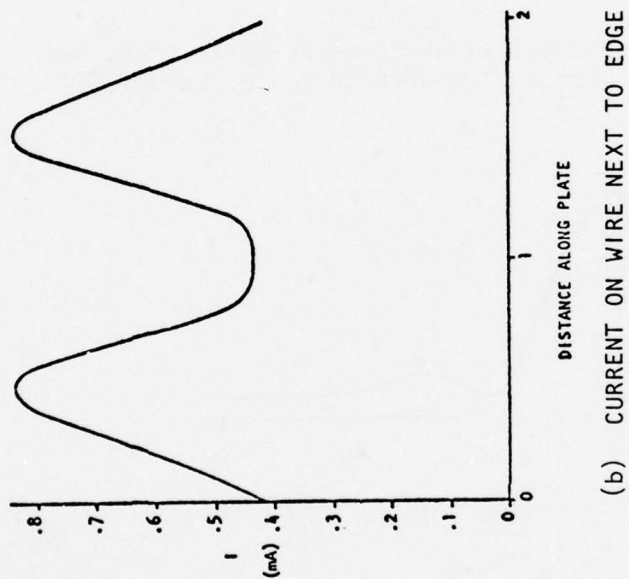
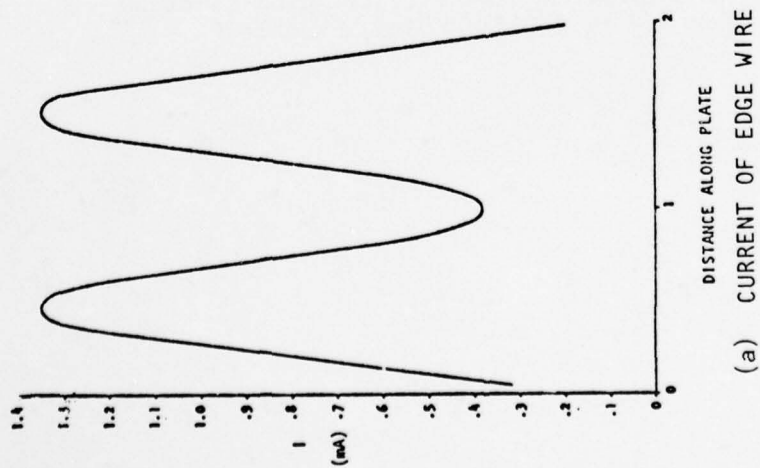


Figure 17. Sample Wire Grid Currents for Example 6A or 6B

Currents normal to the E-field are zero along the centerline wires due to symmetry. They are small everywhere compared to currents parallel to the field, and are largest at the edges. Figure 18 shows the approximate edge current normal to the field. These small currents are subject to considerable error due to the 1 percent convergence criterion. The upturn at the corners is due to the difference in boundary conditions between plates and wire grids.

Comparison of tables 5 and 6 shows that the error in  $X_1$  is considerably larger for example 6B, although the final efficiencies are not much different. The higher initial error is due to the direction of the E-field (and hence the currents) relative to the orientation of the strips used in segment numbering. Interactions between segments at moderate distances are largest when the segments are parallel to each other and normal to the line between their centers. In example 6A, the banded matrix includes distant interactions between parallel segments with large currents and between collinear or nearly collinear segments with essentially no current. In example 6B, the opposite is true. Hence, although exactly the same matrix operations are involved in the two cases, the excitation affects the results considerably.

Example 6C differs from example 6A only in the wavelength. With  $\lambda$  equal to 1.176, the quantity  $kW/2$  or  $\pi W/\lambda$  is equal to the square root of 28. Ufimtsev (reference 15) has investigated plane wave scattering from an infinite strip with this parameter value for the strip width. For normal incidence and E across the strip (H-polarization), he gives the normalized far field amplitude shown in figure 19. For E parallel to the strip (E-polarization), he gives the normalized far field amplitude shown in figure 20 by a solid line. With the same normalization, the far field in the E-plane for the wire grid is identical to figure 19 within graph reading limitations. The far field in the H-plane differed from the strip results as shown by dots in figure 20.

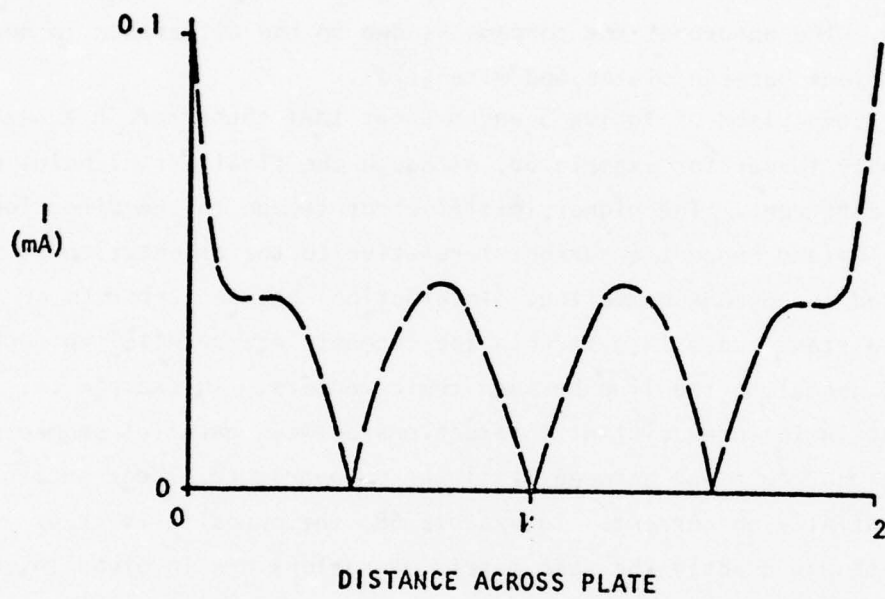


Figure 18. Wire Currents Along Edge Normal to The E-Field, Example 6

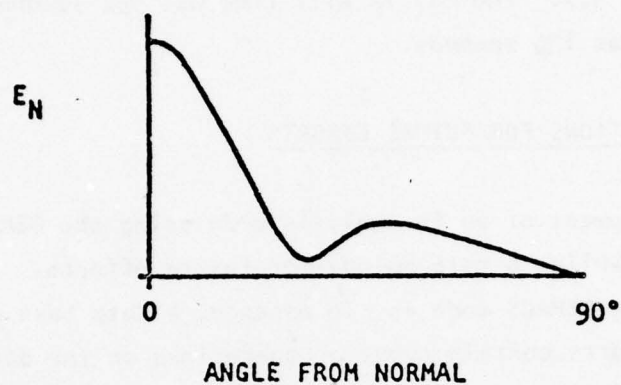


Figure 19. Far Field for Plane Wave Scattering from a Strip, H-Polarization, Reference 15

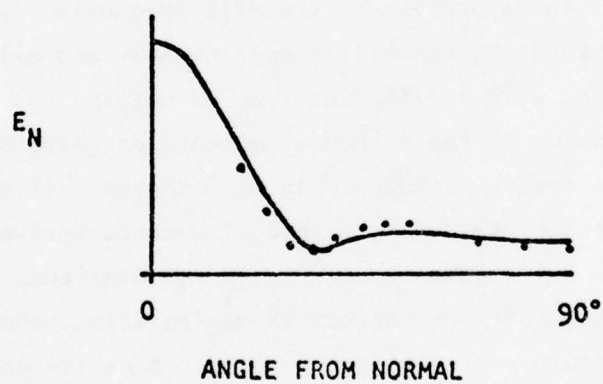


Figure 20. Far Field for Plane Wave Scattering from a Strip, E-Polarization (Line from Reference 15, Points from Wire Grid)



Convergence data for example 6C are shown in table 7. The pivot ratio was 9.7. The matrix fill time was 592 seconds, and the solution time was 136 seconds.

#### E. RECOMMENDATIONS FOR FUTURE EFFORTS

The development of an EM analysis code using the GEMACS architecture should establish a methodology for future efforts.

The present GEMACS code is, in essence, a data base manipulation tool which also supports certain types of operations on the data involved. The current operations result in the EM analysis of those structures and antennas which can be modeled using the thin-wire approximation to the EFIE with a sine + cosine + pulse expansion function. Additional capability in the method of moments areas should be added which would allow a consistent analysis of the modeling requirements based on different expansion and weighing functions.

Additionally, incorporation of the MFIE (Magnetic Field Integral Equation) would extend the capability considerably and allow investigation of the BMI technique with a different type of matrix.

Besides expansion of the method of moments oriented solution technique, diffraction theory methods could be included. If properly done, this would support analysis using method of moments derived current distributions with diffraction theory field computations.

With additional software for matrix manipulation, the diakoptic solution process could be investigated to determine its applicability to field coupled problems. This technique is already applied to distributed power networks and mechanical systems with a great deal of success.

Besides increasing the capability of GEMACS to solve a larger class of problems, there are some software improvements which could greatly reduce the size and run time of the program. These improvements would

not correspond to ANSI FORTRAN IV; however, the resultant code would still run on a large number of second and third generation computers. The two most obvious improvements are random access I/O and dynamic core allocation. Both of these operations require software peculiar to the host machine and are generally available.

#### REFERENCES

1. Ferguson, T. R. The EMCAP (Electromagnetic Compatibility Analysis Program) Iterative Techniques in the Method-of-Moments, The BDM Corporation, RADC-TR-75-121, May 1975, AD-A011668.
2. Ferguson, T. R. Solution of Thin Wire Moments Problems by Banded Matrix Iteration, The BDM Corporation, RADC-TR-75-189, July 1975, AD-A015826.
3. Ferguson, T. R. The EMCAP (Electromagnetic Compatibility Analysis Program) Properties of the Banded Matrix Iterative Solution Technique for Thin Wire Moments Problems, The BDM Corporation, RADC-TR-75-272, November 1975, AD-A018444.
4. Ferguson, T. R. Wire Moments Problems of Intermediate Size, The BDM Corporation, RADC-TR-76-48, March 1976, AD-A023198.
5. Ferguson, T. R. The EMCAP (Electromagnetic Compatibility Analysis Program) Wire Moments Problems of Large Size, The BDM Corporation, RADC-TR-76-122, May 1976, AD-A026402.
6. Ferguson, T. R. "Banded Matrix Iteration in Moments Problems," AP-S International Symposium, June 1975, pp. 146-149.
7. Ferguson, T. R., T. H. Lehman, and R. J. Balestri. "Efficient Solution of Large Moments Problems: Theory and Small Problem Results," IEEE Trans. Ant. Prop., Vol. 24, No. 2, March 1976.
8. Ferguson, T. R. and R. J. Balestri. "Solution of Large Wire Grid Moments Problems," IEEE International Symposium on Electromagnetic Compatibility, July 1976.
9. Forsythe, G. E. and C. B. Moler. Computer Solution of Linear Algebraic Systems, Prentice-Hall, 1967.
10. Mittra, R. and C. A. Klein. "The Use of Pivot Ratios as a Guide to Stability of Matrix Equations Arising in the Method-of-Moments," IEEE Trans. Antennas and Propagation (Commun.), May 1975, pp. 448-450.
11. Harrington, R. F. Field Computation by Moment Methods, Macmillan Co., New York, 1968.

12. Deadrick, F. J. and E. K. Miller. Program WAMP (Wire Antenna Modeling Program), (UCID-30084), Lawrence Livermore Laboratory, December 1973 (a modified version of a program created by MB Associates).
13. The Antenna Modeling Program is a general purpose thin-wire code developed and documented by MB Associates.
14. King, R. W. P., and T. T. Wu. The Scattering and Diffraction of Waves, Harvard University Press, Cambridge, Mass., 1959. Copyright 1959 by the President and Fellows of Harvard College.
15. Ufimtsev, P. Ia. "Secondary Diffraction of Electromagnetic Waves by a Strip," Soviet Phys. - Techn. Phys. 3, 1952, p. 535.
16. MB Associates. "Antenna Modeling Program - Engineering Manual," July 1972, AD-A025890.



AD-A040 027

BDM CORP ALBUQUERQUE N MEX  
GENERAL ELECTROMAGNETIC MODEL FOR THE ANALYSIS OF COMPLEX SYSTEMS--ETC(U)  
APR 77 R J BALESTRI, T R FERGUSON

F/G 20/3

F30602-74-C-0182

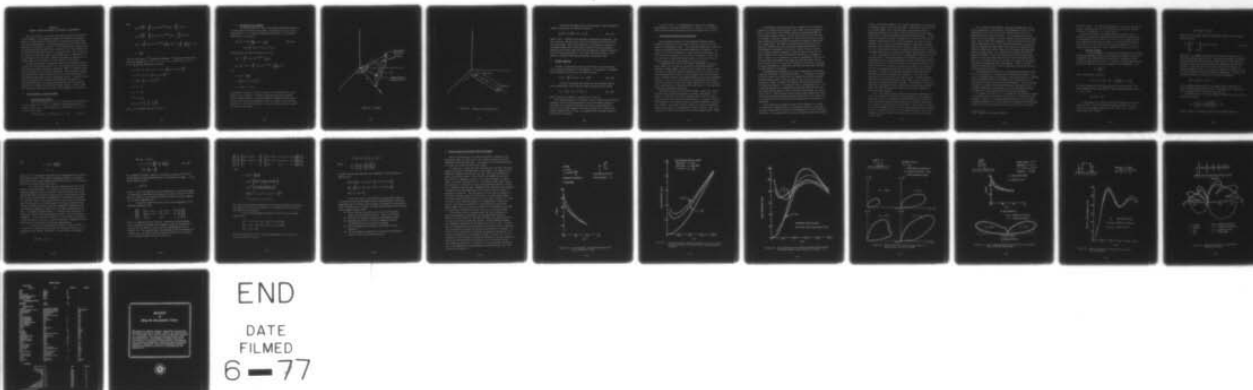
RADC-TR-77-137-VOL-2

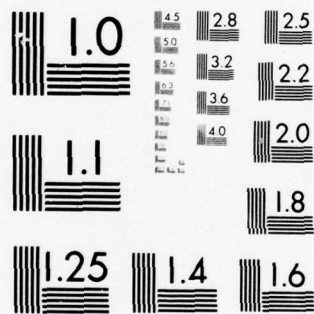
NL

UNCLASSIFIED

2 OF 2

AD  
A040027





MICROCOPY RESOLUTION TEST CHART  
NATIONAL BUREAU OF STANDARDS-1963-A

## APPENDIX A

### ANTENNA SYSTEM EFFECTIVENESS AS AFFECTED BY ENVIRONMENT

The effectiveness of an antenna system can be adversely affected by its environment. As one example, consider the frequently encountered problem in antenna siting of realistically including the ground effects upon the antenna behavior. The antenna properties can be influenced by the ground in essentially two ways: (1) by modifying the antenna current distribution through the near-field interaction; (2) and by changing the far-field radiation pattern from its free-space value. Even in the case of a perfectly conducting ground, where image theory is applicable in a straightforward way, the mutual interaction between the antenna and its ground image must be allowed for if the coupling is significant.

The antenna engineer is oftentimes faced with the task of designing a system with certain characteristics in a particular ground environment. The rigorous approach presented by Sommerfeld (1964) is somewhat cumbersome and lengthy even for computer evaluation. An accurate but approximate method which surmounts the numerical difficulties associated with the Sommerfeld approach is used in the GEMACS program. A tested integral equation approach for free-space antenna analysis was modified in a straightforward manner to provide an accurate and efficient numerical procedure for handling the antenna/half-space problem. Fresnel plane-wave reflection coefficients are used to allow modeling of the ground.

#### A. THE DIFFERENTIAL FIELD OVER GROUND

##### 1. Vertical Source Segment

The Hertzian potential,  $\bar{d}\pi_v$ , of a vertically directed electric current filament of strength  $Id\ell$  located in free space above a half-space of permittivity  $\epsilon_1$  and conductivity  $\sigma_1$  defined by  $z \leq 0$  is given by (Sommerfeld, 1964)

$$\bar{d}\pi_v(\bar{r}) = \hat{z} d\pi_v(\bar{r}) = \hat{z} \int P(\bar{r}') d\ell \{g_d + g_i - g_s\} \quad (\text{Eq. A-1})$$

where

$$g_d = \frac{e^{-ikR}}{R} = \int_0^\infty J_0(\lambda \rho'') e^{-\mu |z-z'|} \frac{\lambda}{\mu} d\lambda = \int_0^\infty F(\lambda) d\lambda$$

$$g_i = \frac{e^{-ikR'}}{R'} = \int_0^\infty J_0(\lambda \rho'') e^{-\mu (z+z')} \frac{\lambda}{\mu} d\lambda = \int_0^\infty F_i(\lambda) d\lambda$$

$$g_s = 2 \int_0^\infty J_0(\lambda \rho'') e^{-\mu (z+z')} \frac{\mu_E}{\epsilon_E \mu + \mu_E} \frac{\lambda}{\mu} d\lambda = 2 \int_0^\infty \frac{\mu_E}{\epsilon_E \mu + \mu_E} F_i(\lambda) d\lambda$$

$$P = \frac{i\omega\mu_0}{4\pi}$$

with the time factor  $e^{j\omega t}$  suppressed throughout. The source and observation points are denoted by  $\bar{r}'$  ( $x'$ ,  $y'$ ,  $z'$ , or  $\rho'$ ,  $\phi'$ ,  $z'$ ) and  $\bar{r}$  ( $x$ ,  $y$ ,  $z$ , or  $\rho$ ,  $\phi$ ,  $z$ ) respectively (see figure A-1) with

$$\rho'' = |\bar{\rho}''| = |\bar{\rho} - \bar{\rho}'| = |\rho \hat{\rho} - \rho' \hat{\rho}'| = [(x-x')^2 + (y-y')^2]^{1/2}$$

$$R = |\bar{R}| = |\bar{r} - \bar{r}'| = [\rho''^2 + (z-z')^2]^{1/2},$$

$$R' = |\bar{R}'| = [\rho''^2 + (z+z')^2]^{1/2},$$

$$\mu^2 = \lambda^2 - k^2,$$

$$\mu_E^2 = \lambda^2 - k_E^2,$$

$$k^2 = \omega^2 \mu_0 \epsilon_0$$

$$k_E^2 = \epsilon_E k^2 = \frac{\epsilon_1}{\epsilon_0} \left( 1 - \frac{i\sigma_1}{\omega\epsilon_1} \right) k^2$$

and  $J_n$  is the Bessel function of order  $n$ .



## 2. Horizontal Source Segment

The Hertzian potential  $d\bar{\pi}_h$  of a horizontal differential electric current source  $Idl$  pointing at an angle  $\alpha$  with respect to the  $x$  axis at coordinates  $x'$ ,  $y'$ ,  $z'$  above a half-space defined by  $z \leq 0$  of relative permittivity  $\epsilon_E$  is given by

$$d\bar{\pi}_h(\vec{r}) = Pl(\vec{r}') d\lambda \left\{ \left[ g_d - g_i + g_{ss} \right] \hat{s} + g_{sz} \hat{z} \right\} = d\pi_{xh} \hat{x} + d\pi_{yh} \hat{y} + d\pi_{zh} \hat{z} \quad (\text{Eq. A-2})$$

where  $g_d$  and  $g_i$  are given by equation A-1 and

$$g_{ss} = 2 \int_0^\infty J_0(\lambda \rho'') e^{-\mu(z+z')} \frac{\lambda}{\mu + \mu_E} d\lambda$$

$$g_{sz} = \frac{2}{k^2} \cos \phi'' \int_0^\infty J'_0(\lambda \rho'') e^{-\mu(z+z')} \frac{\mu - \mu_E}{\epsilon_E \mu + \mu_E} \lambda^2 d\lambda$$

with

$$\phi'' = \tan^{-1} \frac{y-y'}{x-x'},$$

$$\rho'' = \left[ (x-x')^2 + (y-y')^2 \right]^{1/2},$$

$$\hat{s} = \hat{x} \cos \alpha + \hat{y} \sin \alpha,$$

as depicted in figures A-1 and A-2, and  $J'_0$  is the derivative of  $J_0$  with respect to its argument. It should be observed that the horizontal antenna produces not only a Hertzian potential aligned with the current filament, but a vertical component as well as a result of the half-space interaction. Note also the change in sign of the image term  $g_i$  compared with the vertical source.

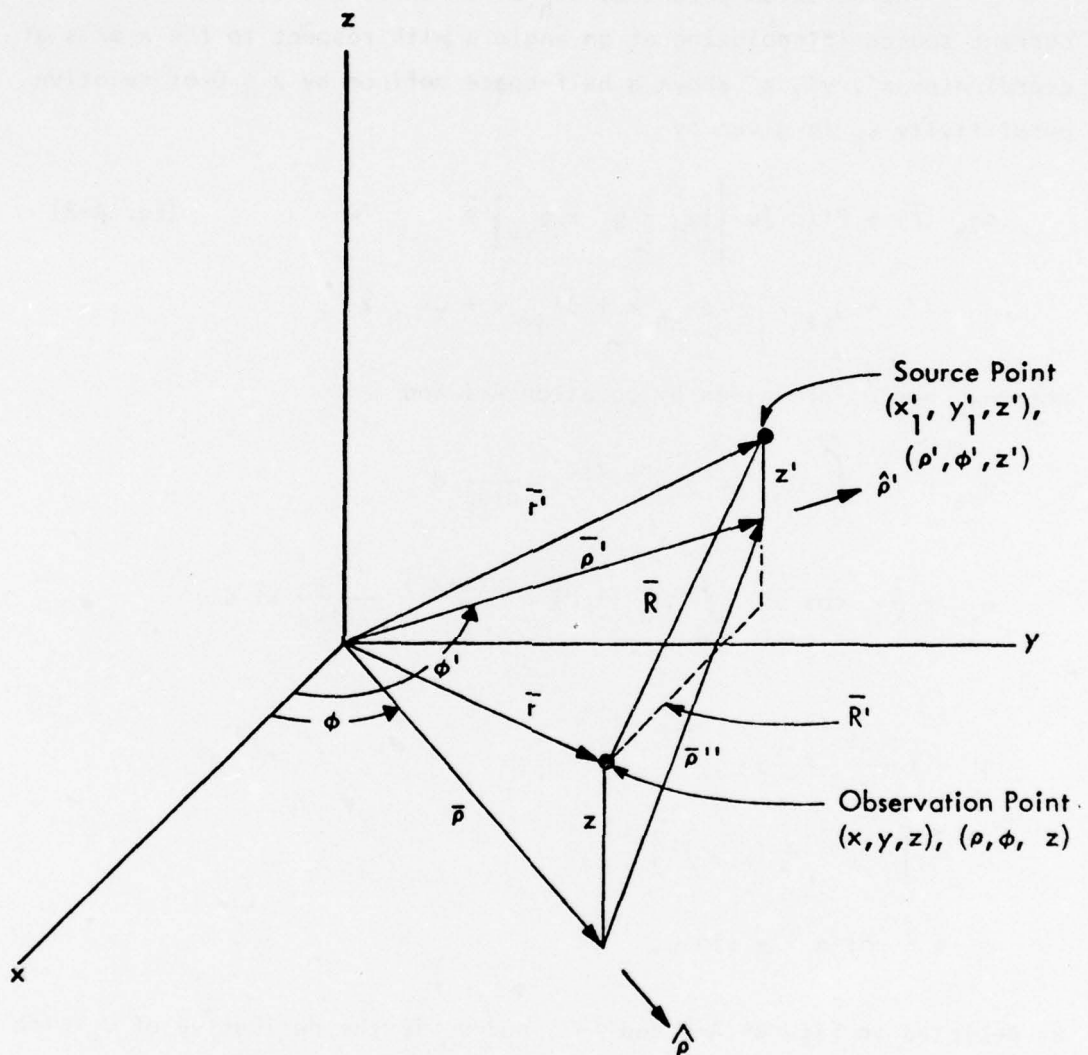


Figure A-1. Geometry

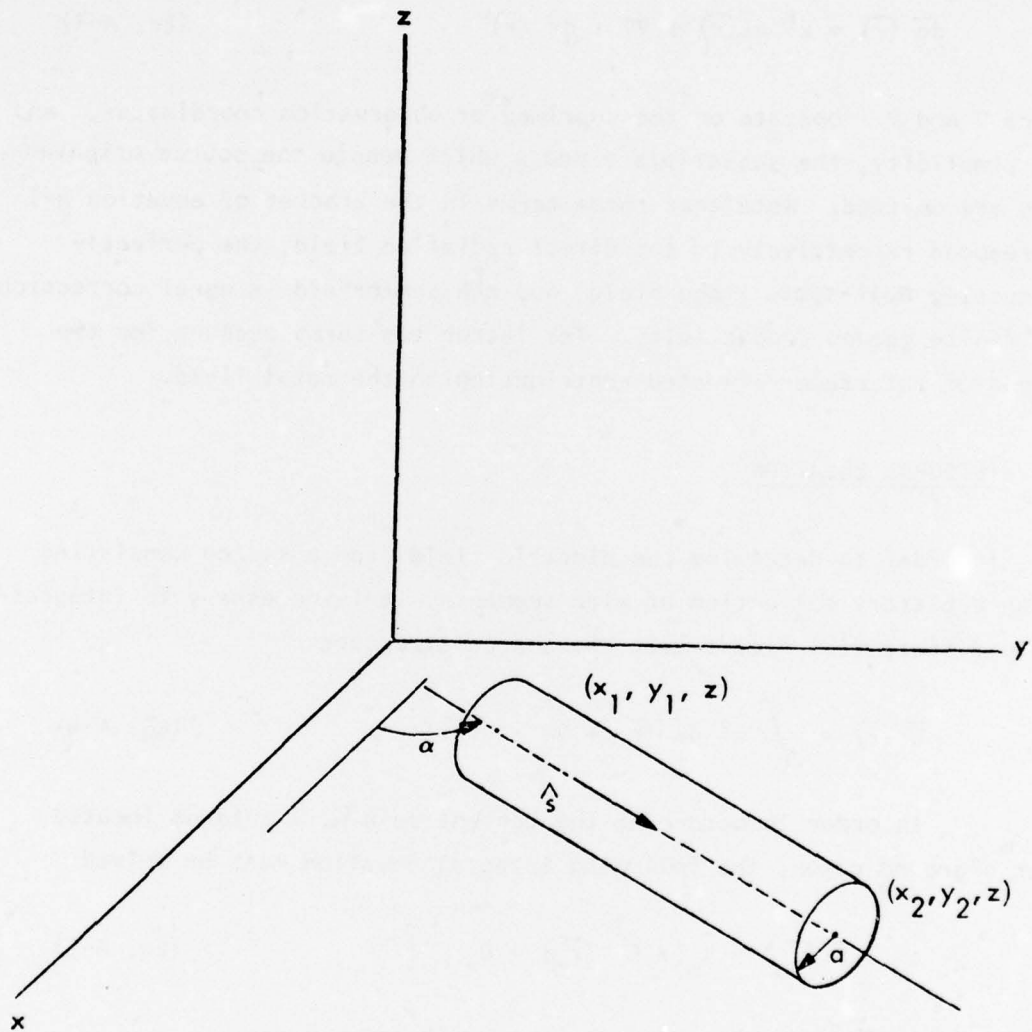


Figure A-2. Geometry for Horizontal Wire

For both of the above cases, an expression for the differential electric field,  $d\bar{e}$  of the source is given by

$$d\bar{e}(\bar{r}) = k^2 d\bar{\pi}(\bar{r}) + \nabla \nabla \cdot d\bar{\pi}(\bar{r}) \quad (\text{Eq. A-3})$$

where  $\nabla$  and  $\nabla \cdot$  operate on the unprimed or observation coordinates, and for simplicity, the subscripts  $v$  and  $h$  which denote the source orientation are omitted. Note that three terms in the bracket of equation A-1 correspond respectively to the direct radiation field, the perfectly conducting half-space image field, and the Sommerfeld integral correction for finite ground conductivity. The latter two terms account for the ground or interface-reflected contribution to the total field.

#### B. INTEGRAL EQUATION

In order to determine the electric field from a source consisting of an arbitrary collection of wire segments, it is necessary to integrate these differential fields over the source structure

$$\bar{E}(\bar{r}) = \int_L k^2 d\bar{\pi}(\bar{r}) + \nabla \nabla \cdot d\bar{\pi}(\bar{r}) \quad (\text{Eq. A-4})$$

In order to determine the current on a wire antenna located over a ground plane, the following integral equation must be solved

$$\hat{s}_0 \cdot \bar{E}(\bar{r}_0) - \hat{s}_0 \cdot \bar{E}^I(\bar{r}_0) = 0 \quad (\text{Eq. A-5})$$

where  $\hat{s}_0$  and  $\bar{r}_0$  are defined in subsections A.1 and A.2.

This integral equation is rigorously correct (within the restrictions imposed by the thin-wire approximation) for a wire-antenna located in free-space over a ground of arbitrary permittivity and conductivity. The resulting integral equation thus has a portion which involves the double integration over  $S'$  and  $\lambda$ , a procedure that in general cannot be analytically carried out.



In view of this, it is advantageous to make use of reasonable approximations to provide a method which is simpler to use and which does not significantly degrade the numerical accuracy of our results.

#### C. THE REFLECTION COEFFICIENT APPROXIMATION

One approximate solution for the Sommerfeld integral employs asymptotic expansions for the integral which are valid over various ranges of the parameter values. This particular method makes use of the method of stationary phase and double saddle-point integration. The results from using this approach include closed form expressions for the fields of an elementary source, electric or magnetic, useful over various ranges of observation point location relative to the source, and involving the electrical parameters of the two media.

A comprehensive survey of this general methodology is given by Banos (1966), and the numerical accuracy of these approximations is examined by Siegel (1970). Siegel's work is especially useful in that he is able to establish ranges of observation distance for which the various expressions are valid, but unfortunately also shows that gaps exist in general over which the approximations do not provide acceptable accuracy. This is true in particular for observation points located close to the source, so that the integral equation A-3, which requires this close proximity of observation and source points is not amenable to using these approximate expressions.

Other formulations of this general problem, suitable for possibly more physically based approximations, have been investigated. The reader is referred to the work by Feynberg (1967), where a surface integration over the interface induced sources is discussed, with many other aspects of the problem, and the conference proceedings edited by Wait (1969a). The latter provides a number of interesting treatments, including one based on the compensation theorem (Surtees, 1969) and a comparison of several formulations for antenna impedance (Wait, 1969b).

In developing an approximate solution to equation A-5, we chose to proceed on a primarily physical basis, and further to seek an approach which is well suited to the integral equation treatment developed for the free-space antenna problem. We have noted that the first two terms in the Green's function of equations A-1 and A-2 are the direct or free-space radiation and the perfectly conducting half-space or image radiation, respectively. The image term represents the contribution of a specularly reflected ray from a perfectly conducting half-space, the electromagnetic equivalent of an optically perfect mirror in optics. This ray optics specular component is thus rigorously correct for the perfect conductor for which the Sommerfeld correction,  $g_s$ , becomes a zero. Further, the  $\lambda$ -integration, as shown in equations A-1 and A-2 can be analytically performed for the image term (and the direct term as well) so that there is no significant increase in difficulty in treating an antenna located over a perfectly conducting half-space over analyzing the same antenna in free-space.

The advantage of extending the ray optics approach to the finitely conducting half-space is immediately evident. If a specularly reflected ray can be used in this case as well to account for the entire ground-reflected contribution ( $g_i$  and  $g_s$  terms) to the field, then it may be possible to largely circumvent the numerical difficulties presented by the Sommerfeld integral. Two problems arise in accomplishing this -- one is the determination of the appropriate reflection coefficient for the half-space, and the other is that of specifying the specular ray contribution itself. These problems are both brought about because the fields involved are non-plane wave and the observation point can in general lie in the near-field of the source where the higher order terms may be of importance.

Some insight may be gained by viewing the interface as a surface distribution of induced sources, as discussed by Feynberg. The ground-reflected contribution to the total field produced by a given infinitesimal source is then obtained from a surface integration over these induced

sources. Practically speaking, this surface integration can be truncated to include a region of only limited extent. Upon applying the principle of stationary phase, this truncated region (or essential region as denoted by Feynberg) can be shown to be of generally elliptical shape and centered in some sense about the specular reflection point. If the area of this essential region is allowed in the limit to shrink to zero centered on the specular point, only the specular ray itself will be obtained. Thus, a ray optics approach based on a specular ray amounts essentially to collapsing the entire interface induced source distribution to a single point from which the ground reflected field at a particular observation point to a given infinitesimal source appears to originate.

This is equivalent to the use of an image source to account for the reflected field. The principle applies to extended sources as well, by integrating over the corresponding specular point distribution of equivalent image sources. Since this picture of the reflection process is of course, exact for the perfectly conducting half-space, its extension to the finitely conducting problem with a minimum of modification appears expedient. To obtain the functional dependence of the total ground reflected field upon the geometrical parameters, it follows that equation A-1 with the  $g_i$  term only should be used. Complete specular reflection of the field components of all orders is thus presumed (unit magnitude reflection coefficients assumed). The effect of finite ground conductivity consequently enters below only via a modified reflection coefficient which multiplies the image fields, and thus effectively alters the image strength.

Again, the simplest extension beyond the perfectly conducting case which will introduce the ground electrical parameters in an apparently meaningful way is to be preferred. Certainly the simplest reflection coefficient which could be employed would be one based on plane waves, the so-called Fresnel reflection coefficients. Since these are, however, polarization dependent, and the vertical and horizontal field components reflect in different ways as well, the ground reflected field must be decomposed into the usual TE (transverse electric) and TM (transverse magnetic modes).



This is readily accomplished by breaking the image field, or  $g_i$ , terms of equation A-4, into electric field components lying in TM and perpendicular to TE the vertical plane containing the source and observation points (incidence plane). The TM components are further identified as a horizontal or vertical relative to the horizontal interface. Each of these field components is then multiplied by the corresponding plane wave electric field reflection coefficient, using as the angle of incidence the angle made by the specular ray connecting the source and observation points (midpoints of the source and observation segments, respectively). This procedure thus neglects the possible angle of incidence variation resulting from a non-zero length source segment for which the actual specular point distribution would be the path on the interface traced by a straight line drawn from the observation point and scanned over the image segment. Finally, the total tangential observation point field is obtained as the sum of the direct and ground reflected fields.

The approach described above is a straightforward extension to the EFIE<sup>1</sup> for free-space, or to the perfectly conducting half-space. Yet, as will be demonstrated by the numerical results which follow, it provides surprisingly good results for the analysis of wire antennas, over a half-space with widely varying electrical parameters. Since the method is based on a surface reflection coefficient at the specular point, it is readily adapted to a horizontally stratified half-space, and to a half-space with slowly varying properties along the interface.

For reasons of simplicity, it is assumed that the antenna is located in free-space above a horizontal ground with the x-y plane forming the interface. Since any wire segment can be specified in terms of three orthogonal components, it is only necessary to determine the differential fields due to a vertical Hertzian source and an arbitrarily oriented

---

<sup>1</sup>EFIE: Electric Field Integral Equation



horizontal source. The following development is limited to the vertical source. Subsequent sections will deal with the arbitrarily oriented horizontal wire segments in a similar fashion.

The reflection coefficient approximation, the name by which we characterize the modified image method outlined above, represents only a simple extension to the EFIE for the case of a wire antenna located over a perfectly conducting half space. To provide some theoretical justification for the reflection coefficient approximation it will be compared with the rigorously correct Sommerfeld integral formulation.

#### 1. Vertical Filament

It will be convenient in comparing the Sommerfeld and reflection coefficient approaches (and no loss of generality results) to deal with the differential fields  $d\bar{E}$  which result from an incremental current filament  $dl$  located on the  $z$  axis. In addition, the principal polarized fields are simply the cylindrical coordinate system components. Let

$$Q = \frac{i\omega\mu_0}{4\pi} dl$$

then, from equation A-1 and A-3

$$d\bar{E}(\bar{\rho}, z) = Q \left[ \hat{z} + \frac{1}{k^2} \nabla \frac{\partial}{\partial z} \right] (g_d + g_i - g_s)$$

The total differential field can be written as the sum of  $d\bar{E}^D$ , the direct component (due to  $g_d$ ) and  $d\bar{E}^R$ , the reflected component (due to  $g_i - g_s$ ) so that

$$d\bar{E} = d\bar{E}^D + d\bar{E}^R$$

As noted above, the reflection coefficient approximation involves computing  $d\bar{E}^R$  in terms of the perfect ground contribution; let us denote the latter image component by  $d\bar{E}^I$  (due to  $g_i$ ). Then  $d\bar{E}^R$  is approximated by  $d\tilde{\bar{E}}^R$  where

$$d\bar{E}^R \approx d\tilde{E}^R = \bar{\Gamma}_V d\bar{E}^I$$

where  $\bar{\Gamma}_V$  is the Fresnel reflection coefficient matrix for the vertical source, given by

$$\bar{\Gamma}_V = \begin{bmatrix} R''_H & 0 \\ 0 & R''_V \end{bmatrix} = R''_H \hat{\rho}\hat{\rho} + R''_V \hat{z}\hat{z} \quad (\text{Eq. A-6})$$

Note that  $\bar{\Gamma}$  is a geometrical function of the relative locations of the source and observation points only. The superscript denotes the electric field polarization relative to the incidence plane (in this case the  $\hat{\rho}$ ,  $\hat{z}$  plane) and the subscript denotes the field component relative to the interface. While only the z- or vertical field is required for the integral equation solution, the horizontal component is required for the far field calculation, and is included for completeness. Of course, the differential electric fields must be similarly decomposed as

$$d\bar{E}^R = dE_H^{R''} \hat{\rho} + dE_V^{R''} \hat{z}$$

with corresponding expressions for the other fields. Note that the vertical dipole produces only z- and  $\rho$ - directed electric fields since the  $\phi$ - components of the various  $\nabla g$  terms are zero.

The coefficients in  $\bar{\Gamma}_V$  are the standard Fresnel plane wave reflection coefficients given by

$$R''_V = \frac{\epsilon_E \cos \theta - \sqrt{\epsilon_E - \sin^2 \theta}}{\epsilon_E \cos \theta + \sqrt{\epsilon_E - \sin^2 \theta}} = -R''_H$$

where the angle of incidence relative to the interface normal is

$$\theta = \cot^{-1} \left\{ \frac{z' + z}{\rho''} \right\}$$

Observe that the plane-wave reflected electric fields are related to the incident field in the same manner as equation A-6, with || corresponding to the TM wave polarization. Note that the reflection coefficients are constant for the self-fields of a single vertical antenna, where the angle of incidence is effectively zero, since  $x = x'$  and  $y = y'$  everywhere on the antenna. For radially separated vertical antennas, this equality no longer holds, however, and the variation of the  $\bar{\Gamma}_V$  matrix with observation and source coordinates must be taken into account.

## 2. Arbitrarily Oriented Horizontal Filament

For the case of an arbitrarily oriented horizontal segment, the reflection coefficient approximation requires that the electric field at a given observation point due to a differential source (or a single antenna segment) be decomposed into components which correspond to the transverse magnetic (TM) and transverse electric (TE) polarizations of a plane wave relative to the incidence plane. It is thus necessary in general to find the three orthogonal components of the field, two of which lie in the plane of incidence (for a non-zero length segment, the source point is taken to be the segment center), and one which is orthogonal to it. The two in-plane field components are the radially and vertically (or  $z$ ) directed parts of the field, while the orthogonal component is the azimuthally directed part, relative to a cylindrical coordinate system on whose vertical or  $z$ -axis the source is located. Since the total field is obtained as the summation of differential fields due to a distribution of sources which will not in general have a common incidence plane, it is necessary to perform the field integration in a convenient, absolute coordinate system, such as cartesian, or cylindrical, with respect to which the source distribution is specified.

It is consequently expedient to express the differential field directions relative to the source-incidence plane, and to then transform this field into components relative to the absolute reference system. Let the in-plane unit vectors which are horizontal and vertical relative to the interface be  $\hat{s}_{||}$  and  $\hat{z}$  respectively and let the orthogonal unit vector to the plane be  $\hat{s}_{\perp}$ . The three field components at observation point  $x, y, z$  (or  $\rho, \phi, z$ ) due to a source at  $x', y', z'$  (or  $\rho', \phi', z'$ ) can be expressed as

$$\begin{aligned} d\vec{E} &= de_x \hat{x} + de_y \hat{y} + de_z \hat{z} = de_{\rho} \hat{\rho} + de_{\phi} \hat{\phi} + de_z \hat{z} \\ &= de_{||} \hat{s}_{||} + de_{\perp} \hat{s}_{\perp} + de_z \hat{z} \end{aligned}$$

where

$$\begin{bmatrix} \hat{s}_{||} \\ \hat{s}_{\perp} \\ \hat{z} \end{bmatrix} = \begin{bmatrix} \cos \phi'' & \sin \phi'' & 0 \\ -\sin \phi'' & \cos \phi'' & 0 \\ 0 & 0 & 1 \end{bmatrix} \begin{bmatrix} \hat{x} \\ \hat{y} \\ \hat{z} \end{bmatrix}$$

(Eq. A-7)

$$= \begin{bmatrix} \cos \gamma & \sin \gamma & 0 \\ -\sin \gamma & \cos \gamma & 0 \\ 0 & 0 & 1 \end{bmatrix} \begin{bmatrix} \hat{\rho} \\ \hat{\phi} \\ \hat{z} \end{bmatrix}$$

$$\begin{bmatrix} \hat{x} \\ \hat{y} \\ \hat{z} \end{bmatrix} = \begin{bmatrix} \cos \phi'' & -\sin \phi'' & 0 \\ \sin \phi'' & \cos \phi'' & 0 \\ 0 & 0 & 1 \end{bmatrix} \begin{bmatrix} \hat{s}_{||} \\ \hat{s}_{\perp} \\ \hat{z} \end{bmatrix}$$

$$\begin{bmatrix} \hat{\rho} \\ \hat{\phi} \\ \hat{z} \end{bmatrix} = \begin{bmatrix} \cos \gamma & -\sin \gamma & 0 \\ \sin \gamma & \cos \gamma & 0 \\ 0 & 0 & 1 \end{bmatrix} \begin{bmatrix} \hat{s}_{||} \\ \hat{s}_{\perp} \\ \hat{z} \end{bmatrix}$$



and

$$\phi'' = \tan^{-1} \left( \frac{y-y'}{x-x'} \right)$$

$$\gamma = \phi'' - \phi$$

Note that  $\phi''$  is the angular coordinate of the observation point relative to the source, and  $\gamma$  is the angular separation between the incidence plane and a radial vector through the observation point. For the special case of the vertical source  $d\epsilon_{\perp}$  is zero.

As a final point concerning the reference directions for the electric field calculation, it is pertinent to mention that the direct, image and Sommerfeld terms of the Green's function produce only longitudinal and radial differential fields relative to the source direction. This is due to the azimuthal independence of a filamentary source and its resultant fields. Thus the differential field is most conveniently found for an arbitrarily directed source in the source-oriented longitudinal and radial directions, and then subsequently transformed into the appropriate components required for the integral equation calculation. For computer implementation it is generally most convenient to arrange the overall numerical procedure entirely in terms of cartesian components. In the following discussion, it will be more illuminating in some instances to use the  $\hat{s}_{||}$ ,  $\hat{s}_{\perp}$  and  $\hat{z}$  directions in demonstrating the application of the reflection coefficient approximation.

Let the radial and longitudinal electric fields referred to the source (or image) oriented cylindrical coordinate system  $(\rho, \delta, \ell)$  be denoted by  $dE_{\rho}$  and  $dE_{\ell}$  respectively. These fields are obtainable from

$$d\vec{E} = dE_{\rho} \hat{\rho} + dE_{\ell} \hat{\ell}$$

$$\begin{aligned}
d\vec{E} &= dE_{\rho} \hat{\rho} + dE_{\ell} \hat{\ell} \\
&= P \int (\ell') d\ell' \left\{ \left[ 1 + \frac{1}{k^2} \frac{\partial^2}{\partial \ell'^2} \right] g \hat{\ell} \right. \\
&\quad \left. + \frac{1}{k^2} \frac{\partial^2}{\partial \rho \partial \ell} g \hat{\rho} \right\}
\end{aligned} \tag{Eq. A-8}$$

for a segment of length  $\Delta$  where  $g$  is the Green's function  $e^{ikr}/r$  with  $r$  the distance from the observation point to the source (or image). In the source centered system

$$r = \sqrt{\rho^2 + \ell^2}$$

with  $\rho$ ,  $\delta$ , and  $\ell$  the observation point coordinates. As previously noted, it is possible to analytically evaluate the  $dE_{\rho}$  and  $dE_{\ell}$  terms of equation A-8 for a cosine or sine current variation, as well as the  $dE_{\rho}$  component for a current independent of  $\ell'$ .

We can now transform from the  $\hat{\rho}$  and  $\hat{\ell}$  field components to the cartesian components using

$$\begin{bmatrix} \hat{x} \\ \hat{y} \\ \hat{z} \end{bmatrix} = \begin{bmatrix} \sin \alpha \sin \delta & \sin \alpha \cos \delta & \cos \alpha \\ -\cos \alpha \sin \delta & -\cos \alpha \cos \delta & \sin \alpha \\ \cos \delta & -\sin \delta & 0 \end{bmatrix} \begin{bmatrix} \hat{\rho} \\ \hat{\delta} \\ \hat{\ell} \end{bmatrix}$$

where  $\delta$  is measured from the vertical. Continuing, we then proceed to the incidence-plane image field components which are expressible in terms of the unit vector  $\hat{s}_i$  and  $\hat{s}_j$  via the transformation given by equation A-7. The required image field components (which we denote with a superscript  $i$  and which come from equation A-8 with  $g = g_i$  relative to the incidence plane) can be put in the form

$$\begin{bmatrix} dE_{||}^I \\ dE_{\perp}^I \\ dE_z^I \end{bmatrix} = \begin{bmatrix} \cos \phi'' & \sin \phi'' & 0 \\ -\sin \phi'' & \cos \phi'' & 0 \\ 0 & 0 & 1 \end{bmatrix} \begin{bmatrix} \sin \alpha \sin \delta & \sin \alpha \cos \delta & \cos \alpha \\ -\cos \alpha \sin \delta & -\cos \alpha \cos \delta & \sin \alpha \\ \cos \delta & -\sin \delta & 0 \end{bmatrix} \begin{bmatrix} dE_{\rho}^I \\ dE_{\delta}^I \\ dE_z^I \end{bmatrix}$$

where

$$\phi'' = \tan^{-1} \left( \frac{y-y'}{x-x'} \right)$$

$$\begin{aligned} \delta &= \tan^{-1} \left[ \frac{(x-x') \sin \alpha + (y-y') \cos \alpha}{z-z'} \right] \\ &= \tan^{-1} \left[ \frac{1 + \cot \alpha \tan \phi''}{\sin \alpha (x-x') (z-z')} \right] \end{aligned}$$

$$\rho = \left[ (x-x')^2 + (y-y')^2 + (z-z')^2 - \ell^2 \right]^{1/2}$$

$$\ell = (x-x') \cos \alpha + (y-y') \sin \alpha$$

Note that the direct field components and the image components as obtained from equation A-8 differ only because  $z'$  is the positive for the former, and negative for the latter.

Since the  $dE_{\delta}^I$  component of electric field is zero, the above simplifies to

$$\begin{aligned} dE_{||}^I &= \sin \delta \sin (\alpha - \phi'') dE_{\rho}^I + \cos (\alpha - \phi'') dE_{\ell}^I \\ dE_{\perp}^I &= -\sin \delta \cos (\alpha - \phi'') dE_{\rho}^I + \sin (\alpha - \phi'') dE_{\ell}^I \\ dE_z^I &= \cos \delta dE_{\rho}^I \end{aligned}$$

Upon multiplication of the  $E_{||}^I$ ,  $E_{\perp}^I$  and  $E_z^I$  components by the reflection coefficient matrix  $\bar{\Gamma}$ , where

$$\vec{\Gamma} = R_H'' \hat{s}_{11} \hat{s}_{11} + R_H^\perp \hat{s}_\perp \hat{s}_\perp + R_V'' \hat{z} \hat{z}$$

where

$$R_H^\perp = \frac{\cos \theta_o - \sqrt{\epsilon_E - \sin^2 \theta}}{\cos \theta_o + \sqrt{\epsilon_E - \sin^2 \theta}}$$

we obtain the desired reflected field components, which we denote by superscript R,

$$\begin{aligned} dE_{11}^R &= R_H'' \left[ \sin \delta \sin (\alpha - \phi'') dE_\rho^I + \cos (\alpha - \phi'') dE_\ell^I \right] \\ dE_{1\perp}^R &= R_H^\perp \left[ -\sin \delta \cos (\alpha - \phi'') dE_\rho^I + \sin (\alpha - \phi'') dE_\ell^I \right] \\ dE_Z^R &= R_V'' \cos \delta dE_\rho^I \end{aligned}$$

As the final step in the procedure of approximating equation A-5, add the direct and reflected fields (transformed back to cartesian components) due to the given source segment, evaluated at an observation point at another antenna segment, and take the dot product with the observation segment tangent vector.

- (1) Pass a vertical plane through the center of the source segment and the observation point. (Plane of Incidence)
- (2) Determine the angle of incidence at the specular point.
- (3) Decompose the electric field into components parallel and perpendicular to the plane of incidence.
- (4) Apply the appropriate reflection coefficients to each component.
- (5) Sum the tangential components of the direct and reflected electric field at the observation point.



#### D. RESULTS USING THE REFLECTION COEFFICIENT METHOD

The most desirable test of a numerical method is comparison with experimental data, and lacking that, with results obtained using other independent analytical techniques. Such comparisons are presented below to validate the reflection coefficient method.

In figure A-3 is shown the input resistance of a vertical half-wave dipole as a function of height over a lossy ground. The comparison with Sommerfeld integral results points out that significant discrepancies occur only when the dipole is very close to the ground and that even when the tip is touching, an error of less than 10 percent is encountered. The input resistance of a  $0.1 \lambda$  horizontal dipole above a dielectric half-space is shown as a function of height above ground in figure A-4. Comparison with the scant independent data indicates close agreement. A comparison with experimental data for a purely dielectric ground is included in figure A-5. The plot pertains to the input resistance of a horizontal half-wave dipole as a function of its height above ground. Since the antenna radiation pattern is also of great interest, we include in figure A-6 the radiation patterns of a monopole over a dielectric ground. The results are compared to those presented in Collin and Zucker (1969) wherein a current distribution on the monopole was assumed. For comparison, a Sommerfeld integral calculation is also provided.

The characteristics of antenna arrays over lossy ground can be easily and accurately established using the approximate approach. Figure A-7 contains plots of the input resistance and radiation patterns of a parasitic array of half-wave dipoles. The discrepancies between two independent approaches are noticeable only for  $h/\lambda < 0.35$ . The same array is considered with variable spacing in figure A-8 where a comparison with the Sommerfeld integral and perfect ground results is included. To emphasize the usefulness of the method, the radiation patterns of a log periodic antenna over various grounds are shown in figure A-9. With a knowledge of the free-space or perfect ground pattern, one must appreciate that an accurate prediction of the pattern over an arbitrary ground would indeed be difficult. Furthermore, for the case shown, the evaluation of the Sommerfeld integrals would be not only difficult, but time consuming and expensive.

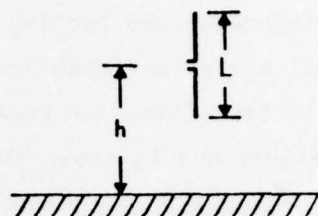
3.0MHz

$\epsilon_r = 10.0$

$\sigma = 3 (10^{-3}) \frac{\text{mho}}{\text{m}}$

x Reflection Coefficient

o Sommerfeld



Vertical Dipole  $L = .5\lambda$

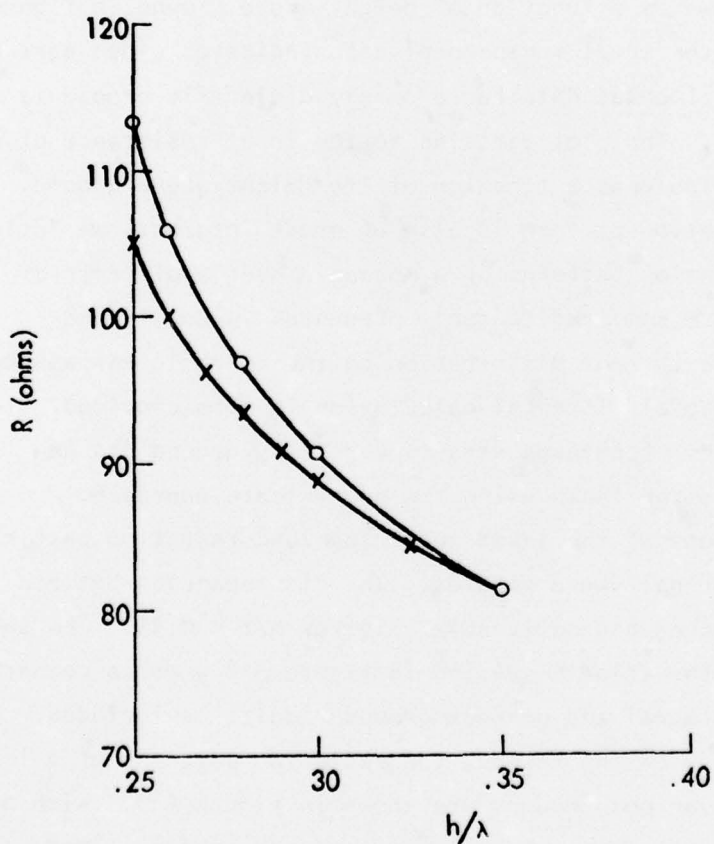


Figure A-3. Input Resistance of a Half Wave Dipole Over a Lossy Ground at 3.0 MHz

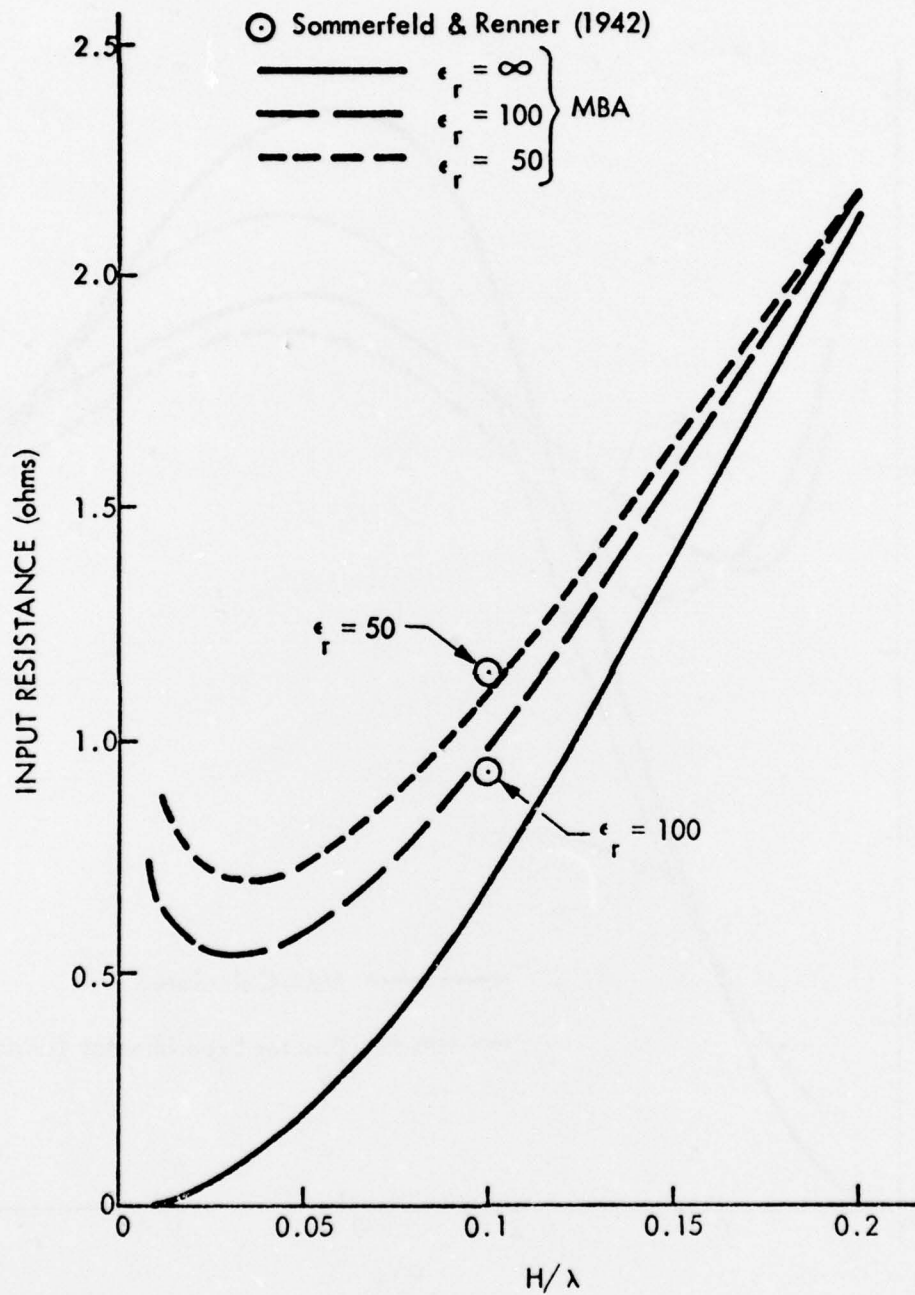


Figure A-4. Input Resistance of Horizontal Dipole,  $0.1\lambda$  Long, Located a Distance  $H$  Above a Purely Dielectric Ground (Dielectric Constant  $\epsilon$ )

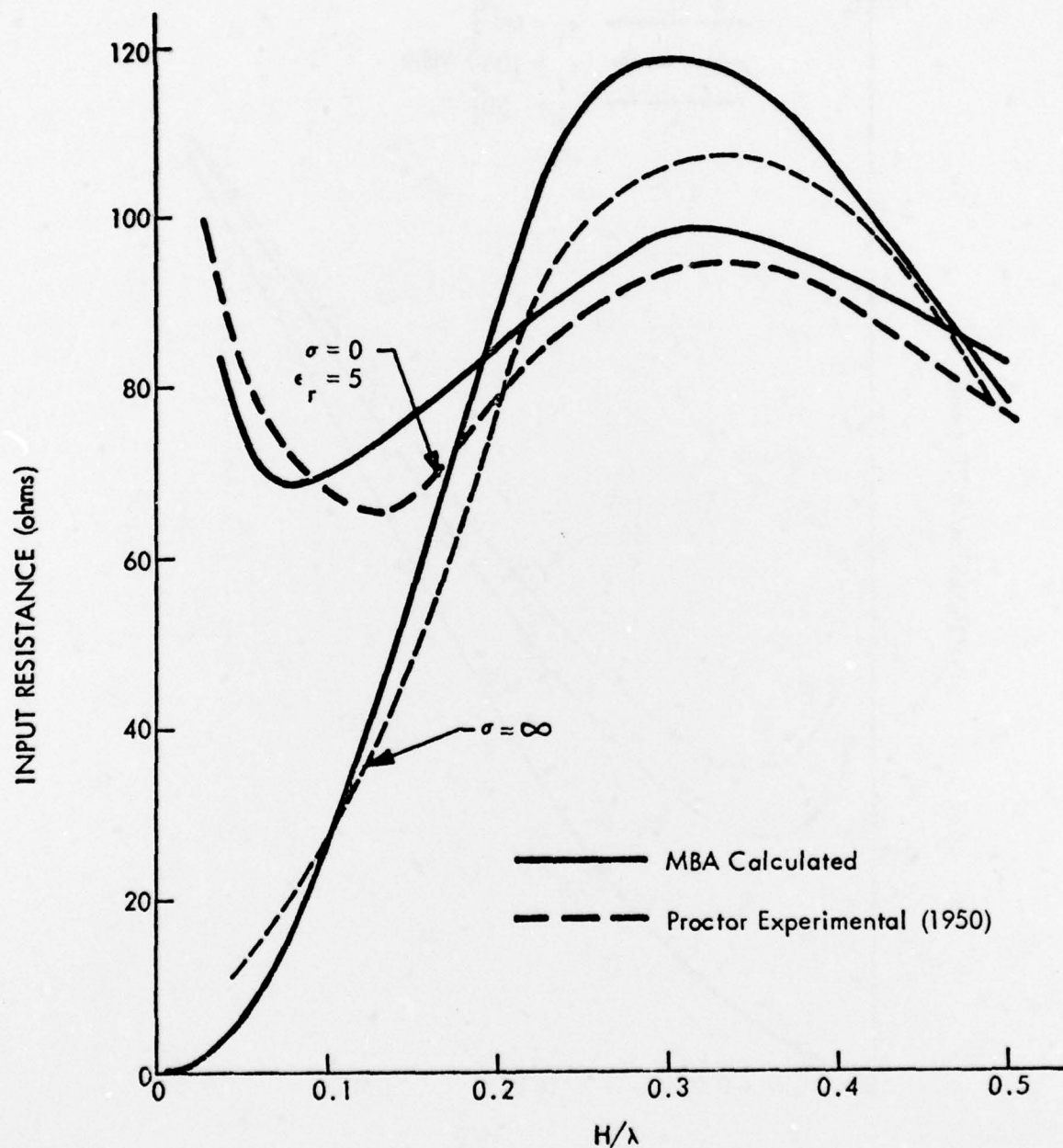
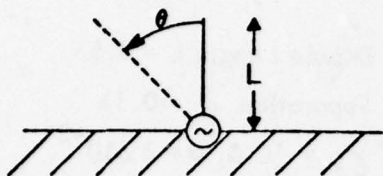


Figure A-5. Input Resistance of Horizontal Half-Wave Dipole Located a Distance  $H$  Above a Purely Dielectric Ground,  $\epsilon = 5$





Monopole Length =  $L$

$\epsilon_r = 4.0$

• MBA Reflection Coefficient

— Collin & Zucker Ant. Theory

x MBA Sommerfeld Integral

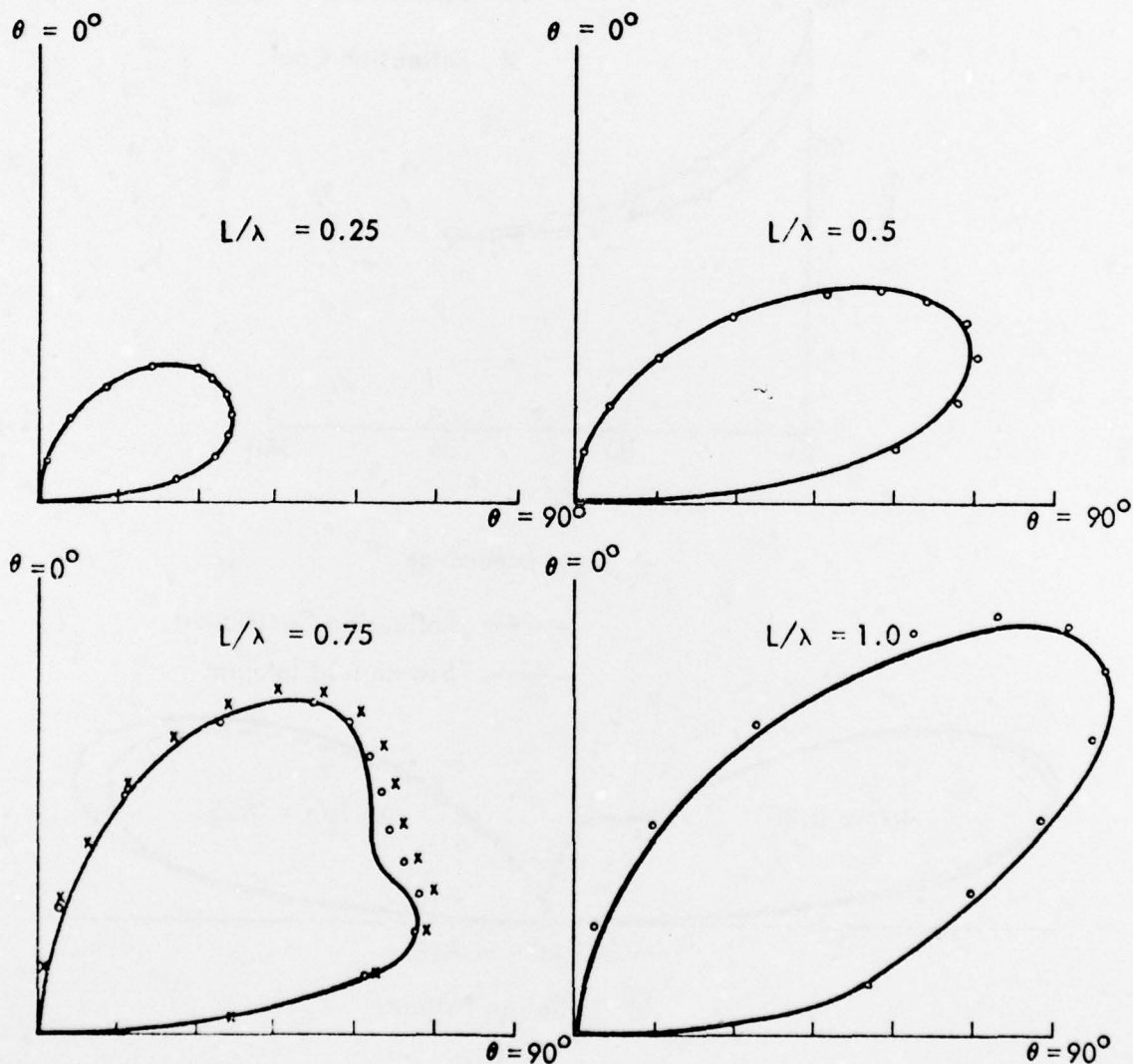
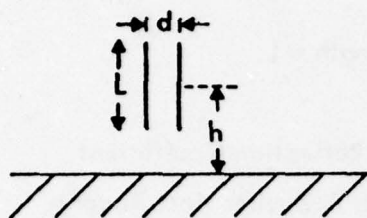
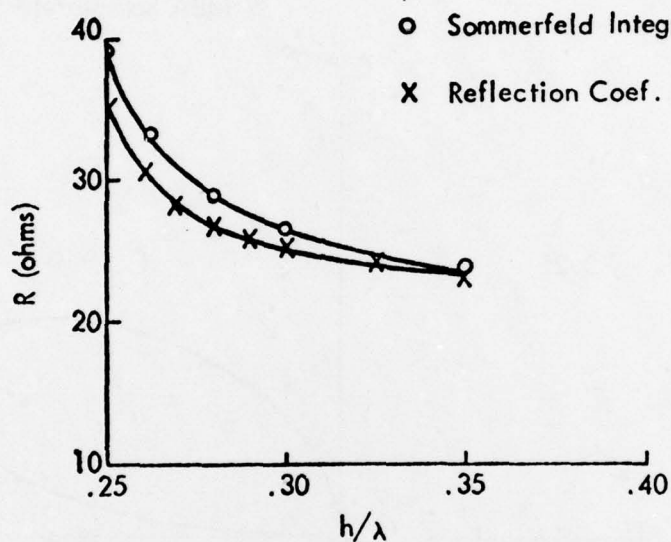


Figure A-6. Radiation Patterns (Linear Voltage Scale) of a Monopole Over a Dielectric Ground

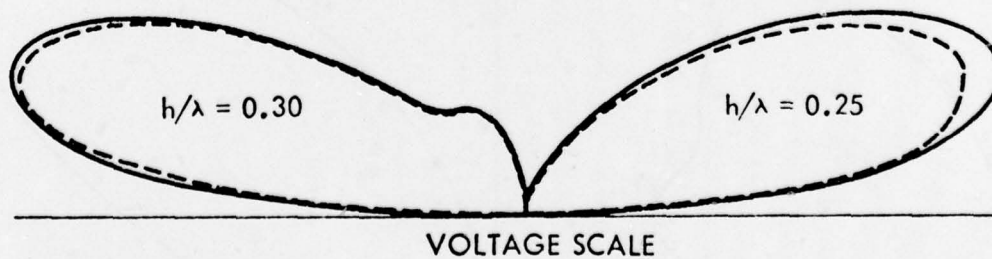


Dipole Length  $L = 0.5\lambda$   
 Separation  $d = 0.1\lambda$   
 $\epsilon_r = 10.0$ ;  $\sigma = 3 \times 10^{-3}$   
 Frequency = 3.0 MHz



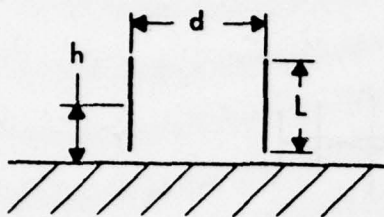
a) Input Impedance

— Reflection Coefficient  
 - - - Sommerfeld Integral



b) Radiation Patterns

Figure A-7. Input Impedance and Radiation Patterns for a Parasitic Array of Two Half-Wave Dipoles



Frequency = 3.0 MHz  
 $\epsilon = 10.0$   $\sigma = 0.01$  mho/m  
 $h/\lambda = 0.3$   $L/\lambda = 0.5$

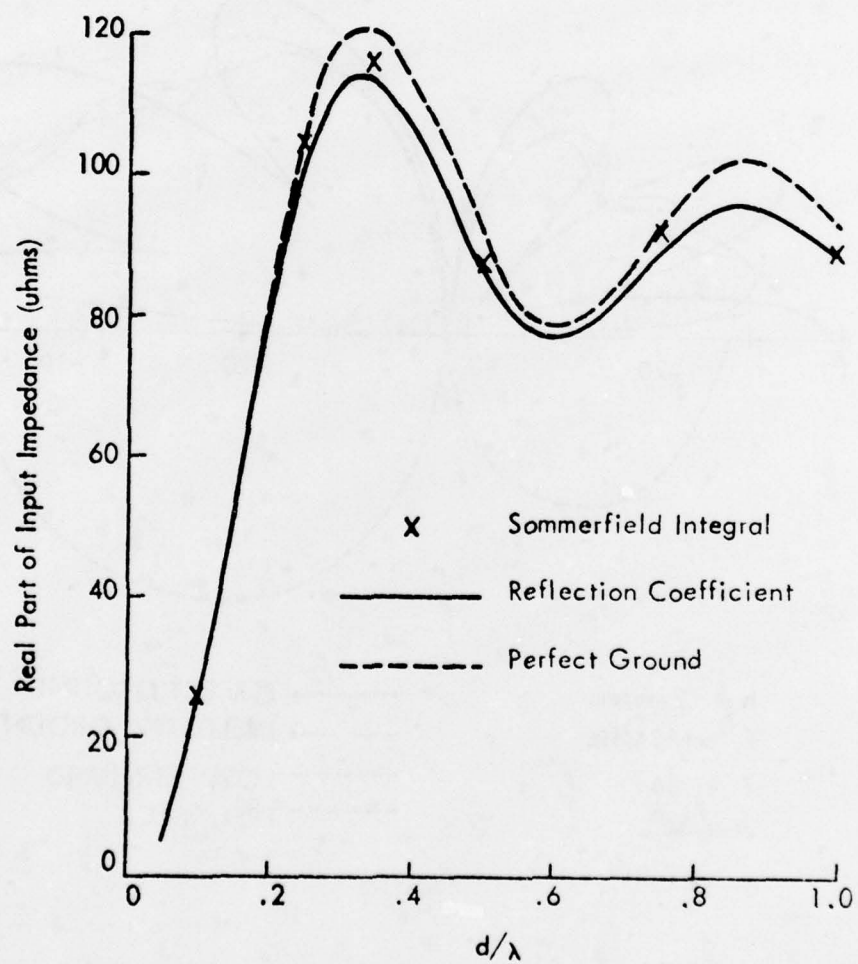


Figure A-8. Input Resistance for a Parasitic Array of Two Half Wave Dipoles

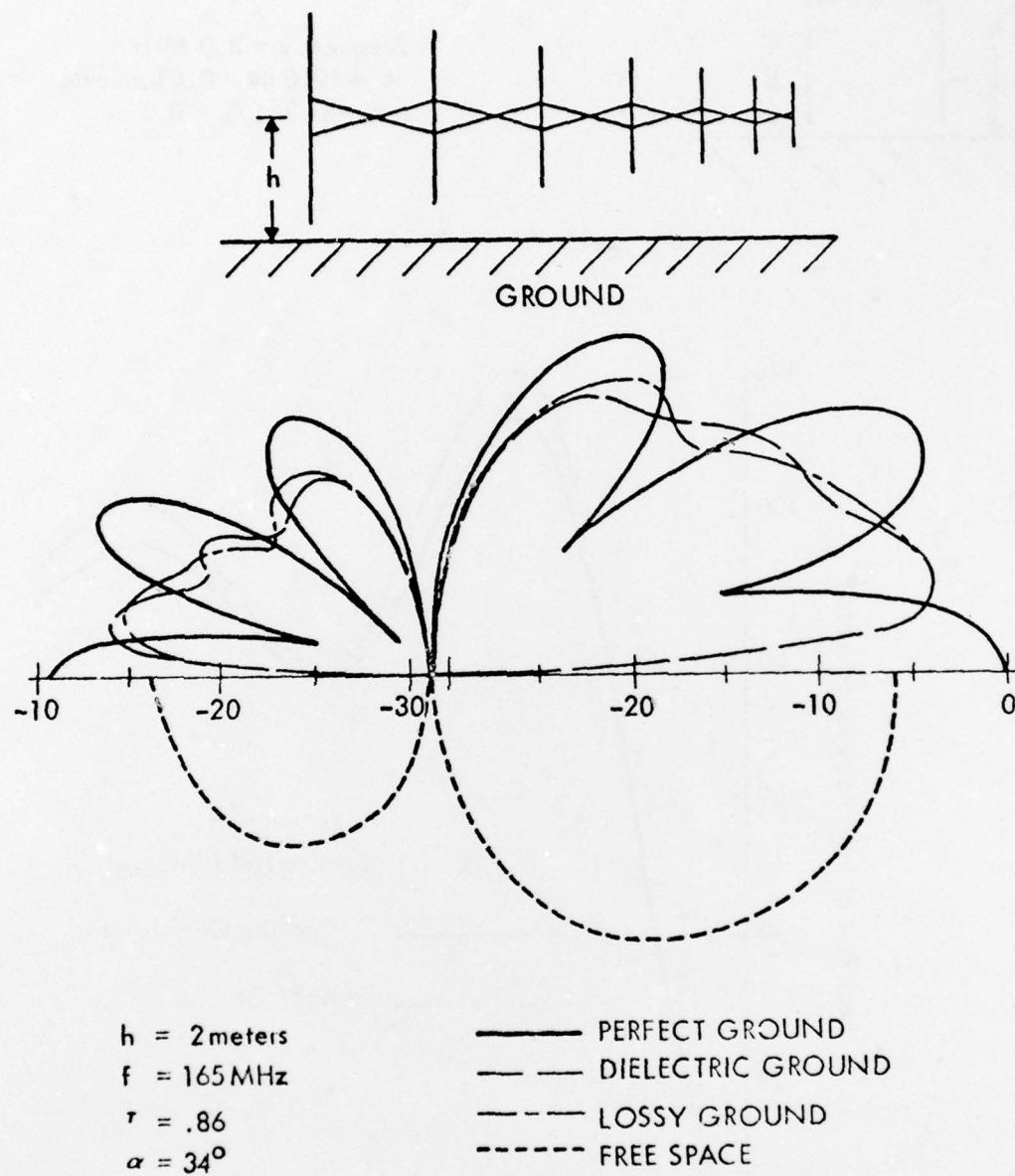


Figure A-9. Radiation Patterns of a Log-Periodic Antenna Over Ground



## BIBLIOGRAPHY

Andreasen, M. G. and F. B. Harris, Jr. Analysis of Wire Antennas of Arbitrary Configuration by Precise Theoretical Numerical Techniques, Technical Report ECOM-0631-F, Contract DAAB07-67-C-0613, Granger Associates, Palo Alto, California, 1968.

Banos, A., Jr. Dipole Radiation in the Presence of a Conducting Half-Space, Pergamon Press, New York, 1966.

Chen, C. L. "On the Scattering of Electromagnetic Waves from a Long Wire," Radio Sci., 3, 1968, pp. 585-598.

Collin, R. E. and F. J. Zucker. Antenna Theory, Part 1, McGraw Hill, New York, 1969.

Crout, P. D. "A Short Method for Evaluating Determinants and Solving Systems of Linear Equations with Real or Complex Coefficients," Trans. Am. Inst. Elec. Engrs. 60, 1941, pp. 1235-1240.

Duncan, R. H. "Theory of the Infinite Cylindrical Antenna Including the Feedpoint Singularity in Antenna Current," J. Res. NBS 66D (Radio Prop.), No. 2, 1962, pp. 181-187.

Fenlon, F. H. "Calculation of the Acoustic Radiation Field at the Surface of a Finite Cylinder by the Method of Weighted Residuals," Proceedings of the IEEE, V. 57, No. 3, 1969, pp. 291-306.

Feynberg, Y. L. The Propagation of Radio Waves Along The Surface of the Earth, Foreign Technology Division, Wright-Patterson Air Force Base, Ohio, 1967.

Hallen, E. "Theoretical Investigation into Transmitting and Receiving Antennae," Nova Acta Regiae Societatis Scientiarum Upsalienis (Sweden), Ser. 4, 11, 1938.

King, R. W. The Theory of Linear Antennas, Harvard Univ. Press, Cambridge, Massachusetts, 1956.

Miller, E. K. "Admittance Dependence of the Infinite Cylindrical Antenna Upon Exciting Gap Thickness," Radio Sci., 2, No. 12, 1967, pp. 1431-1435.

Neureuther, A. R., B. D. Fuller, G. D. Haake, et al. "A Comparison of Numerical Methods for Thin Wire Antennas," presented at the 1968 Fall URSI meeting, Department of Electrical Engineering and Computer Sciences, University of California, Berkeley, 1968.

Ralston, A. and H. S. Wilf, Editors. Mathematical Methods for Digital Computers, John Wiley & Sons, Inc., New York, Chapter 2, 1960.

Siegel, M. "The Electromagnetic Fields of a Dipole in a Dissipative Half-Space: A Numerical Approach," Harvard University Division of Engineering and Applied Physics, May, 1970.

Sommerfeld, A. Partial Differential Equations in Physics, Academic Press, New York, 1964.

Surteff, W. J. "Effects of the Ground Screen on the Field Radiated From a Monopole," Proceedings of Conference on Environmental Effects on Antenna Performance, Boulder, Colorado, Vol. 1, 1969, p. 95.

Wait, J. R. "Impedance of a Hertzian Dipole Over a Conducting Half-Space," Conference on Environmental Effects on Antenna Performance Proceedings, Vol. 1, Boulder, Colorado, July 14-18, 1969.

Wait, J. R., Editor. Conference on Environmental Effects on Antenna Performance, Proceedings, Vol. 1, Boulder, Colorado, July 14-18, 1969.

Wu, T. T. "Theory of the Dipole Antenna and the Two-Wire Transmission Line," J. Math. Physics, 2, 1960, pp. 550-574.

Yeh, Y. S. and K. K. Mei. "Theory of Conical Equiangular Spiral Antennas: Part I - Numerical Techniques," IEEE Trans. Ant. Prop. AP-15, 1967, pp. 634-639.

# METRIC SYSTEM

## BASE UNITS:

Quantity	Unit	SI Symbol	Formula
length	metre	m	...
mass	kilogram	kg	...
time	second	s	...
electric current	ampere	A	...
thermodynamic temperature	kelvin	K	...
amount of substance	mole	mol	...
luminous intensity	candela	cd	...

## SUPPLEMENTARY UNITS:

plane angle	radian	rad	...
solid angle	steradian	sr	...

## DERIVED UNITS:

Acceleration	metre per second squared	...	m/s
activity (of a radioactive source)	disintegration per second	...	(disintegration)/s
angular acceleration	radian per second squared	...	rad/s
angular velocity	radian per second	...	rad/s
area	square metre	...	m
density	kilogram per cubic metre	...	kg/m
electric capacitance	farad	F	A-s/V
electrical conductance	siemens	S	A/V
electric field strength	volt per metre	...	V/m
electric inductance	henry	H	V-s/A
electric potential difference	volt	V	W/A
electric resistance	ohm	...	V/A
electromotive force	volt	V	W/A
energy	joule	J	N-m
entropy	joule per kelvin	...	J/K
force	newton	N	kg-m/s
frequency	hertz	Hz	(cycle)/s
illuminance	lux	lx	lm/m
luminance	candela per square metre	...	cd/m
luminous flux	lumen	lm	cd-sr
magnetic field strength	ampere per metre	...	A/m
magnetic flux	weber	Wb	V-s
magnetic flux density	tesla	T	Wb/m
magnetomotive force	ampere	A	...
power	watt	W	J/s
pressure	pascal	Pa	N/m
quantity of electricity	coulomb	C	A-s
quantity of heat	joule	J	N-m
radiant intensity	watt per steradian	...	W/sr
specific heat	joule per kilogram-kelvin	...	J/kg-K
stress	pascal	Pa	N/m
thermal conductivity	watt per metre-kelvin	...	W/m-K
velocity	metre per second	...	m/s
viscosity, dynamic	pascal-second	...	Pa-s
viscosity, kinematic	square metre per second	...	m/s
voltage	volt	V	W/A
volume	cubic metre	...	m
wavenumber	reciprocal metre	...	(wave)/m
work	joule	J	N-m

## SI PREFIXES:

Multiplication Factors	Prefix	SI Symbol
1 000 000 000 000 = 10 <sup>12</sup>	tera	T
1 000 000 000 = 10 <sup>9</sup>	giga	G
1 000 000 = 10 <sup>6</sup>	mega	M
1 000 = 10 <sup>3</sup>	kilo	k
100 = 10 <sup>2</sup>	hecto*	h
10 = 10 <sup>1</sup>	deka*	da
0.1 = 10 <sup>-1</sup>	deci*	d
0.01 = 10 <sup>-2</sup>	centi*	c
0.001 = 10 <sup>-3</sup>	milli	m
0.000 001 = 10 <sup>-6</sup>	micro	μ
0.000 000 001 = 10 <sup>-9</sup>	nano	n
0.000 000 000 001 = 10 <sup>-12</sup>	pico	p
0.000 000 000 000 001 = 10 <sup>-15</sup>	femto	f
0.000 000 000 000 000 001 = 10 <sup>-18</sup>	atto	a

\* To be avoided where possible.

*MISSION  
of  
Rome Air Development Center*

*RADC plans and conducts research, exploratory and advanced development programs in command, control, and communications (C<sup>3</sup>) activities, and in the C<sup>3</sup> areas of information sciences and intelligence. The principal technical mission areas are communications, electromagnetic guidance and control, surveillance of ground and aerospace objects, intelligence data collection and handling, information system technology, ionospheric propagation, solid state sciences, microwave physics and electronic reliability, maintainability and compatibility.*

